Investigation of Hygro-Thermal Strain in Polymer Electrolyte Membranes Using Optical Coherence Elastography

by

Victor Keller
BEng, University of Liverpool, 2011

A Thesis Submitted in Partial Fulfillment
of the Requirements for the Degree of

MASTER OF APPLIED SCIENCE

in the Department of Mechanical Engineering

Supervisory Committee

Investigation of Hygro-Thermal Strain in Polymer Electrolyte Membranes Using Optical Coherence Elastography

by

Victor Keller
BEng, University of Liverpool, 2011

Supervisory Committee

Dr. Nedjib Djilali, Department of Mechanical Engineering
Co-Supervisor

Dr. Peter Wild, Department of Mechanical Engineering
Co-Supervisor

Abstract

Supervisory Committee
Dr. Nedjib Djilali, Department of Mechanical Engineering
Co-Supervisor
Dr. Peter Wild, Department of Mechanical Engineering
Co-Supervisor

The work present in this thesis report introduces a novel non-destructive technique for experimentally measuring through thickness hygro-thermal strain of Nafion membranes though digital image correlation. An Optical Coherence Tomography (OCT) system was used to acquire images of a Nafion-TiO_2 (titanium dioxide powder) composite membranes in a fuel cell like device. The proposed technique, commonly known as optical coherence elastography (OCE) makes use of the normalized correlation algorithm to calculate strain between two successive scans of different relative humidity step values. Different normalized correlation parameters were compared to measured results of PDMS-TiO_2 phantoms in order to analyze accuracy. The effect of TiO_2 on Nafion membranbes mechanical properties was further analysed by comparing the swelling behaviour of membranes with different concentrations. It has been found that Nafion undergoes approximately 25 – 30% more strain on the land section than on the channel section, regardless gas diffusion electrode (GDE) layer presence. Furthermore, it was shown that the overall strain on the material decrease by approximately 10% when GDE layers are present. Overall this work demonstrated how OCE is a viable technique for measuring through thickness strain distribution in Nafion composite membranes and has the potential to be implemented for non-destructive in situ measurements.

Table of Contents

List of Tables

List of Figures

Acknowledgments

I would like to express my deepest appreciation to my two supervisors Dr. Nedjib Djilali and Dr. Peter Wild for their advice, insight, and commitment and for offering me this amazing opportunity. I cannot express enough gratitude to Dr. Nigel David, who was the project manager from start to near completion. Nigel's insight, knowledge, humor and mentoring were essential parts for the completion of this work. I would also like to thank my fellow researchers and graduate students in the Energy Systems and Transport Phenomena group for your feedback and support and fellow researchers Geoff Burton and Steven Warwick for you kindness and assistance. To Rodney Katz at the engineering machine shop for your patience and feedback and to my fellow IESVic members.

I would also like to acknowledge Dr. Marinko Sarunic at the at the Biomedical Optics Research Group at Simon Fraser University and his graduate student Michelle Cua for their collaboration and allowing use to their OCT system.

I would like to acknowledge Dr. Steven Holdcroft from the Department of Chemistry at Simon Fraser University and his graduate student Thomas Weissbach for their assistance in casting the composite membranes.

Dedication

This theses is dedicated to my parents for their never ending support, my sisters Ingrid and Laetitia and my grandfather who motivated me to become an engineer.

Chapter 1: Introduction

1.1 Overview

Fuel cells are devices with the ability to convert chemical energy directly into electrical energy. Although the fuel cell is a relatively new technology, it can be found in a wide range of sizes, power output levels and fuel types. Fuel cells have found applications as power extenders in small electronic devices, combined heat and power (CHP) generators for households and as vehicular power sources, among others. Over the past few years, fuel cells have received a great deal of attention and become an ever stronger candidate as an alternative power source in the automotive industry. A strong contender is the Proton Exchange Membrane Fuel Cell (PEMFCs). When compared to internal combustion engines, PEMFCs provide higher energy efficiency and have zero emission at the point of use. However, a number of drawbacks remain unsolved. Hydrogen storage and infrastructure, high costs and durability are the main factors to be addressed before large-scale commercialization of fuel cell vehicles takes place. The durability of the PEMFCs are strongly limited by the mechanical and chemical degradation mechanisms. This thesis focuses on the mechanical degradation issue in Nafion membranes for PEMFCs. This report presents a novel technique for studying the mechanical degradation of Nafion membranes during humidity cycles in a fuel cell and measuring through depth strain distribution.

1.2 Motivation

The degradation mechanisms in PEMFCs are important factors to be addressed for the successful commercialization of the fuel cell vehicle. The U.S. Department of Energy has established a durability target of voltage loss lower than 10% with 5000 h of cyclic use at high operating temperatures [1, 2] equivalent to roughly 150,000 miles. The durability is impacted by a combined effect of chemical and mechanical degradation mechanisms. Relative humidity and temperature have a significant impact on cell performance [3]. These

two components tend to undergo cycling during a normal drive cycle. This process is called hygro-thermal cycling. The polymer membrane at the centre of the fuel cell responds to increased humidity and temperature by swelling. Therefore this so called hygro-thermal cycling leads to swelling-shrinking cycles on the membrane [4, 5]. This results in stress cycles in the membrane and leads to material failure by fatigue in a process reffered to as mechanical degradation.

While much work has been carried out on modeling the stresses in the polymer membrane under fuel cell operating conditions [1, 6, 7, 8], there is currently a lack of experimental studies measuring swelling-shrinkage cycles. To the knowledge of the authors, the experimental studies available in the literature on membrane mechanical characteristics to date have been carried out ex-situ and are limited to thickness change measurements as mentioned in section 2.3. This thesis studies the implementation of a technique to experimentally determine through thickness strain maps of fuel cell membranes with the potential to be carried out in situ. By developing such a technique, it would become possible to study localized strain in Nafion membranes and determine the conditions in which the material may undergo plastic strain.

The work presented here introduces digital image correlation as a technique to measure through thickness strain maps in Nafion membranes and optical coherence tomography (OCT) as a technique to acquire Nafion membrane scans. Speckle tracking is used on successive images of the membrane with varying humidity levels. Speckle tracking allows for the determination of a through-thickness strain distribution in the polymer membrane. The technique was demonstrated to work ex situ and in situ with minor cell modifications. Microscope acquired images were further used to analyse the membranes response, but limited to ex situ experiments. Cell alterations for OCT imaging are carefully considered in order not to impact the cell performance.

Composite membranes with the addition of a contrast agent were fabricated in order to generate speckled images necessary for speckle tracking. The mechanical response of different concentrations of contrast agent is also studied in order to characterize its impact on the mechanical properties of the membrane.

1.3 Thesis Goal and Objectives

The primary goal of this work is to develop a technique with the potential to study through thickness swelling strain distribution of Nafion membranes for fuel cells. The technique must be non-destructive and have the potential to be carried out in situ in a working fuel cell with minimal intrusion. Optical Coherence Tomography was used as the main imaging technique with the potential for being carried out in situ. Strain maps were further calculated by means of Digital Image Correlation (DIC) by tracking the position of speckles. Microscope acquired images were further used to acquire additional data for comparison, but were limited to ex situ experiments. The specific deliverables of the project are:

A. Acquire Nafion OCT scans in a representative fuel cell environment and establish necessary modifications to the material in order to create a speckled pattern
B. Fabricate modified membranes with minimal alterations to commercially available material.
C. Establish a filtering technique for removing speckled noise present in OCT scans without affecting membranes speckled pattern.
D. Digital Image Correlation Analysis.
    a. Study the effect of changing parameters in DIC.
    b. Establish the appropriate conditions for accuracy by comparing DIC swelling results to comparison measurements.
E. Study the effect of contrast agent concentration on results.
F. Membrane Swelling Analysis
    a. Study the effect of incorporation of Gas Diffusion Layers
    b. Study effect of location on membrane swelling
G. Demonstrate capacity for outputting strain maps
H. Demonstrate the potential for the technique to be carried out in situ

1.4 Thesis Outline

Chapter 1 introduces the motivation for this work by highlighting some of the shortcomings still to be overcome by fuel cells. It was pointed out that there currently is a

lack of experimental studies that are able to measure through thickness strain distribution in fuel cell membranes.

Chapter 2 provides background information on the operating principles of hydrogen fuel cells, the importance of Nafion and the mechanical degradation mechanism. Current methods available in the literature for measuring membrane swelling are reviewed in this chapter. The reasons for selecting optical coherence tomography are discussed along with its operating principles, strengths and limitations. Elastography is introduced and the effect of changing parameters were noted. The chapter closes with a discussion of how contrast agents are used to provide speckled patterns, and image processing considerations.

Chapter 3 covered the experimental methodology carried out in this work, and detailed information on the architecture of the experimental setup. The methodology carried out in casting the PDMS-TiO_2 phantoms and Nafion-TiO_2 membranes is described. The details of the experimental technique are described.

The results of the validation experiments are covered in chapter 4.

Chapter 5 presents the experimental results along with detailed analysis, discussion and recommendations for further work.

Chapter 6 summarizes the findings and draws conclusions.

Chapter 2: Background and Literature Review

2.1 PEMFC Structure and Operating Conditions

A single PEM fuel cell is a multilayer device formed by different materials with specific functions. Fuel cell are designed and constructed to maximize efficiency, robustness and durability while minimizing weight and costs. Figure 2-1 below shows a representation of the main components of a PEM fuel cell [9]. The anode and cathode graphite plates (regions T and S on Figure 2-1), also known as bipolar plates, are responsible for making up the mechanical structure to the fuel cell and facile transport of products and reactants to and from the fuel cell [10]. Layers D and E are known as the Gas-Diffusion Electrode (GDE), which is made up of the Gas-Diffusion Layer (GDL) coated with the micro-porous layer. The function of the GDL is to facilitate the transport of electrons and species to and from the surface of the catalyst layers (layers A and C).

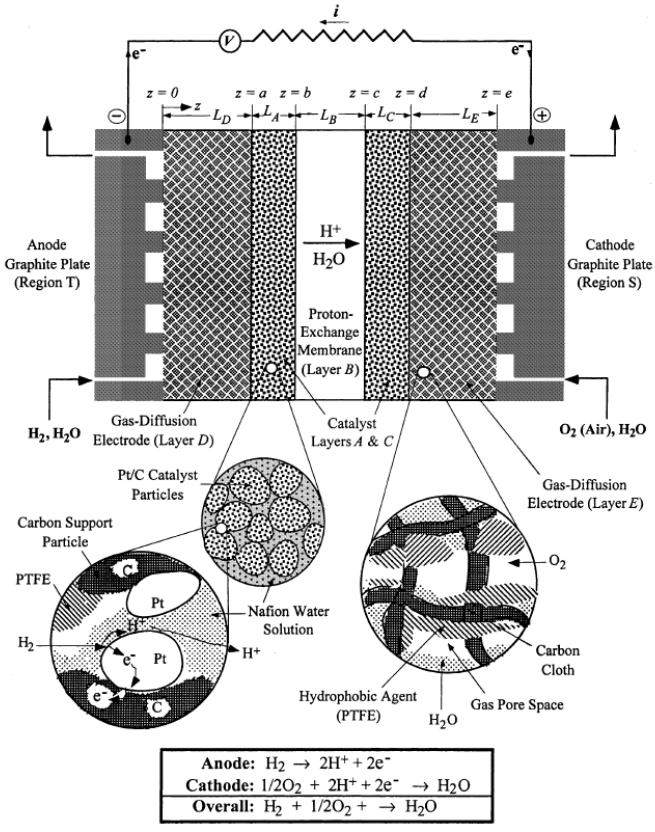

Figure 2-1. Schematic representation of the main Components of a PEM fuel cell [9]

The catalyst layers are the components where the electrochemical reactions responsible for cell operation take place. The anode catalyst (component A) allows for the hydrogen oxidation reaction (HOR), where electrons and protons in a hydrogen molecule are separated. The cathode electrode (component C) is where protons, electrons and oxygen from air combine to form water and release heat. Lastly, the proton exchange polymer membrane is located in the middle of the fuel cell. Typically the membrane is made of a sulfonated copolymer of trade name Nafion, although other similar materials are also commercially available. For more information on the morphology and properties of Nafion, please refer to section 2.2.1.

The electrochemical reaction in a PEMFC is shown schematically in Figure 2-2 . This reaction makes use of hydrogen fuel and oxygen from air, while the by-products of the reaction are water vapour and heat. Firstly the high pressure hydrogen is pumped into the flow channels of the anode graphite plate. The gas diffusion layer then serves as a permeator between the graphite plate and the anode catalyst layer [9, 10, 11]. Hydrogen is then dissociated into protons and electrons [12]. This is known as the hydrogen oxidation reaction (HOR).

$$H_2 \rightarrow 2H^+ + 2\,e^- \tag{1.1}$$

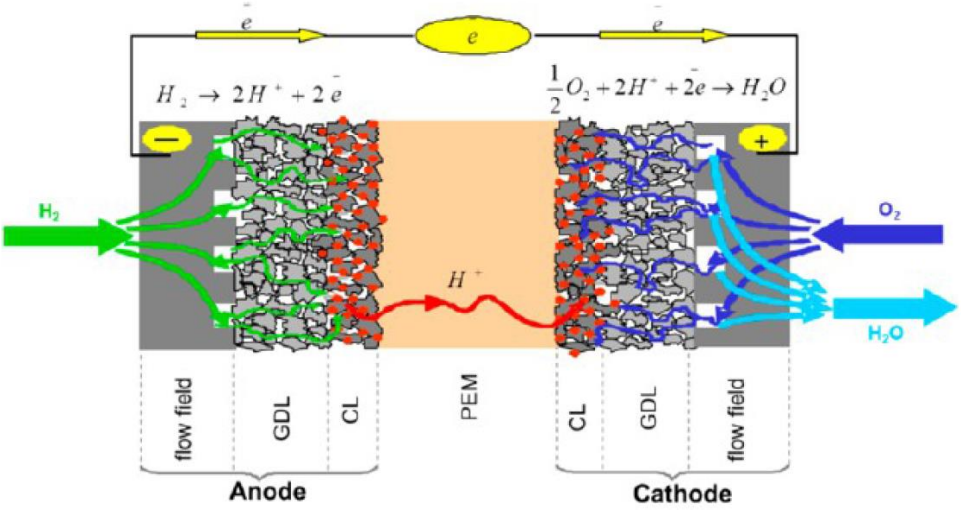

Figure 2-3. A Schematic of the operation of a PEM fuel cell [13]

The protons (positively charged particles) travel through the polymer membrane to the cathode side, while the electrons (negatively charged particles) travel back through the GDL and onto an external circuit to the cathode side [10, 11, 12]. More details on proton conduction on the polymer membrane can be found on section 2.2. The membrane also serves as an electrical insulator, stopping electrons from directly flowing to the cathode side [10]. An electrical potential gradient attracts the electrons to the cathode side, which are conducted through an external circuit as seen in Figure 2-2 above. The electrons flow to the cathode catalyst layer where the oxygen reduction reaction (ORR) takes place. The (ORR).

$$2H^+ + 2\,e^- + \frac{1}{2}O_2 \rightarrow H_2O \tag{1.2}$$

The overall reaction in the fuel cell can be found by combining Equations 1.1 and 1.2 which yields:

$$H_2 + \frac{1}{2}O_2 \rightarrow H_2O \tag{1.3}$$

The overall reaction of the PEMFC creates a maximum theoretical voltage of 1.23 V [10] at standard temperature and pressure, while the current depends on the molar rate of consumption of reactants on the fuel cell. However, real cells cannot achieve this maximum theoretical voltage of 1.23 V due to internal loses. These losses are due to a combination of activation energy, ohmic polarization and concentration polarization. More information on the details of the operating principles of fuel cells and performance characterization can be found in reference 10.

When installed in a vehicle, a fuel cell should be able to cope with dynamic drive cycles. However, water flux and water concentration in the membrane are strong functions of the operating conditions. Mainly this is affected by the electro-osmotic drag [10]. The electro-osmotic drag can be reviewed as voltage gradient driven flow. Thus, as the operating conditions of the fuel cell change, so does the water content. The polymer swells with increased water content and shrinks upon dehydration. These hydration/dehydration cycles lead to mechanical stress cycles [2, 4]. It has been recognized in recent years that these hygrothermal stresses may lead to fatigue [4]. The next section summarizes some of

the studies available in the literature regarding the polymer membrane, its morphology, properties and degradation mechanisms.

2.2 Nafion

The polymer membrane is a key component of the PEM fuel cell. It works as a physical separator between anode and cathode preventing reactant crossover and flow of electrons, while acting as a protonic conductor. Ideally the material of choice must provide high ionic conductivity, high electronic resistivity, low costs, mechanical and chemical stability and low gas permeability [14]. DuPont's Nafion is the most widely used polymer electrolyte for PEM fuel cells. Nafion is a perfluorosulfonic acid (PFSA) polymer that has shown high proton conductivity and chemical stability. Much progress has been made in recent years towards reduction of chemical degradation [4]. However, as Nafion is still prone to mechanical failure [15], some attention has been shifted to the mechanical degradation mechanism as it is believed to be a life limiting factor [4].

2.2.1 Structure and Morphology

The polymer structure of consists of a tetrafluorethylene copolymer (backbone) and a sulfonated end group (side chains) [12].

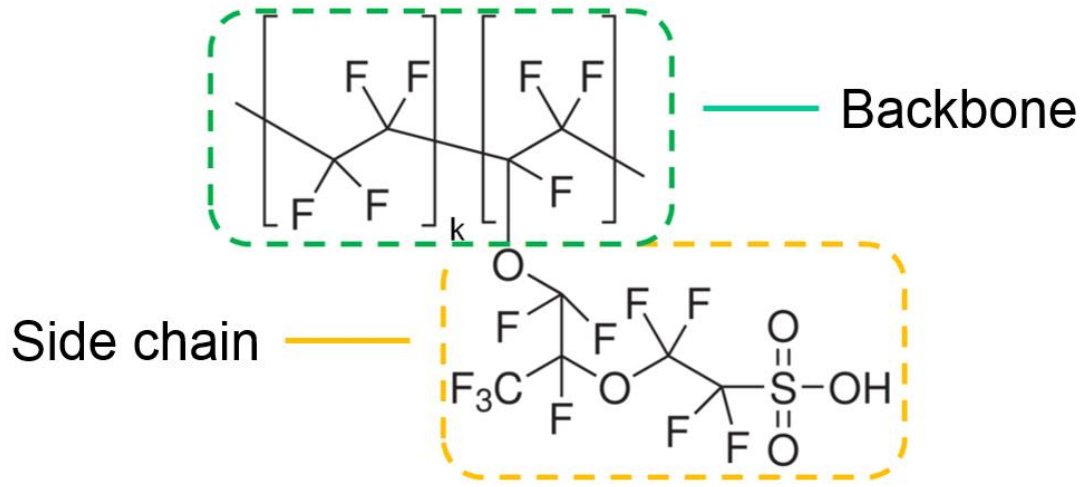

Figure 2-4. Representation of the chemical structure of Nafion. Backbone (top) and side chain (bottom).

The backbone is formed of semi-crystalline chains of polytetrafluoroethylene (PTFE), also commercially known as Teflon [16]. Teflon is responsible for proving the membrane its physical strength and chemical stability [12, 17].

The ionic group, or side chain, attached to the membrane backbone is responsible for the ionic transport. In the case of Nafion, the side chain ends in a sulfonic acid functional group [10, 17]. When hydrated, the sulfonic acid end group becomes negatively charged (SO_3^-) [10]. This allows for the passage of positively charged particles, while repelling negatively charged particles [16]. In other words, it allows for protons to travel through the membrane while blocking the passage of electrons.

The ionic conductivity and mechanical properties of the polymer are strongly related to the structural relationship between backbone and side chains. A key parameter to characterize the structure of the polymer is the equivalent weight, which takes account for the ratio between backbone polymer and sulfonic acid groups [10].

$$EW\ \left(\frac{g}{eq}\right) = \ 100\ k + 446 \tag{1.4}$$

Where k is the number of tetrafluorethylene groups per polymer chain [10]. Increasing the EW should theoretically lead to stronger mechanical properties at the cost of lower ionic conductivity [10, 12]. Common values for EW for fuel cell applications range from 800 to 1200. Nafion is normally designated in a sequence of three or four numbers, containing information of its EW and membrane thickness. The first two numbers refer to the EW, while the third and possible fourth numbers represent the dry membrane thickness in thousands of an inch [10]. Nafion 112 for example is a polymer membrane with dry thickness of 0.002" (51 μm) and equivalent weight of 1100.

The ionic conductivity of Nafion strongly depends on the membrane morphology, which has been the subject of intense research [18, 19]. However the morphology of the polymer strongly changes with hydration level. In 1999, Gebel proposed a model describing the morphology of Nafion according to humidity level. In this model, Gebel described the membranes to form a structure of spherical ionic clusters. The cluster size is typically 15 Å in diameter for dry membranes. For water volume fractions (Φ_W) of 0.2, the morphology of the material starts to change. The cluster size may increase to 40 Å, while the number of clusters tends to decrease, ultimately leading to membrane swelling. A representation of the evolution of the polymer structure with water content can be seen in Figure 2-5 below

[19]. Between $\Phi_W = 0.3 - 0.5$ the clusters keep increasing in size to typically 50 Å and the clusters become interconnected with cylinders of water. At values above $\Phi_W = 0.5$, a phenomenon called inversion takes place. The hydrophobic phase becomes entangled and formins chains, while the ionic groups form interconnected rods, increasing the protonic conductivity. From $\Phi_W = 0.5 - 0.9$ the membrane continues to swell as the spacing between ionic rods increases, but the radius of the ionic rods remains relatively unchanged (R$\approx$ 25 Å).

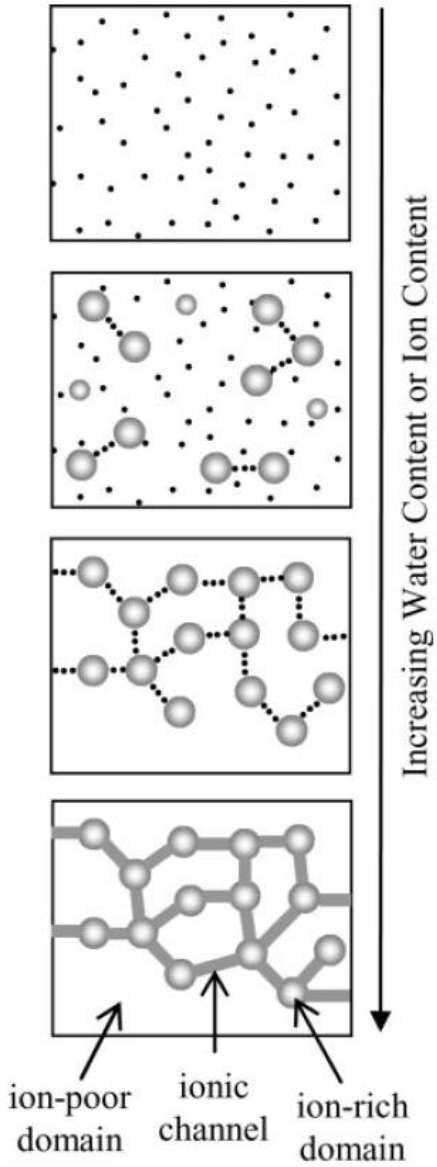

Figure 2-5. Change of morphology of Nafion as a function of hydration level [19].

2.2.2 Water Balance and Management

The last two sections highlighted the importance of water for the operation of the fuel cell as the protonic conduction of solid polymer electrolytes such as Nafion is strongly dependent on water content. Water is introduced in the cell by humidification of inlet gases and as result of the electrochemical reactions taking place during operation. The term flooding is used for water accumulation in the cell and the formation of water droplets. Phase change and ejection of droplets through the flow channels regulate the amount of water in the cell. On the other hand, when the cell works in a net drying condition, the water content in the membrane, GDL and flow channels decreases. This decrease in overall relative humidity ultimately leads to a reduction in performance. In the previous section, the water volume fraction was used to describe the change in morphology with hydration. Membrane hydration is more commonly characterized in terms of the water content (λ).

$$\lambda = \frac{\mathrm{H_2O}}{\mathrm{SO_3H}} \tag{1.9}$$

Maximum water uptake depends greatly on the EW of the polymer. For EW of 900 and 1100 maximum λ is typically 30 and 20 respectively. The conductivity of Nafion 1100 EW as a function of λ is given empirically by:

$$\sigma_i \left(\frac{S}{cm}\right) = \exp\left[1286 \left(\frac{1}{303} - \frac{1}{T}\right)\right] (0.005193\lambda - 0.00326) \tag{1.10}$$

For 25 °C ≤ T ≤ 90 °C

Hence by increasing λ, the overall conductivity of the membrane increases. However when the cell operates at flooding conditions, the liquid water may restrict fuel-flow which ultimately will affect the performance of the cell. Therefore proper water management is vital for optimal cell operation. There are four basic modes of local water transport in the membrane: diffusion, electro-osmotic drag, hydraulic permeation and thermo-osmosis [10].

Diffusion of water in Nafion is a concentration gradient driven flow. The diffusion flux can be modelled according to Fick's law:

$$\dot{n}_w = -D_w \frac{dc_w^m}{dx} \tag{1.11}$$

Where c_w^m is the molar concentration of water and D_w is the diffusion coefficient. D_w has been measured to change with temperature and water content according to Equations 1.12 and 1.13 below [10].

$$D_w = 3.10 \text{ X } 10^{-3} \lambda (-1 + exp^{0.28\lambda}) \exp\left[\frac{-2436}{T(K)}\right] for\ (0 < \lambda \leq 3) \quad (1.12)$$

$$D_w = 4.17 \text{ X } 10^{-4} \lambda (1 + 161\ exp^{-\lambda}) \exp\left[\frac{-2436}{T(K)}\right] for\ (3 \leq \lambda < 17) \quad (1.13)$$

The water mass transport by electro osmotic drag is related to the movement of protons from anode to cathode side in a similar fashion to the vehicular motion of protons. Water molecules are dragged by protons due to the polarity of the molecule from anode to cathode side [10]. The water transport is proportional to the proton flux across the membrane as described by Equation 1.14. The higher the current density or proton flux, the higher the water transport across the membrane.

$$\dot{n}_{H_2O} = n_d \frac{iA}{F} \quad (1.14)$$

Where $n_d$is the electro osmotic drag coefficient. This coefficient changes with water content and membrane type and is typically found experimentally. Common values range from 1-5. A is the cross section area of the cell, i is the current density and F is the Faraday's constant.

The difference in pressure between anode and cathode could also lead to hydraulic permeability of water through the membrane. The molar flow rate of water follows Darcy's law, as seen in Equation 1.5.

$$\dot{n}_{H_2O} = \frac{k\Delta P_{c-a}}{\mu l} \quad (1.14)$$

Where ΔP_{c-a} the pressure difference between cathode and anode, k is the permeability of the membrane, l is the membrane thickness and μ is the viscosity of the fluid. This water transport mechanism can take place in gas and liquid phase. The gas phase hydraulic permeability is normally small as fuel and oxidant are typically pumped at similar pressures [10]. The liquid phase is typically more significant due to the capillary pressure difference.

The GDL or the introduction of a diffusion media is normally engineered to induce capillary pressure create a water flux.

The fourth and last mode of water transport is thermo-osmosis. As a general rule, water moves from warm to cold locations [10]. However, it has been stated in literature that this mode is still poorly understood [10], but it is believed to take place in similar fashion of capillary pressure change.

The four different water transport mechanisms play a key role in membrane water content. As electro-osmotic drag tends to vary during life cycles, so does diffusion driven flows. This ultimately leads to the membrane undergoing humidifying – drying cycles. As mentioned on section 2.2.1, the membrane responds to humidity by swelling, which could lead to stress cycling of the material. The next section is an overview of the mechanical properties of Nafion and how this humidity cycling may lead to the mechanical degradation mechanism.

2.2.3 Mechanical Properties and Degradation Mechanism

The previous sections highlighted the importance of water for cell operation and how hydration level is vital for protonic conduction. However water content leads to polymer relaxation [12]. This relaxation or swelling is caused by the increased distance of nodes as water content increases [18], as stated in section 2.2.1. As water content and water flux change with operating conditions, it is believed that the membrane undergoes swelling-shrinking cycles under dynamic loads [8]. Both temperature and humidity lead to swelling-shrinking cycles, although hydration-induced swelling is much more significant than temperature induced swelling [7]. Although these hydrothermal cycles are well below the material ultimate strength, cyclic loads may lead to material fatigue [20].

Earlier studies have been carried out to test the polymer's mechanical behaviour. Typically the polymer is subjected to a uniaxial tensile test in order to experimentally find its strength [4, 5]. It has been found that the strength of Nafion is highly dependent on the environmental conditions, i.e. temperature and humidity. However, a 50% RH is commonly used as a standard for comparison of different membrane types. Nafion EW = 1100 typically has an ultimate strength of about 17-19 MPA under 50% RH and 25 ℃

conditions, although there may be some discrepancies between studies, likely due to preparation methods and pre-conditioning. However, it is possible to see that as a general trend that the strength of Nafion membranes decreases with both humidity and temperature, as seen in Figure 2-6 and Figure 2-7 [7]. It is believed that water acts as a platicizer, softening the material and reducing its strength [7]. This is probably due to the formation of ionic domains and their increased size and distance, leading to lower entanglement of backbone chains as water content increases.

More representative studies of fuel cell operating conditions have been numerically carried out in an attempt to characterize the stresses undergone by the membrane during fuel cell operation [1, 2, 5, 8].

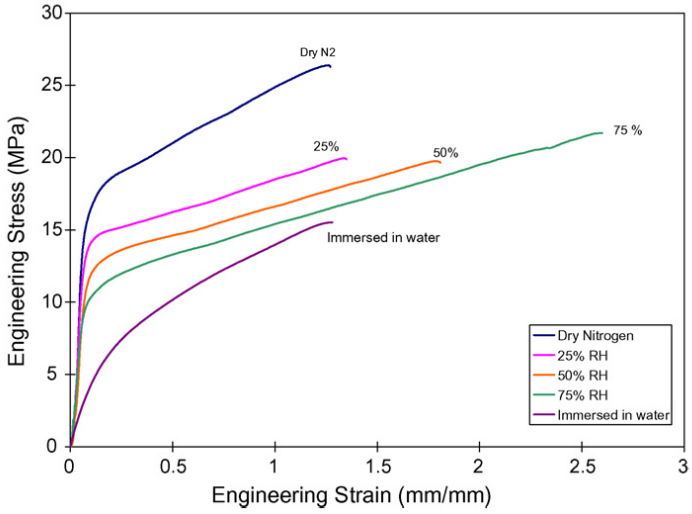

Figure 2-6. Stress strain curves of Nafion 111 at 25℃ with varying RH [7]

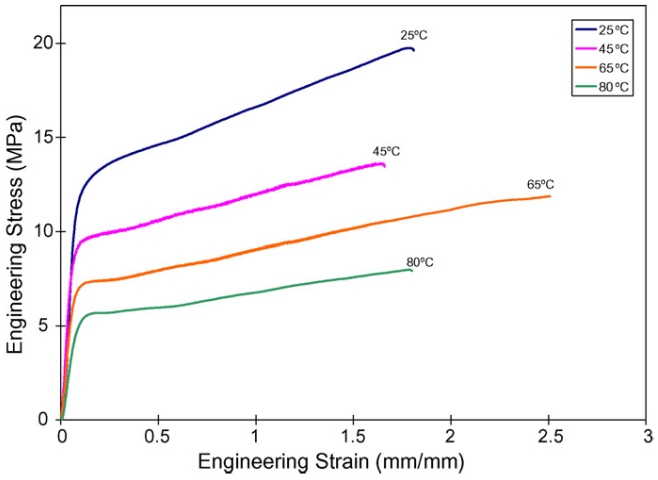

Figure 2-7. Stress strain curves of Nafion 111 at 50% RH with varying temperature [7]

These studies have numerically investigated the effect of clamping loads, cell geometry, membrane thickness and relationship between stresses and water uptake. It has been found that dimensional stability in the membrane is a key factor for membrane longevity as they govern the mechanical degradation mechanism [1]. The authors concluded that even though clamping forces and thickness affect the stresses in the membrane, water absorption induced swelling plays a more profound role [1, 2, 5, 8]. Different water profiles across the membrane were also been studied to evaluate stress distribution. It was found that a uniform water uptake profile ($\lambda_a = \lambda_c = 14$) leads to a uniform stress distribution on the membrane. Where $\lambda_a$is water uptake of anode and $\lambda_c$is water uptake of the cathode side. However, when the cell suffered from dry out ($\lambda_a = 6\ \lambda_c = 14$), a non-linear stress profile across the membrane emerged. It is important to remark that the stress gradient is always lower than the water gradient due to the decreasing modulus of the membrane with water content (as seen in Figure 2-6). The authors concluded that the membrane is more likely to suffer mechanical failure on the cathode side as electro-osmotic drag leads to more pronounced RH cycling on the cathode [2].

Further simulation studies were carried out to characterize the stresses in a membrane after hydration-dehydration cycles. This indicated that the membrane may not only suffer from compressive stresses upon hydration, but also of tensile residual stresses upon dehydration [6]. The authors also found that membrane failure forms are more likely to occur at the flow channels, as these regions experience more tensile residual stresses upon dehydration. These tensile residual stresses are believed to be the precursor of crack formation in the polymer membrane [6]. Cracks lead to leakage or gas crossover, leading to power loss and eventually to cell failure.

2.3 Current Methods for Measuring Membrane Swelling

Membrane swelling has been previously investigated in a number of different studies using both experimental and numerical techniques. This section reviews these methods and highlights the current gaps that this project attempts to fill.

A number of experimental studies can be found on the literature studying Nafion's stress-strain response [11, 21, 22, 23]. These studies have measured the stress strain-strain response, modulus of elasticity and stress to failure of Nafion membranes through tensile

testing. The response at different temperature and humidity values was reported by conducting tensile tests in environmental chambers with parameters representative of typical fuel cell duty cycles [11, 22]. Further studies have also analyzed the effect of adding catalyst coating [4], the response of membranes with a varying TiO2 concentration [24] and high strength ePTFE/PFSA composite membranes [23]. A similar study was carried by conducting tensile tests of Nafion membranes in environmental chambers at varying strain rates or inside water tanks [25]. These studies were carried out at temperature and humidity values typical of those in a fuel cell duty cycle, all tensile tests were carried out ex-situ.

Partially constrained swelling studies have also been carried out via bimaterial swelling [21, 26]. Nafion membranes were hot pressed onto a strip of a material of different mechanical properties. As the Nafion membrane is humidified, it tends to swell in all directions, however the second material hot pressed onto the membrane constrains the swelling in membrane plane [21]. This leads to bending of the bimaterial in the direction of the membrane, leading to a net compressive force on the membrane and a net tensile force on the second material. Stress estimations were based on the observed curvature of the membrane following the Stoney formula [21]. Strain was then calculated based on the modulus of the membrane and the material hot pressed to it. While Silberstein's and Boyce's study was carried out by humidified and membrane and observe it as it dried, Li et al observed the curvature for a number of different relative humidity values. Even though the bimaterial swelling is representative in terms that the Nafion membrane is constrained by GDL strips [21]or polyether ether ketone strips [26], these studies are carried out ex-situ. This type of study also fails to take in account the clamping force produced by the bipolar plates onto the membrane.

Optical measurements of Nafion swelling have previously been reported in the literature [27]. This study was carried out by placing the membrane sample in a chamber where both temperature and humidity could be controlled. The sensing element used in this study was an optical micrometer that could track the swelling behavior of the membrane with humidity changes [27]. Although the system is reported to have a high accuracy of 1 micron and a high degree of reproducibility, this study measured only bare Nafion membranes, with no GDL or GDE presence. Furthermore, this study measured swelling in

the planar direction, opposed to measurements in the thickness direction. Volume dilation was calculated by assuming the material to be isotropic.

The swelling behavior of Nafion membranes have also been studied through mass fraction change [28]. Membranes swelling or absorbance was measured by placing rectangular membrane films in tests tubes containing solutions of water and methanol of different molar fractions. The membranes were subsequently weighed at various time intervals to study their absorbance of species and mass gain.

A more recent study carried out by Eastman et al [29] has measured thickness change in Nafion thin films on substrates through X-ray reflectivity. Similarly to tensile tests of Nafion, X-ray reflectivity experiments were carried out in an environmental chamber with controlled temperature and humidity. Film thickness was then measured and tracked for a range or air relative humidity values by tacking the fringe frequency between the reflected signals from membrane and substrate. The authors have reported sub nanometer thickness changes with this technique [29], showing the high resolution of this method.

One shortcoming of a number of experimental procedures listed in this section is that thickness change is usually measured in the longitudinal direction, but not in the through thickness direction. Nafion swelling has also been reported to be anisotropic [2] due to the different constraints applied to the membrane while inside a fuel cell. The assumption of an isotropic swelling inside a fuel cell like environment may lead to errors in the estimation of thickness change. Mass fraction change experiments are limited to overall volumetric increase. While these experiments also measure the water content within the membrane, it is somewhat difficult to extrapolate the membranes mechanical response to this mass change. Furthermore to the knowledge of the author, all thickness change experiments carried out to date are limited to ex-situ experiments and they are able to measure total thickness change only. No through thickness strain distribution studies are currently available in the literature.

To address the lack of experimental observation of through thickness Nafion strain distribution, a number of numerical or modeling studies have been published [1, 2, 5, 8]. Tang et al [8] performed a finite element analysis and investigated the effects of plate alignment and membrane thickness. Solasi et al [7] studied the effect of changes in hydration, temperature, the presence of a hole at the center of the membrane, and the visco-

plastic response of the material. However, theirs models assumed a constant pressure applied by the bipolar plates, with all stress-strain being applied in the in-plane direction, opposed to the through the thickness direction. Kusoglu et al published a similar study on the mechanical behavior of Nafion under humidity cycles [2].

The unit cell model accounted for a fixed force exerting a pressure of 1 MPa on the membrane or fixed displacements. The stress-strain response was studied in both the planar and the through thickness directions. The authors found that for the given clamping conditions the through thickness strain was substantially larger on the channel section of the membrane when compared to the land section of the membrane. The study also concluded that stress magnitude decreases with increasing levels of anisotropy and that membrane thickness had a little effect on the calculated stresses. A follow up study by the same group [1], examined stress-strain behavior in the planar direction.

As discussed previously in this section, a variety of studies can be found on the open literature on strain measurements of Nafion membranes. However as it was previously mentioned, there is currently a lack of experimental studies that measure strain in the through thickness direction of the membrane with the potential of being carried in situ. As mentioned in chapter 1, this project focuses on a technique to accomplish this feat. Optical coherence tomography speckle tracking arises as an alternative to fill the gap. Section 2.4 gives an overview of this imaging technique and outlines its potential for measuring through thickness strain in Nafion membranes.

2.4 Optical Coherence Tomography

2.4.1 Introduction

Optical coherence tomography (OCT) is presented in this section as an image acquisition technique with the potential to measure through thickness strain in Nafion membranes. Section 2.4.2 briefly describes the operating principles of the system. Section 2.4.3 briefly describes the time domain systems and section 2.4.4 describes Fourier domain systems.

As mentioned in chapter one, the overall goal of this project was to develop a technique that would allow for non-destructive in situ studying and tracking of through thickness strain distribution of Nafion membranes. Imaging techniques were selected as the most

appropriate as they are non-contact and typically lead to low intrusion. The strain measurements carried out in this project were carried out through speckle tracking or digital image correlation (DIC). OCT was used as in order to acquire the images to be subsequently digitally correlated.

A number of different imaging techniques were considered in this project. The other techniques considered were: ultra sound, X-ray imaging, neutron imaging, and magnetic resonance imaging (MRI). However, ultrasound, MRI and neutron imaging were promptly discarded due to their low axial resolution compared to that of OCT [30, 31, 32, 33]. Although X-ray has been reported to achieve resolutions comparable to those of OCT [31, 34], this technique was also discarded due to its difficulty of imaging through metals. Furthermore, X-ray radiation exposure on fuel cell materials has been linked to performance loss for exposure times as short as tens of seconds [35]. Therefore, OCT was selected as the most appropriate technique for acquired in situ scans of fuel cell membranes due to its high axial resolution and low intrusion when compared to the other techniques. The next session describes the basics of OCT systems, theirs strengths and shortcomings along with the operating principles.

2.4.2 Operating Principles

OCT was first developed in the early 1990's as a high resolution technique for imaging of the retina and anterior eye [36, 37]. This technique is analogous to ultra sound in that it makes use of backscattered pulses from the sample it is imaging [38]. The difference is that while ultrasound uses backscattered high frequency sound waves, OCT makes use of backscattered light intensity [37, 39]. As a result, OCT systems typically have spatial resolution in the order of 1 to 2 orders of magnitude higher than ultrasound. Furthermore, the non-contact nature of this system makes it ideal for imaging with low intrusion. However, the system is limited to transparent and translucent media and has a limited penetration depth of typically 2-3 mm depending on the media [37, 39, 40].

OCT also differs from ultra sound in how the echo time delay is measured. As light travels extremely fast, it is not possible to directly measure time of flight of backscattered signals. Instead OCT makes use of a Michaelson type interferometer to acquire data, as

seen in figure 2-7 below [38]. This system may either work with low coherent light sources, or with the use of short pulses. When the backscattered light signals from sample arm and reference arm (refer to Figure 2-8) [38] match to within the coherence length of the light beam, the two signals interfere with each other. The intensity of light from the sample arm can be acquired by demodulating the intensity perceived by the detector.

The electric field incident by a light wave can be described at any given time as follows:

$$E(x, y, z, t) = a \cos[2\pi(vt - z\,\lambda)] \tag{2.1}$$

Where "a" is the amplitude of the light wave, v is the frequency, λ is the wavelength, t is time and z is the direction of propagation [41].

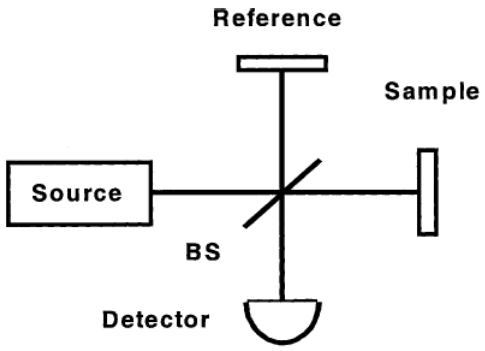

Figure 2-8. Michaelson type interferometer [38]

Equation 2.1 can also be written as:

$$E(x, y, z, t) = a \cos[wt - kz] \tag{2.2}$$

Where w = 2 πv is the circular frequency and k = 2 π / λ is the propagation constant.

By using a complex exponential representation, Equation 2.2 becomes:

$$E(x, y, z, t) = Re\{A\, exp(iwt)\} \tag{2.3}$$

Where Re denotes the real part of the Equation, A = a exp (-iφ) is the complex amplitude and φ = 2 $\pi z / \lambda$. Assuming that the signals from reference arm and sample arm propagate in the same direction at the same frequency, the complex amplitude at the detector arm A_d is given by:

$$A_d = A_r + A_s \tag{2.4}$$

The resultant intensity at the detector is:

$$I_d = |A_d|^2 \tag{2.5}$$

Which when expanded becomes:

$$I_d = |A_r|^2 + |A_s|^2 + A_r A_s^* + A_r^* A_s \tag{2.6}$$

$$I_d = I_r + I_s + 2\,(I_r I_s)^{1/2} cos\Delta\varphi \tag{2.7}$$

Where I_r and I_s are the intensities of the reference and sample arms respectively and $\Delta\varphi$ is the phase difference between reference and sample arms given by:

$$\Delta\varphi = \frac{\Delta p}{\lambda/2\pi} \tag{2.8}$$

Where Δp is the optical path length difference between reference and sample arms taking a refractive index n [41].

Based Equation 2.7, assuming that the intensity of the signal from the reference arm is constant, when the signal of the detector is measured, it is possible to demodulate the intensity of the sample arm. For more details on demodulating of the signal and derivations, please refer to reference [41].

Spatial resolution of an imaging system determines the ability of the system to distinguish between two different objects. The spatial resolution of a system is measured in units of length, typically in microns for OCT systems. The higher the spatial resolution of the system is, the smaller the distance between two objects that can be resolved. The spatial resolution of an OCT system can be further sub-divided into axial and lateral resolutions [42]. Axial resolution is the ability to resolve objects along the axis of the OCT light beam, whereas lateral resolution is the ability of the system to resolve objects perpendicular to the beam direction. The high axial resolution of the OCT systems is particularly important for the purposes of this thesis project as Nafion membranes can be very thin (i.e. 25 µm). If an axial resolution higher than 25 µm was used, the system would not be able to distinguish between upper and lower interfaces of the thin membrane, producing only one line. Therefore no depth information could be extracted from Nafion scans.

The axial resolution of an OCT system depends only on the coherence length of the light source. The coherence of light is related to how it correlates with a pure sine wave [43]. There are two types of coherence in light, temporal and spatial [43]. In simple terms, temporal coherence can be understood as how closely a light wave resembles a pure sine wave. Take for example a light wave that has its phase measured at a point P in space at

time t. If the light correlates perfectly with a sine wave, the phase could be predicted at any given time. However, in real conditions light waves exhibit a certain degree of uncertainty in their frequency [43]. The temporal coherence is a measure of the time period for which the estimation of the phase of the light wave remains accurate. High temporal coherence is necessary for interferometers such as the Michaelson type interferometer.

Spatial coherence is a similar concept to temporal coherence, but it differs from it in that instead of time it quantifies the phase relationship in space. Coherence length is used to quantify the degree to which a light wave is spatially coherent. Waves with high spatial coherence or long coherence length are displayed on Figure 2-9 below on the left hand side, while waves with short coherence length are displayed on the right hand side [37].

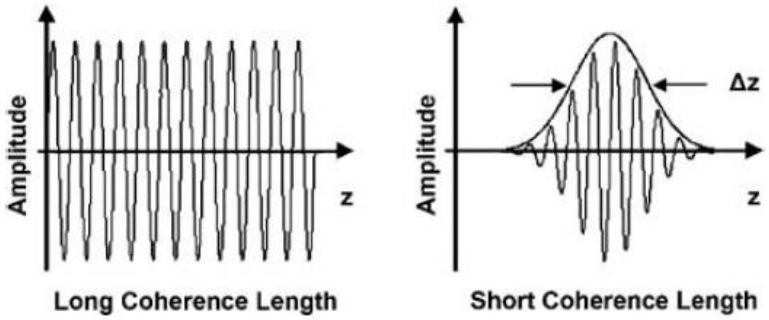

Figure 2-9. Waves displaying long and short coherence lengths [37]

OCT typically makes use of light waves with short coherence length (right hand side on Figure 2-9). This is because interference happens when signals coming from sample and reference arms match or are within the coherence length [37]. Hence the shorter the coherence length of the system the better the system is at resolving objects closely separated, and the system is said to have higher axial resolution. In other words, the axial resolution of an OCT system is determined by the coherence length of the light source [37] [38]. The coherence length is defined as the full-width at half maximum (FWHM) of the autocorrelation function, of simply Δz in Figure 2-8. For sources with Gaussian spectral distribution, the axial resolution of the system is given by:

$$\Delta z = \frac{2\ln 2}{\pi}\frac{\lambda}{\Delta\lambda} \tag{2.9}$$

Where "λ" in Equation 2.9 is the center wavelength and $\Delta\lambda$ is the FWHL of the wavelength range [42]. Δz is a common value for axial resolution and coherence length. There are currently some variation in how depth information is acquired in OCT systems. These are separated in time and domain systems and frequency domain systems. Sections 2.4.3 and 4.4.4 are brief introductions of how these systems physically work.

2.4.3 Time Domain OCT

When the principles of OCT were first published in 1991, the system made use of what today is known as the time domain configuration [36]. This is the simplest configuration and accepted as the easiest to analyze. This configuration makes use of a typical Michaelson interferometer as shown in Figure 2-7 above. The system can be implemented as either a free-space system or through the use of fiber optics as displayed in Figure 2-10 below. The time domain OCT system scans the samples in the axial and lateral directions. Axial scans, also referred to A-scans (refer to Figure 2-11 below) are scans through the depth of the sample being imaged. This is achieved by moving the position of the reference mirror of the OCT system. Interference between the two signals will only happen when the optical path length difference between reference and sample arms are within the coherence length of the light source. By adjusting the optical path length of the reference arm (scanning the reference mirror) depth information of the sample can be acquired. However the scanning depth is limited by the light source as light scatters in medium. A trade-off exists between axial resolution and penetration depth of A-scans, as the scatter light intensity greatly depends on the wavelength of the source [44] [37]. Longer wavelengths (lower frequency) provide for lower axial resolution but higher penetration depth, meanwhile shorter wavelengths (higher frequency) provide for increased axial resolution but are limited on penetration.

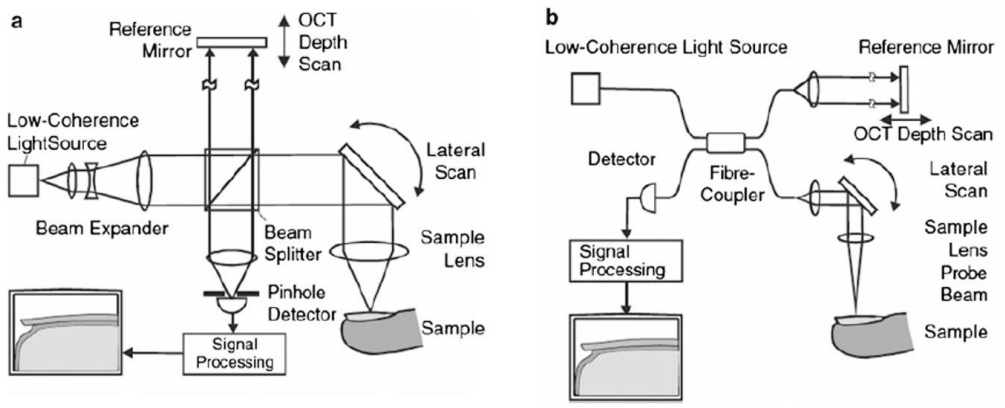

Figure 2-10. Schematics of time domain OCT systems a) free space system b) fiber optic system [24].

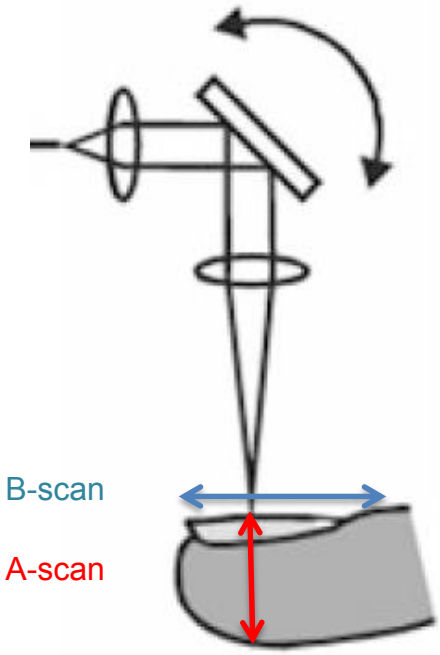

Figure 2-11. A-scans (red) and B-scans (blue) on a sample[24].

B-scans on the other hand are lateral scans across the transverse direction of the sample being imaged (blue arrow on Figure 2-11). B-scans can be thought of a collection of parallel A-scans across the transverse direction of the sample. The transverse resolution of the system is determined by the laser spot size at the focal point [38] [37]. High transverse resolution can be achieved by focusing the beam to a small spot size.

2.4.4 Fourier Domain OCT

Fourier domain OCT works on a similar fashion to time domain OCT, with the difference that it excludes the need for the time consuming a scanning mirror [39, 45, 46]. The backscattered signal in spectral domain OCT systems is acquired by the inverse Fourier Transform of the spectrum of either spectral interferometry or wavelength tuning of the light source [45]. The advantage of Fourier domain system is a much higher acquisition rate from about 400 A-scans per second in the time domain to up to 40,000 A-scans per second in the frequency domain. Currently there are two types of Fourier domain systems: spectral domain and swept source OCT. For brevity only a short description of the system is given here, for more detailed information please refer to references [39, 45, 46].

The typical setup of a spectral domain OCT system can be seen on Figure 2-12 below. The main differences to a time domain system are in that the reference mirror is fixed in position, the light source differs and the presence of a photo detector array.

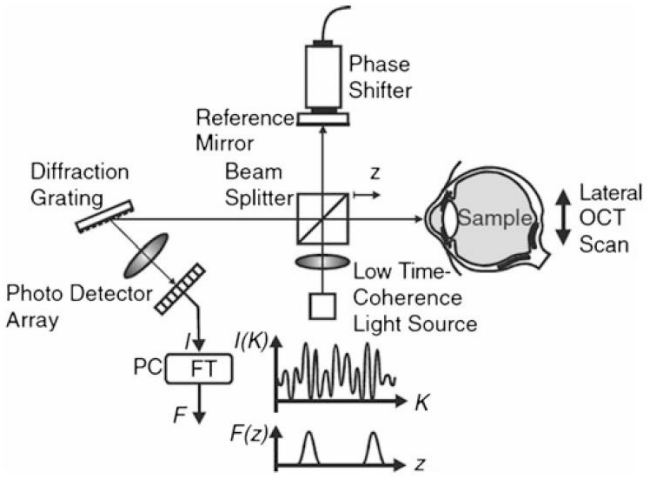

Figure 2-12. The typical setup of a spectral domain OCT system.

The light source in the spectral domain OCT system is made of many different wavelengths that are fired simultaneously. The backscattered reflections interfere with reference light from the reference mirror and are directed to a diffraction grating where the wavelengths are split. A photo detector array then separates the different wavelengths and their intensities are detected by photodetectors. An inverse Fourier transform of the data is

then taken to convert it from the frequency domain to time domain, giving results of the same fashion as those of the time domain system.

The swept source OCT system is similar to the spectral domain OCT system, but this system makes use of a light source with tunable wavelength. Each wavelength is fired separately and interfered with its reference beam. The interference intensity is recorded and the next wavelength is then fired, excluding the need for a photo detector array [45]. The obtained data is then inverse Fourier transformed to the time domain in the same fashion as the spectral domain OCT system.

2.5 Elastography and Speckle Tracking

2.5.1 Principles

Elastography is a commonly used method for the estimation of elastic properties of soft tissue through imaging techniques [47]. This technique has been extensively used coupled with ultrasound as the image acquisition system [48, 49]. More recently the technique has also been demonstrated to work coupled with OCT, as a means to image micrometer level strain [49]. The advantage of OCT elastography over ultrasound elastography is the much higher resolution that can be achieved through OCT as mentioned in section 2.4.

Speckle tracking is carried out thorough cross correlation of two successive frames of the object being imaged. An algorithm is used to correlate images prior and post deformation in order to calculate relative motion. A number of different algorithms have been reported in the literature [50]. These algorithms work by discretization of the image and further block-matching, as seen in Figure 2.12 below. Blocks called subsets or kernels are defined over the domain in the reference image and the deformed image. The mean intensity of these blocks in the reference image “r” and in the deformed image “d” are correlated for tracking of relative motion. In this project we make use of the normalized correlation as it is accepted as the most accurate over a range of different subset sizes [50]. The algorithm used in this project is an open source MATLAB code [51]. Firstly the algorithm discretizes the image domain into control points in the reference image and the deformed image [51]. The amount of control points is the same for the reference and deformed images, but it may be controlled by the user. A greater number of control points leads to more displacement information of the images, but also increases the computational effort. The algorithm then

averages the mean pixel intensity of subsets around each control point (red box in Figure 2-13) [51]. The subset size can be controlled by the user, however the subset size may alter the calculated results, as mentioned in section 2.5.2. The search zone area is set as four times bigger as the subset area (twice the width and twice the height) as default. However, this value can also be changed if necessary. The correlation is then carried out as described by Equation 2.10 below:

$$C(u',v') = \frac{\Sigma_{x',y'}\left[\left(r(x',y') - \bar{r}_{u',v'}\right)\left(d(x'-u',y'-v') - \bar{d}\right)\right]}{\left\{\Sigma_{x',y'}\left[\left(r(x',y') - \bar{r}_{u',v'}\right)^2\right]\Sigma_{x',y'}\left[\left(d(x'-u',y'-v') - \bar{d}\right)^2\right]\right\}^{1/2}} \qquad 2.10$$

The algorithm correlates intensities "r" and "d" for reference and deformed images respectively. This correlation is carried out for a number of theoretical displacements u', v' in the x and y directions respectively. This is done in steps of 1 pixel inside the search zone in the reference image, as seen in Equation 2.10 above. The terms x', y' are the local subset coordinates. The theoretical displacement with highest correlation coefficient for a given control point between reference and deformed images is therefore taken as the real displacement between the two images.

The output of the auto correlation algorithm can be selected to be either a vector field, contour plot or a numerical representation of displacements. When in a vector field, the tail of the arrow represents the position of each control point in the reference image and the tip represent its position of the control point in the deformed image. In the contour plot, each control point is represented as a coloured pixel. The colour of each control point represents the amount of pixels it was displaced (in the x or y directions).

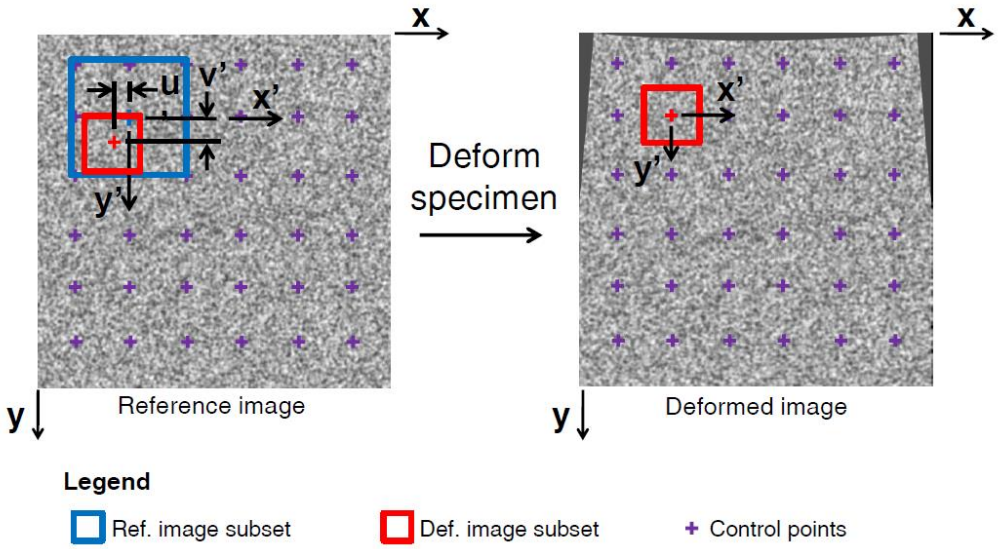

Figure 2-13. Geometry of the search region [51]

Control points that are assigned the colour white represent points where the solution is below the set minimum threshold value. Threshold values van also be modified by the user. The value used in this project was of 0.7.

2.5.2 Effect of Subset Size on Relative Displacement

As it has been reported by Rogowska et al. while carrying out OCT elastography, that the size of the processing kernel or subset size is an important parameter [32]. By selecting the wrong kernel size, the calculated strain may be under or over estimated. The selection of the adequate kernel size depends greatly on the media being imaged, its contrast, speckle pattern, mean displacement and algorithm used. The bigger the subset size the more information is used for the correlation of each control point. However, greater subset sizes will lead to an averaged displacement of the control point, instead of localized results. The careful selection of appropriate subset size is imperative for accurate results.

In order to find the ideal kernel size, Rogowska et al. compared their OCT elastography results to calculated mean axial displacement using Hooke's law. For a variety of different subset sizes used in their experiment, they concluded that a kernel size of 41 X 41 pixels showed the results with the lowest error for their imaging medium [32]. It is therefore imperative to firstly optimize the subset size prior to carrying out a quantitative analysis of

membrane strain. This is done by comparing the elastography strain results for a number of different subset sizes to a known measured strain quantity. This process is carried out as described in section 3.4.

2.5.3 Contrast Agent

The previous section covered the principle of speckle tracking and how it is a useful technique for measuring localized strain in translucent media. However, Nafion membranes tend to be transparent and homogeneous. While this might be beneficial for the operation of the fuel cell, it makes speckle tracking rather difficult. In order for speckle tracking to be considered an option, the media being imaged needs to possess speckles. In other words, speckle tracking would be virtually impossible in a homogeneous medium as there are no speckles to be tracked. Figure 2-14 below shows an OCT scan of a bare Nafion membrane. The green contour represents the physical geometry of the polycarbonate flow field plate. These lines were added for easier understanding of the image. As it can be seen, two distinct horizontal white lines make up the interfaces of the Nafion membrane. However, there is no information from within the membrane.

This setup would allow for thickness change measurements to be carried out. In other words just the distance between top and bottom interfaces of the membrane can be tracked or its thickness change. However, though depth localized strain cannot be calculated as there are no information to be tracked. To make up for this shortcoming, a contrast agent is used, which causes the membrane to scatter light adding a speckled pattern to the membrane when visualized in an OCT system. A contrast agent can be considered to be any substance used to provide or enhance the contrast in the body being imaged. The use of contrast agents has been previously demonstrated in OCT elastography making use of charcoal [47]. The authors created phantoms made up of gelatin and used activated charcoal as the contrast agent. Ideally the contrast agent would possess a different refractive index as the rest of the media, enhancing the contrast between the two bodies. Gold nanoshells and titanium dioxide nanoparticles have also been reported in the literature as contrast agents used in OCT imaging of skin [52, 53].

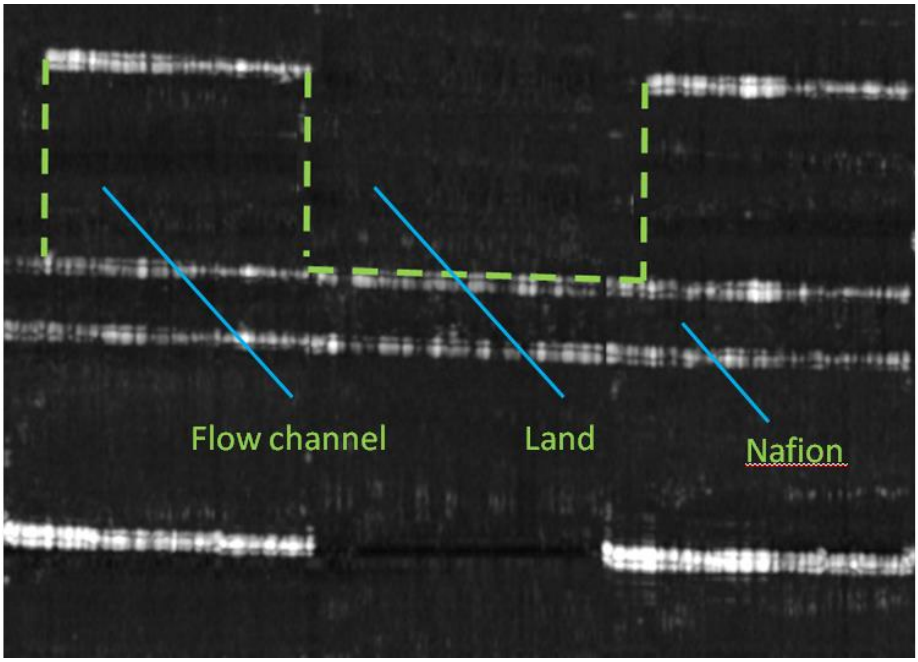

Figure 2-14. OCT scan of a standard Nafion membrane

In a study published in 2009, Kirillin et al used a system with an axial resolution of 15 µm in air, while the TiO_2 nanoshells were about 100 nm in diameter and gold nanoshells were roughly half of that. It is important to note that the OCT system cannot resolve each individual nanoparticle. Instead the contrast agent produces enhanced backscatter [54] and creates a random speckled pattern which is then tracked by an algorithm. An example of enhanced information within a sample due to the addition of a contrast agent can be viewed in Figure 2-15 below. This random speckled pattern may sometimes look similar to white noise, it would therefore be impossible for it to be tracked by the human eye. However, computer codes are more than able to track specific patterns of kernels and generate a strain map. While selecting a contrast agent it is important to consider that its incorporation might alter the mechanical properties of the media being imaged. It is therefore important to keep concentrations of contrast agents to a minimum whenever possible.

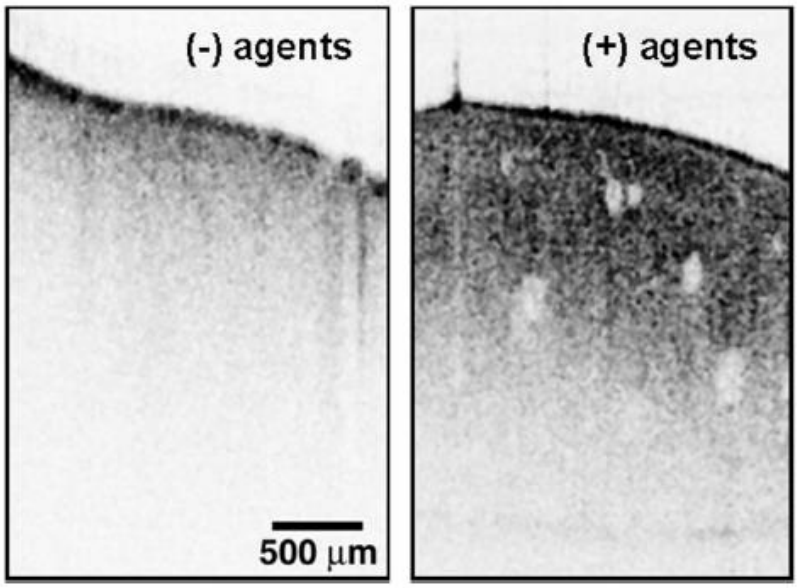

Figure 2-15. OCT scan of mouse liver enhancement with gold nanoshells contrast agent [54]

It has been found that gold nanoshells require a much smaller concentration than TiO_2 nanoparticles (about two orders of magnitude) for the same contrast to be achieved [52]. In the other hand, recent studies have been conducted mechanical properties of Nafion-TiO_2 composite membranes and their impact on performance of PEM fuel cells [11, 55]. As the mechanical properties of Nafion-TiO_2 have already been reported in the literature for different concentration levels [11], this was selected the contrast agent of choice for this project as there is a degree of predictability for the impact of TiO_2 on mechanical properties of Nafion. More information of the effect of TiO_2 on the mechanical properties of Nafion membranes can be found on section 2.6

2.6 Properties of Nafion-TiO_2 Composite Membranes

Nafion-TiO_2 composite membranes were used in this project as titanium dioxide is a strong contrast agent and the mechanical properties of these membranes have already been subject of study. The contrast agent is necessary in order to acquire through depth information of the membrane and carry out speckle tracking, as mentioned in chapter 2. In theory a number of different contrast agents would work for creating a speckled pattern in the membrane. However, the mechanical properties of Nafion-TiO_2 are well documented.

Therefore it is somewhat possible to predict was the mechanical response of the membrane would be under certain conditions. This section summarizes the mechanical properties of Nafion-TiO_2 composite membranes.

It has been reported that due to its hydroscopic properties, Nafion-TiO_2 composite membranes have enhanced water retention capabilities [11]. This allows the membranes to stay hydrated at temperatures close to 100 ^oC, while enhancing the current density in up to 1.5 times when compared to standard Nafion membranes [55]. It has been reported that the addition of this contrast agent into Nafion may alter its microstructure, affecting its mechanical properties [11]. In previous studies, Satterfield et al. carried out stress-strain tests in Nafion-TiO_2 composite membranes of different contrast agent concentrations [11, 24]. The procedure for membrane preparation carried out by Satterfield et al was the recast method, similar to the procedure carried out in this project. The authors found that an increasing concentration of TiO_2 lead to an increase in the elastic modulus and a decrease in plastic modulus, as shown in Figure 2-16 and Figure 2-17 below.

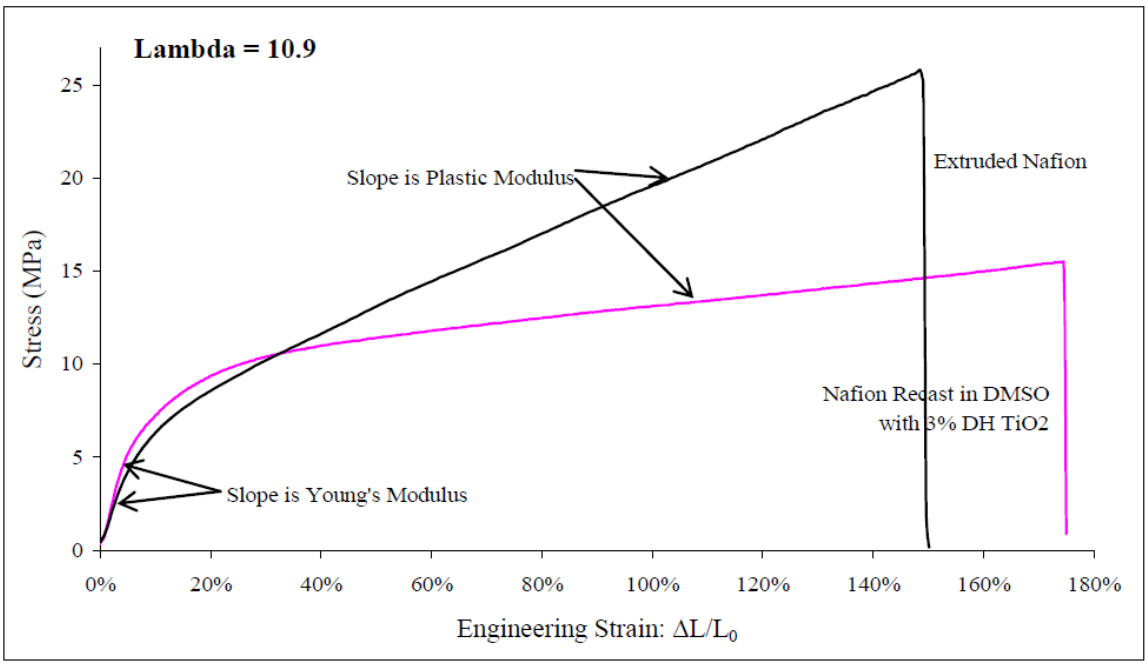

Figure 2-16. Stress-strain curve for Nafion and Nafion-TiO_2 composite membrane C = 3% wt at lambda = 10.9 at room temperature [11]

Satterfield et al. found that a 3 % wt concentration of titanium dioxide at room temperature leads to a small impact on the elastic modulus and yield point. Greater differences are observed in the plastic modulus and stress and strain to rupture. Figure 2-17 meanwhile shows the results for a membrane with a far higher concentration of titanium dioxide. Under a concentration of 30 % wt of contrast agent the yield point increased from approximately 4 MPa to approximately 7 MPa, while the Young's modulus curve is significantly more pronounced. The increased concentration of TiO_2 also leads to a much more significant change in strain to rupture, enhancing the materials ductility. However, the comparison was made between recast composite membranes and extruded Nafion. The fabrication method is likely to also impact the mechanical characteristics of the material.

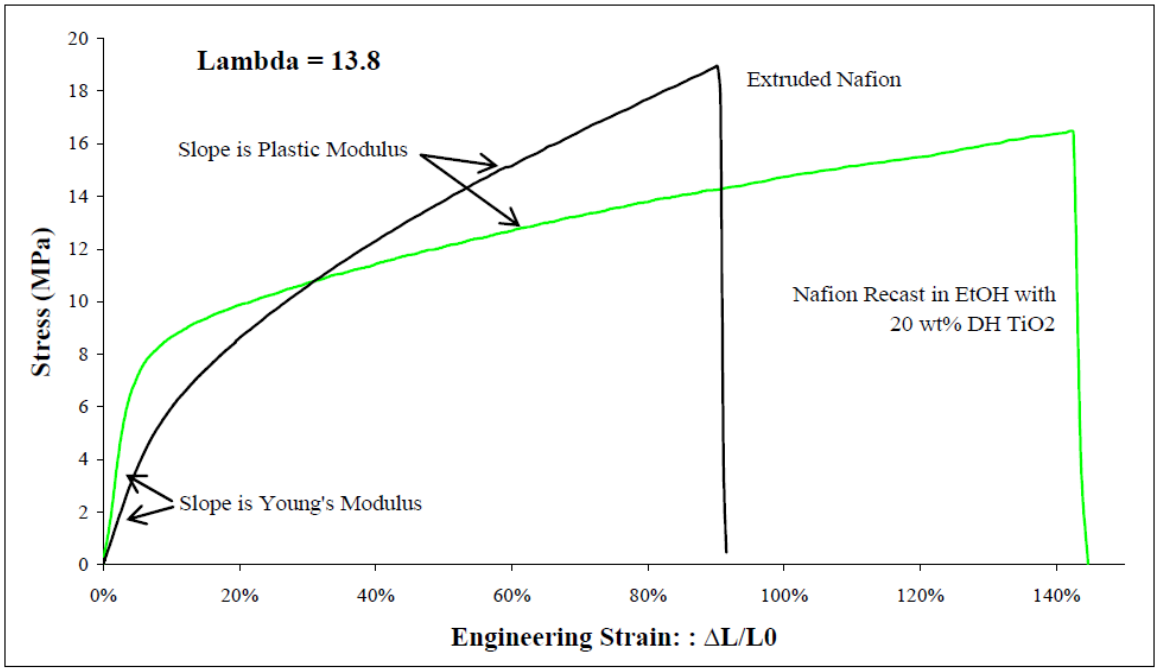

Figure 2-17. Stress-strain curve for Nafion and Nafion-TiO_2 composite membrane C = 30% wt at lambda = 13.8 at room temperature [11]

A similar procedure was repeated at a temperature of 80 °C as seen in Figure 2-18 [11]. Only a small change in stiffness is noticed with increasing concentration of titanium dioxide. The authors mention that stress-strain tests are subject to errors and that normally at least 5 tests of a specimen type should be carried out for more precise results, however due to limitation of materials only 2 specimens of each concentration were available. The authors believe that this explains the apparent increase in stiffness from 2 particular data

points. The authors believe that this apparent increase is linked to experimental errors and that the material undergoes a very small change in stiffness with the small titanium dioxide concentrations used as seen in Figure 2-18.

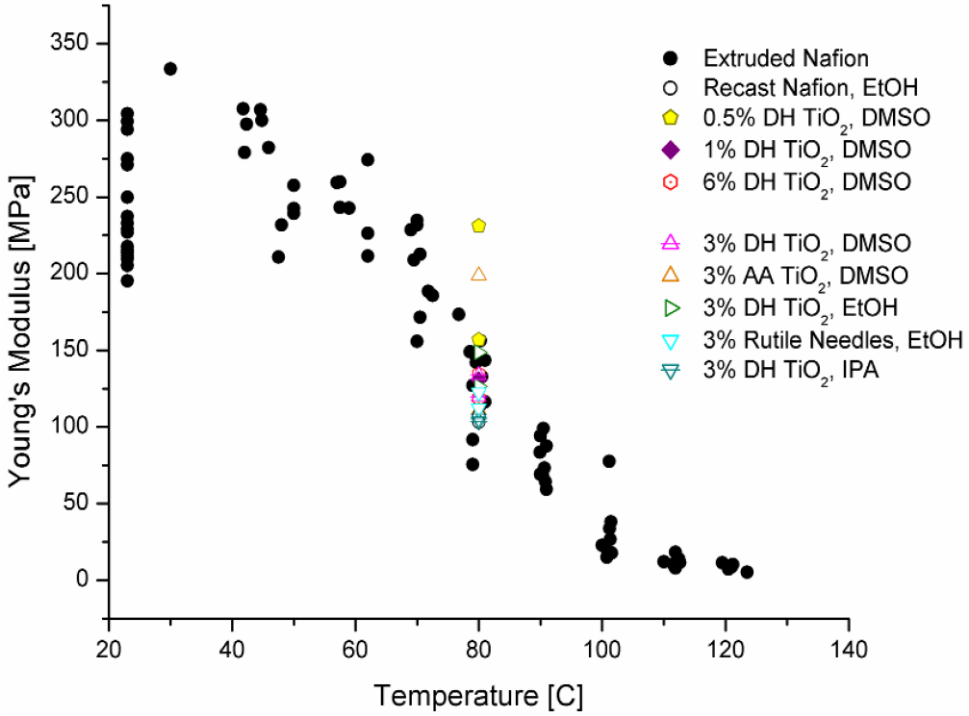

Figure 2-18. Young's modulus for Nafion-TiO_2 membranes at 80 °C [11]

It was found that for elevated temperatures closely resembling those of an operating fuel cell, the concentration titanium dioxide had little effect on the mechanical properties of the membrane. The authors also studied the water sorption of the Nafion and Nafion-TiO_2 membranes by measuring the weight of membranes inside a chamber at 100% RH at 50 °C as seen in Figure 2-19 [11]. The authors also found that there was an almost unnoticeable change in the water sorption dynamics of the membrane regardless of TiO_2 concentration. Perhaps the most noticeable difference is in the desorption dynamics of the composite membranes (right on Figure 2-19). The Nafion-TiO_2 membranes did seem to have an increased water retention capability. However, that should lead to little to no impact in the swelling behaviour of the membrane with humidity.

The titanium dioxide concentrations used in this project were even lower than those used by Satterfield et al. Therefore it is expected that for the lower concentrations used in this

project i.e. 0.1, 0.2 % wt, the change in mechanical properties compared to those of bare Nafion should be almost unmeasurable.

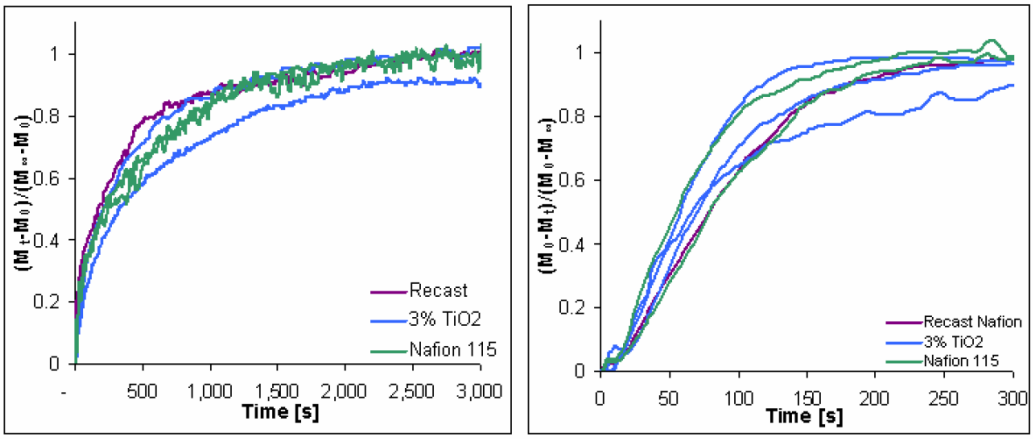

Figure 2-19. Water sorption (left) and desorption (right) dynamics of Nafion and Nafion-TiO_2 composite membranes at 70 °C [11]

2.7 Speckled Noise and Filtering

It has been observed in a number of studies the formation of noise taking the shape of random speckled patterns in OCT images [40, 45, 56]. The source of said speckle noise is not yet well understood and only a small number of publications have focused on the topic [40]. However, it is believed that the main sources of these speckles is due to the inference of ligth waves with random phases, and the presence of multiple scatterers within the imaging sample [45, 56]. For more information on the source of speckled noise in OCT scans, the reader is fowarded to references [40, 45, 56]. This speckled noise differs from the speckles present in the membrane that used for DIC. This speckled noise is randomnized and is present in the entire OCT scan. For clarity, this speckled noise is refered to as unsusable speckles. The speckles that make up the membrane are created by the presence of the contrast agent. This speckle formation is vital for speckle tracking or digital image correlation. This speckle formation is refered to as usable speckles or speckled pattern.

The presence of the unusable speckled noise becomes of increased importance when cross correlation between images is carried out. The random unusable speckled noise in images may affect cross correlation thus impacting the apparent strain calculations [49].

Some techniques for reducing this unusable speckled noise have been mentioned in the literature. Perhaps the most common and simplest is the “spatial compounding” or “spatial diversity processing” [40, 56], as it requires no hardware modification. This technique simply averages the intensity values of multiple b-scans taken at the same location or slightly displaced locations [56]. If the technique was to be applied with multiple scans of the exact same location, it is believed that unusable speckled noise could be averaged out while not affecting the membrane usable speckled pattern. The usable speckled pattern in the membrane undergoes slight alterations when B-scans are acquired in slightly different locations. Therefore, if this technique was to be carried out with b-scans at slightly different locations, membrane speckles could potentially be averaged out, leading to loss of information within membrane material.

2.8 Summary

This chapter highlighted the importance of Nafion membranes in the operation of hydrogen fuel cells. As mentioned in section 2.1, the membrane operates a physical boundary between anode and cathode preventing gas crossover and allowing for protonic transport.

Section 2.2 focused on Nafion, which is currently the material of choice for electrolyte membranes in hydrogen fuel cells. Nafions structure is of great importance to the proper functioning of the fuel cell. The copolymer is composed of semi-crystalline chains of polytetrafluoroethylene (PTFE) giving the material its physical integrity and ionic side chains that allow for the transport of species. Proper humidifying of Nafion membranes is of great importance for ionic transport through the membrane. However, the material undergoes a mechanical response to water content by undergoing swelling. As water is formed in the cathode as a by-product of the electrochemical reactions of the fuel cell by, water management plays a key role for proper functioning and extended lifetime. Dynamic load cycles lead to hygro-thermal cycling of the membranes imposing swelling-shrinkage

cycles of the material. This mechanical response is believed to be the main cause of mechanical degradation in Nafion membranes, impacting fuel cell the life cycles.

Section 2.3 reviewed current techniques listed in the literature for measuring swelling-shrinkage strain in Nafion membranes. It was found that most of the current experimental techniques available in the literature carried out ex-situ testing of the material. Tensile testing of Nafions stress-strain response [11, 21, 22, 23] is seemingly a popular technique for ex-situ testing of the materials mechanical behaviour. Other techniques such as biomaterial swelling, optical micrometer measurements, mass fraction change and x-ray reflectivity have been used to measure membrane swelling in a number of different conditions change [21, 26, 27, 28, 29]. These techniques all have in common that they are only able to measure the mechanical response of the material ex- situ. It was found that there is currently a lack of studies analysing the in situ behaviour of the material. Modelling studies have also been published in the literate, where the membrane was studied under more representative conditions [1, 2, 5, 8]. Although these studies seem to show good correlation to experimental studies, their focus was largely on stress distribution and in plane strain. Little has been done to date on through thickness strain distribution.

Section 2.4 introduces OCT as a potential technique for acquiring images of Nafion membranes in situ. These images were further used to calculate thought thickness strain distribution in membranes through digital image correlation. This section also overviewed the basics of OCT systems and explained the basic operating principles. As mentioned in section 2.4 Oct was selected as the imaging technique most appropriate for this project due to its high axial resolution and low intrusion levels.

The technique to be used for measuring strain through OCT images is described in section 2.5. Speckle tracking or digital image correlation studies images prior and post deformation and through an algorithms determines relative motion between them [50, 51]. The algorithm works by discretizing the images in several points called control points. A kernel or subset is defined around each control point and its intensity is recorded. The algorithm then correlates the intensities between reference and deformed images for a number of theoretical displacements. Section 2.5 also mentions the impact of subset size on relative motion calculations and the importance of a reference measurement in order to estimate the most appropriate subset size. The reference measurement technique is

mentioned in section 3.4. It is of importance for speckle tracking that the imaging media contains a speckle pattern. Due to Nafions homogeneity and transparency it produces no speckles when scanned by an OCT system. Therefore the introduction of an optical contrast agent is necessary. Titanium dioxide powder was introduced in section 2.5.3 as a potential candidate for an opctical contrast agent for Nafion membranes.

Nafion-TiO_2 provides the necessary usable speckled pattern to be used in speckle tracking and tack swelling strain. However the introduction of mentioned contrast agent alter the mechanical properties of the membrane. A number of studies been published on the topic found that the use of TiO_2 in Nafion membranes lowers the materials elastic modulus, leading to higher strains in the elastic region of the membrane [11, 24]. It is therefore imperative to keep the contrast agent concentration to a minimum in order not to affect the mechanical behaviour of Nafion.

A number of studies have observed the presence of noise in OCT scans [40, 45, 56]. This noise when superimposed onto the membrane seciton of the OCT scans may lead to erroneous results or poor correlation between images. In oder to remove this unusable speckle noise, some filtering techniques have been stueided [40, 56]. One such filtering method is the spatial diversity technique. The filtering is carried out by taking several scans of the exact same location over a short period of time. As the noise is randomnized, it presents a different pattern for each scan. However, when these scans have their intensities avergaged, the speckled noise dissapers when the number of images being used is large enough. It is important however to carry out the spatial diversity technique statically, in order not to affect the speckled pattern of the Nafion membranes.

Chapter 3: Experimental Methods and Procedure

3.1 Overview

This chapter describes in detail the experimental setup used in this project, i.e. the ex-situ cell and the in-situ cell. The functions of each cell along with specifications are covered in this chapter.

Section 3.2 details the equipment and cells used in the experiments carried out in this project.

The membrane preparation procedure is detailed in section 3.3. The steps carried out for preparation of PDMS-TiO_2 and Nafion-TiO_2 composite membranes is detailed in this section.

The preliminary tests carried out for methodology validation are detailed in section 3.4 of this chapter.

The experimental procedure carried out during testing is explained in sections 3.5. This section is divided in the two types of experiments that were carried out in the ex-situ cell, i.e. pressure control and humidification and the procedure carried out for humidification tests in the in-situ cell.

3.2 Experimental Setup

Two cells were designed for the experiments carried out in this project: the ex-situ test cell and the in-situ test cell.

The ex-situ test cell was designed with the aim to allow for OCT scans of the membrane to be taken in order to study thickness change. However noted earlier, the subset size taken in speckle tracking may affect the relative displacement estimations. Therefore a comparative technique must be used in order to find the appropriate subset size. Microscope images of the membrane were acquired for this purpose. Thickness change results of both techniques were compared in order to find the appropriate subset size and validate OCT as a technique to measure membrane thickness change.

The in-situ cell was designed to be able to potentially operate as a PEMFC and demonstrate that it is possible to acquire membrane information through OCT scans from

a working fuel cell. The cell follows the design of a standard PEMFC as closely as possible, with minimal modifications to allow the OCT laser beam to reach the membrane.

3.2.1 Ex Situ Test Cell

This section describes the design and specifications of the ex-situ test cell and the experimental setup. Two types of tests were carried out with this setup: the compression tests and humidification tests. Compression tests require control of the clamping pressure applied to the membrane while humidification tests require control of temperature and relative humidity of the membrane.

The ex-situ cell makes use of polycarbonate plates with machined channels rather than a graphite flow field plate, commonly found on PEMFCs. Polycarbonate was used due to its transparency, allowing the OCT laser beam to reach the membrane. Polycarbonate is also relatively rigid when compared to a Nafion membrane, this allows for the polycarbonate plate to mimic the physicals constraints imposed on the membrane by graphite plates in actual PEMFCs. A Schematic of the polycarbonate flow field plate can be seen in Figure 3-1 below.

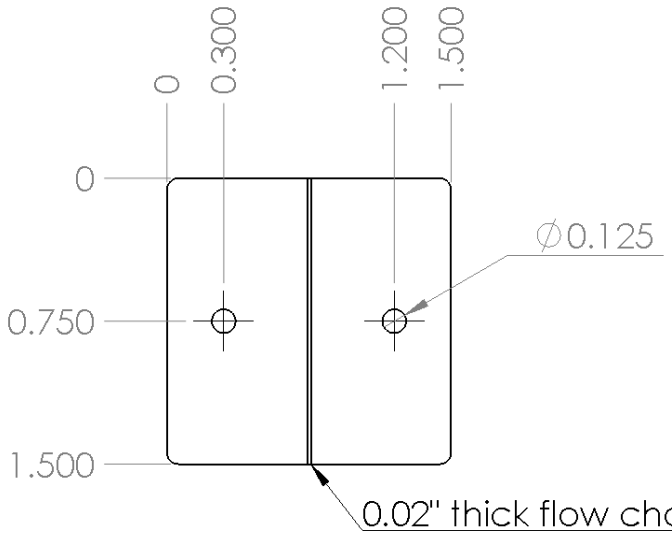

Figure 3-1. Drawing with dimensions of polycarbonate flow field plates

The plates used in this experiment were fabricated out of a 0.08 inch thick polycarbonate plate. The plates were cut to a squared profile with dimensions of 1.5 X 1.5 inches. Two

clearance holes of 0.125 inches were drilled for fitting dowel pins for alignment. A 0.02 inch thick flow channel can also be seen in Figure 3-1. For ease of visualization only 1 flow channel is shown in Figure 3-1, however the plate was manufactured with 15 flow channels machined in parallel. All parts of the ex-situ cell were designed and sketched for fabrication using CAD software Solid Works.

Figure 3-2 below shows a schematic of a side view of a Nafion membrane sandwiched by two polycarbonate plates. Green arrows show the direction of the compressive force applied. The red arrow shows the direction of the incoming OCT laser beam and the blue arrow show the direction the microscope points at. Figure 3-3 shows a representation of the approximate field of view of the OCT scan (red rectangle) in a front view of the polycarbonate plates and the microscope field of view (blue rectangle) on a top view of the polycarbonate plates sandwiching the membrane.

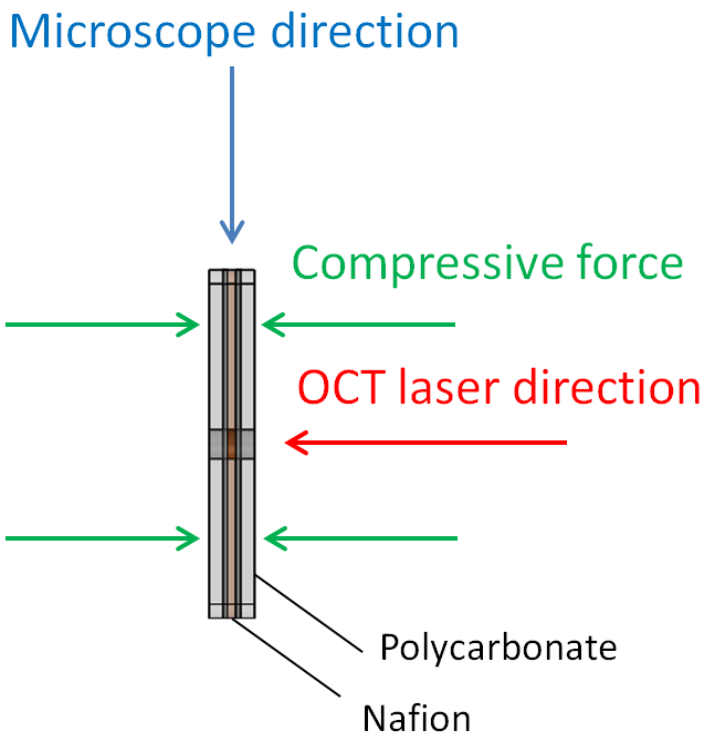

Figure 3-2. Side view of Nafion sandwiched by polycarbonate plates

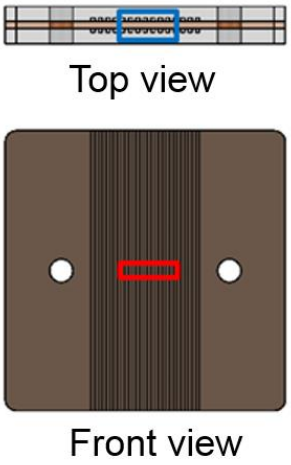

Figure 3-3. Front and top views of polycarbonate plates sandwiching membrane showing microscope and OCT fields of view

A pneumatic setup was used in order to apply and control the clamping pressure on the membrane. Aluminium plates were used to ensure that a constant pressure was applied on the surface of the polycarbonate plates. An exploded view of the pneumatic device can be seen in Figure 3-4 below and a section view in Figure 3-5.

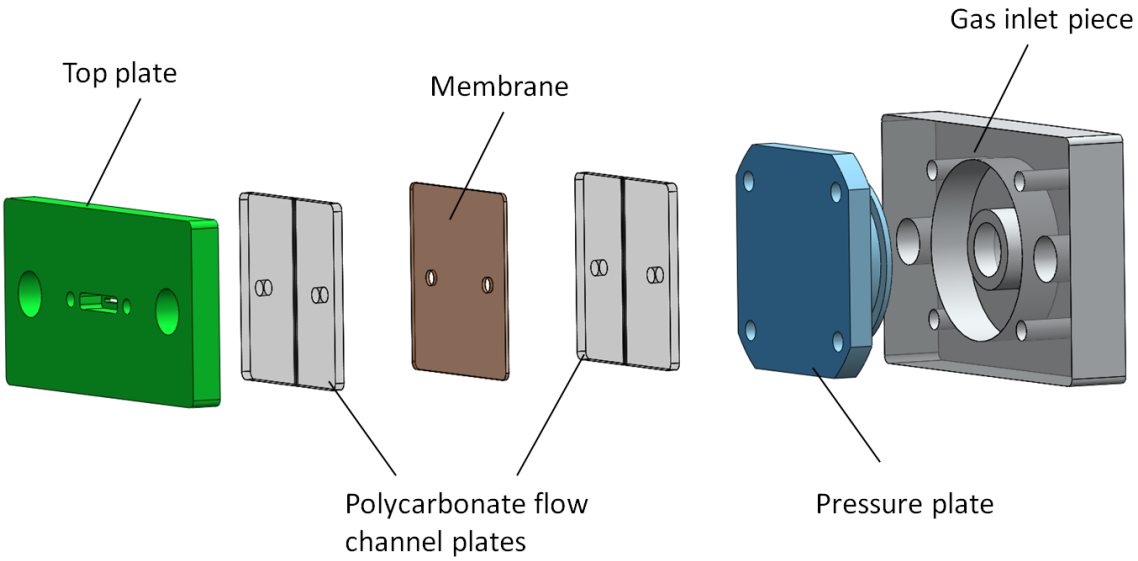

Figure 3-4. Exploded view of pneumatic device.

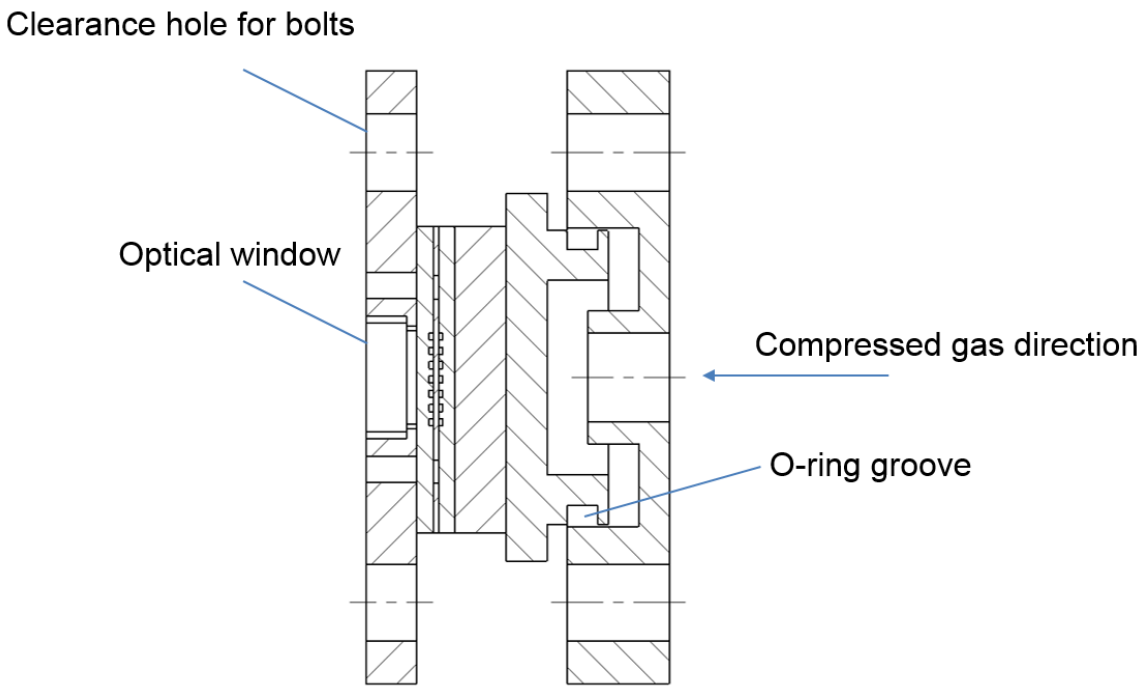

Figure 3-5. Section view of the pneumatic device.

A nitrogen tank coupled with a regulator was used for the experiments carried out in this project due to the inert properties and availability of nitrogen tanks at the facilities where the experiments were carried out. By controlling the pressure at the regulator mounted to the nitrogen tank, the applied pressure at the pressure plate (refer to Figure 3-4 and Figure 3-5) could be controlled. Bolts were coupled with nuts to fasten the gas inlet piece to the top plate (refer to Figure 3-5) ensuring a pressure was applied to the membrane once nitrogen was pumped in. Care was taken not to pre-apply any pressure to the device while tightening the bolt-nuts assembly. The top plate also features an optical window so the membrane/flow plates can be scanned while a pressure is being applied. The pressure plate features a groove for an o-ring in order to avoid leakage and ensuring repeatable results. In order to check for leaks, the device was pumped to 150 psi and left overnight. There was no measurable lost in pressure within the resolution of the pressure measuring device (about 0.1 psi). Figure 3-6 shows the remaining components of the pressure control device. The gas inlet piece was horizontally mounted to an “L” shaped support piece which is mounted to a 3-Axis stage (refer to Figure 3-6).

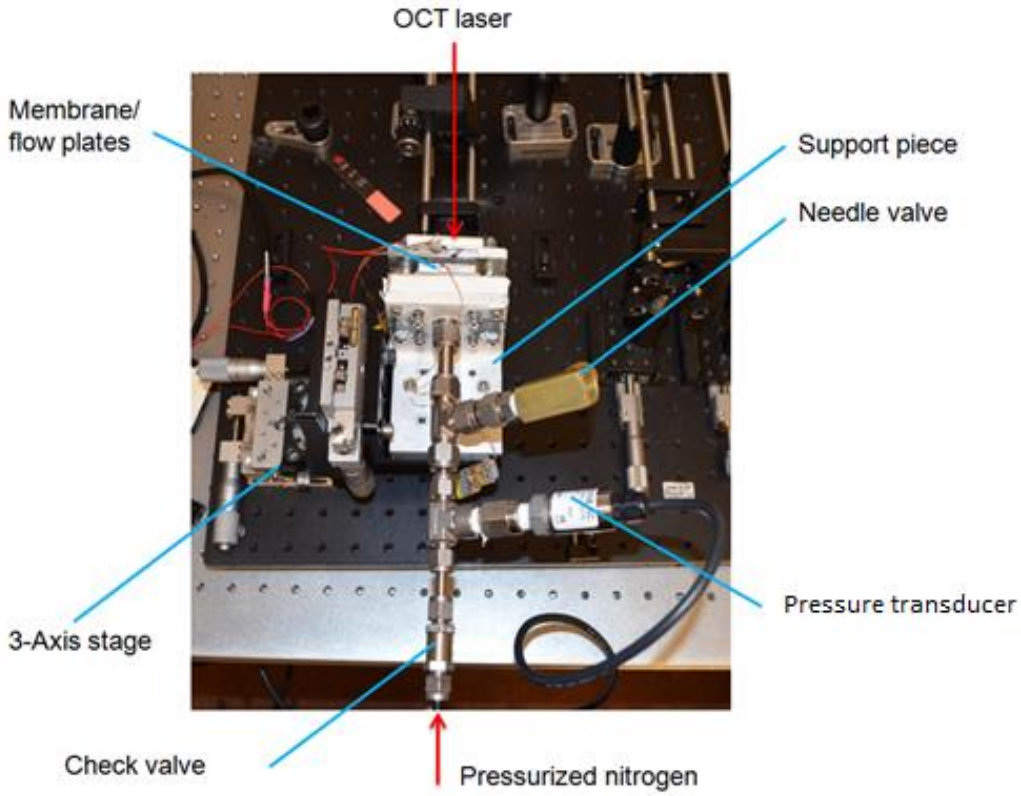

Figure 3-6. Top view of pressure control device

The 3-Axis stage was used to allow for fine adjustment of the position of the ex-situ test cell. A pipe was connected to the support piece, which delivers pressurized nitrogen to the gas inlet piece incoming from the nitrogen tank. The system is also mounted to a check valve (SS-4C-1, Swagelok) in order to avoid leakage. A pressure transducer was fitted to the assembly (PX309-150G5V, Omegadyne INC.) in order to allow pressure readings to be taken. A needle valve (En 20 B, Deltrol) was used to release the pressurized nitrogen once experiments are completed.

Flexible heaters (KH – 202/10, Kapton) and thermocouples were placed in the system to allow for controlling the temperature of the membrane. A little section of the polycarbonate plates was machined in order to fit a combined relative humidity and temperature sensor (SHT75, Sensirion) for monitoring membrane conditions (refer to Figure 3-7). A small pipe was also connected to the bottom of the system in order to provide humidified air to the membrane incoming from a fuel cell test station (850 E, Scribner Associates on loan from NRCC).

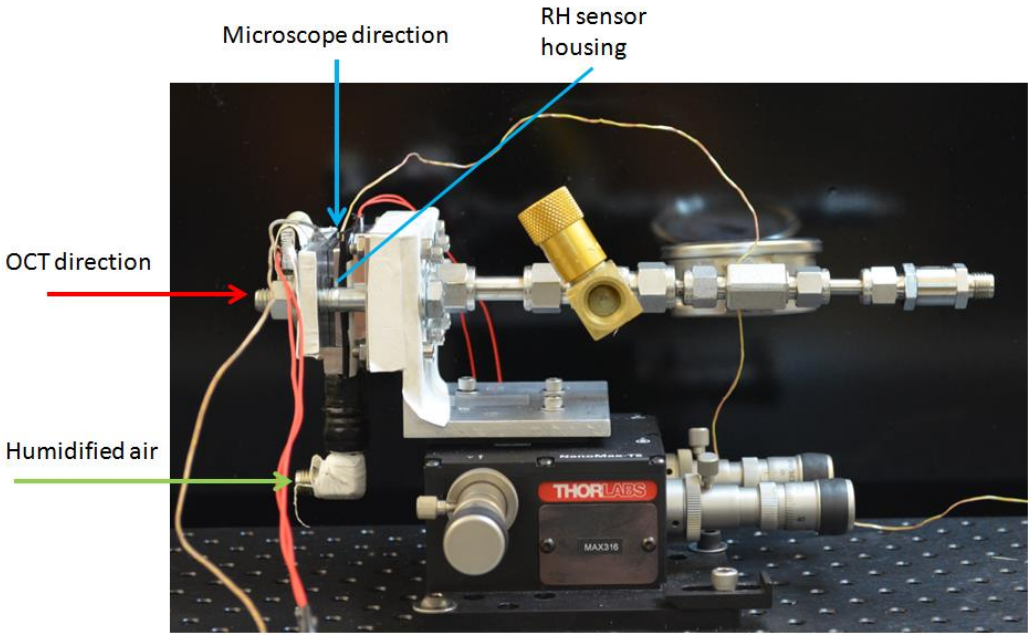

Figure 3-7. Side view of pressure control device

3.2.2 In Situ Test Cell

As mentioned earlier, the in-situ cell was designed in order to be able to operate as a standard PEM fuel cell. Some alterations were necessary in order to allow for an optical window and recesses were machined in the graphite plates in order to provide space for sensors. The cell was designed in order to minimize any impact these alterations would have on cell performance. Figure 3-8 below shows a Solid Works model of the graphite flow field plate of the in-situ cell. The flow field plate was machined with a serpentine configuration from a 0.2 inch thick graphite plate. The flow channels were machined with a 0.125 inch width and 0.04 inch depth (approximately 3 X 1 mm). A recess for the combined humidity and temperature sensors can be found on both sides of the graphite plate. Two pockets for gaskets were also machined in the plate. The first gasket (inner gasket) is for ensuring the gasses pumped to the system stay within the limits of the flow field. The second gasket (outer gasket) is to prevent leakage incoming from the recess for the humidity and temperature sensors (as seen in Figure 3-8).

An optical window was machined at the center of the flow field plate in order to allow for the OCT laser to reach the membrane. This optical window can be found at the center of the graphite flow field plate as seen in Figure 3-8.

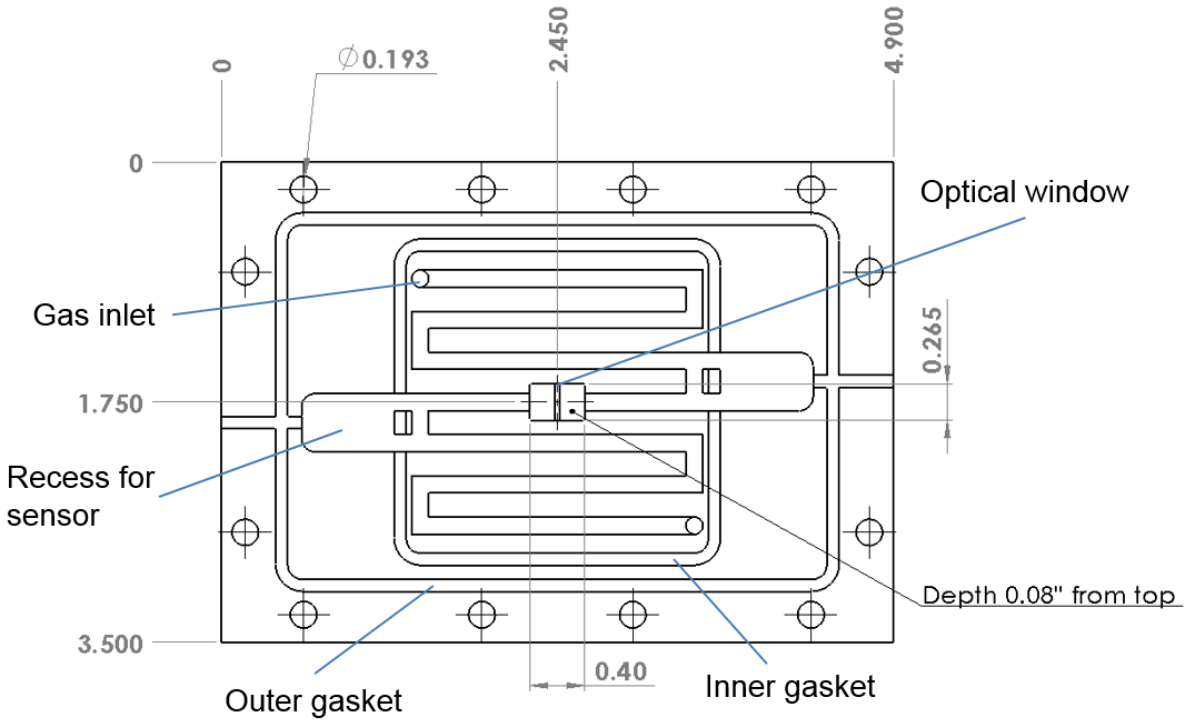

Figure 3-8. Drawing of cathode flow field plate

The optical window was machined with a height of 0.245 inches and a width of 0.08 inches with its thickness going through the graphite plate. A recess was machined around the optical window in order to fit a small chip. This chip consists of two pieces of graphite and one piece of polycarbonate, as seen on Figure 3-9. This chip was placed in the cell to decrease the width of lands and channels being imaged to about 0.5 mm, which more closely represent flow field plates found on running cells. This chip must also allow transparency in order for the OCT laser beam to be able to reach the membrane. The chip could potentially be built entirely out of polycarbonate however, polycarbonate does not conduct electricity the same way graphite does. Therefore the chip was constructed of two parts of graphite and one part of polycarbonate. As the polycarbonate section is considered electrically inactive its width was kept to a minimum. For the procedure carried out in finding the minimum allowed thickness of the polycarbonate section of the chip, please refer to section 3.2.3.

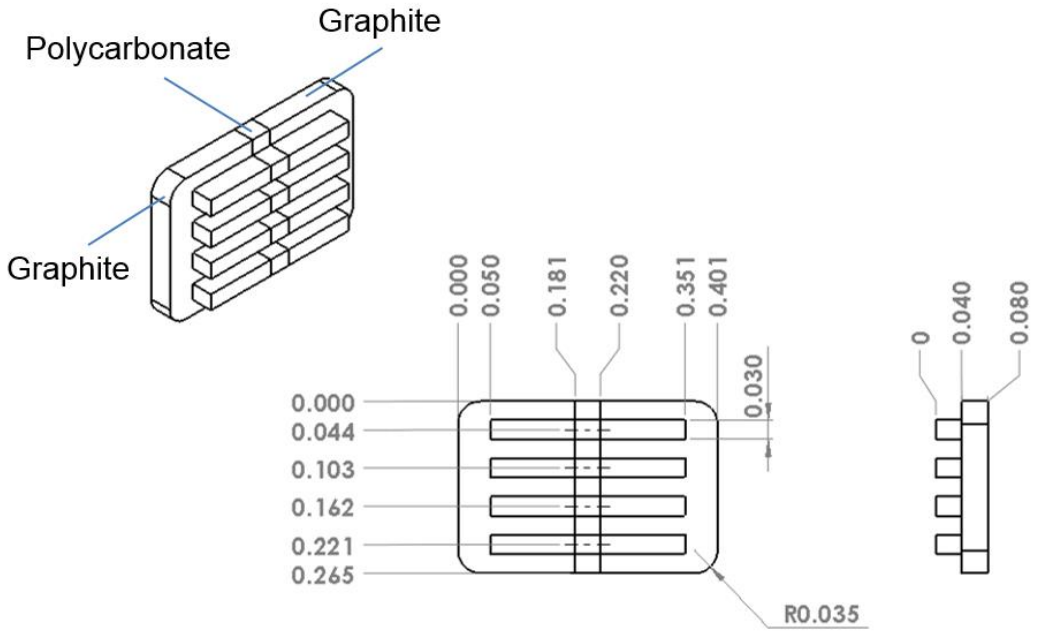

Figure 3-9. Drawing of the channel chip

Two small recesses can also be found on the right and left sides of the graphite flow field plate (refer to Figure 3-8) in order to fit the combined humidity and temperature sensors (SHT75, Sensirion). This setup is similar to those used by Hinds et al. [57]. A close up of the sensors installed near the flow channels of the graphite plates can be found om Figure 3-10 below.

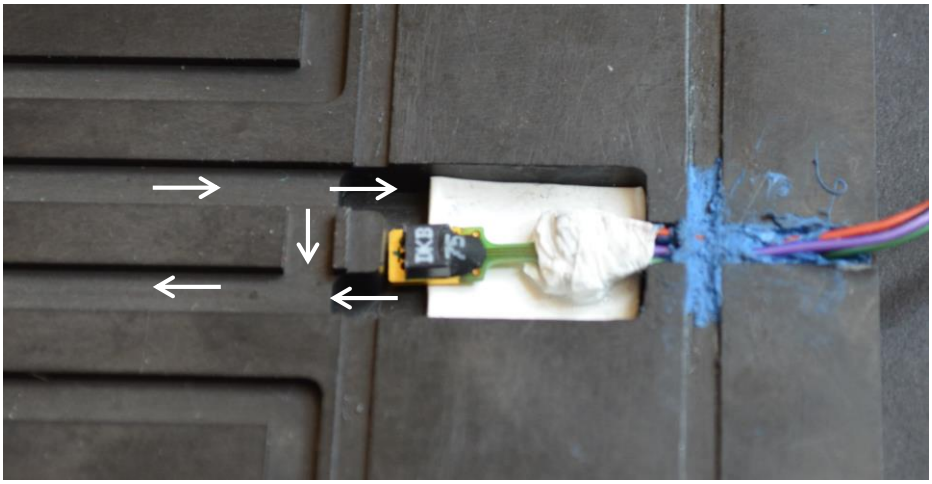

Figure 3-10. Humidity and temperature sensors embedded in cell recess. White arrows demonstrate direction of pumped inlet gases

Care was taken to ensure the sensors received enough humidified air incoming from the test station. The groove machined for the wires of the combined humidity and temperature sensors was sealed using the same material used for the gaskets. The sealing of this groove is important for the accuracy of readings of the temperature and humidity sensors. Leaks in this groove could potentially allow for outside air to leak into the sensor recess which could impact the humidity readings.

PEM fuel cells produce water and heat as by-products of the electrochemical reactions that take place during operation. As mentioned earlier, fuel cells typically operate between 80 and 90 °C. The quasi in-situ test cell however, works with humidified nitrogen and no electrochemical reactions take place in the cell. In order to keep the cell up to representative temperatures heating plates were installed at the sides of the graphite plates, as shown in Figure 3-11 below.

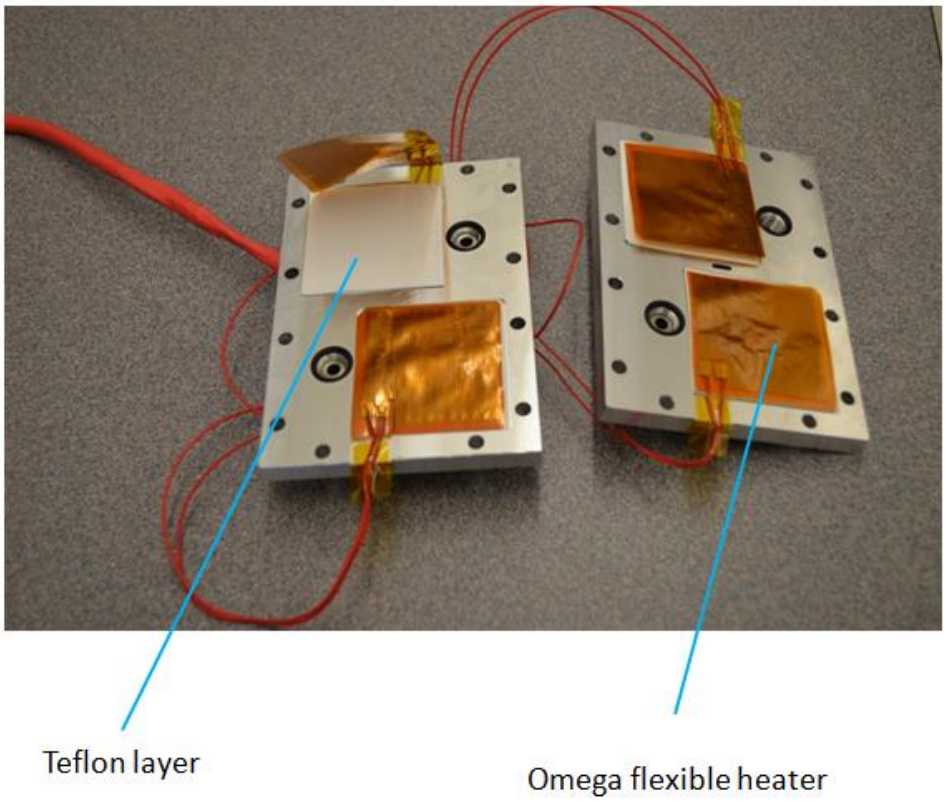

Figure 3-11. Outer plates with heaters of heating plate assembly

The heating assembly was constructed out of two aluminium plates for each side of the cell (anode and cathode). A 3/8'' thick aluminium plate was used as the outer plate of the assembly, as seen in Figure 3-11.

These plates were machined to allow for a recess for the flexible heaters (KH – 202/10, Kapton). A thinner 1/8" thick aluminium plate sandwiches the haters. The thinner plates are directly in contact with the graphite flow field plates, while the thicker plates face the outside of the cell. A double layer of Teflon was placed beside the heaters to provide good contact between heaters and heating plates. Clearance holes were machines in order to allow the incoming gases from the test station to reach the graphite flow field plates. O-rings were fitted around the clearance holes in both thicker and thinner plates in order to avoid any leaks. The heating plate assembly can be seen in Figure 3-12 below.

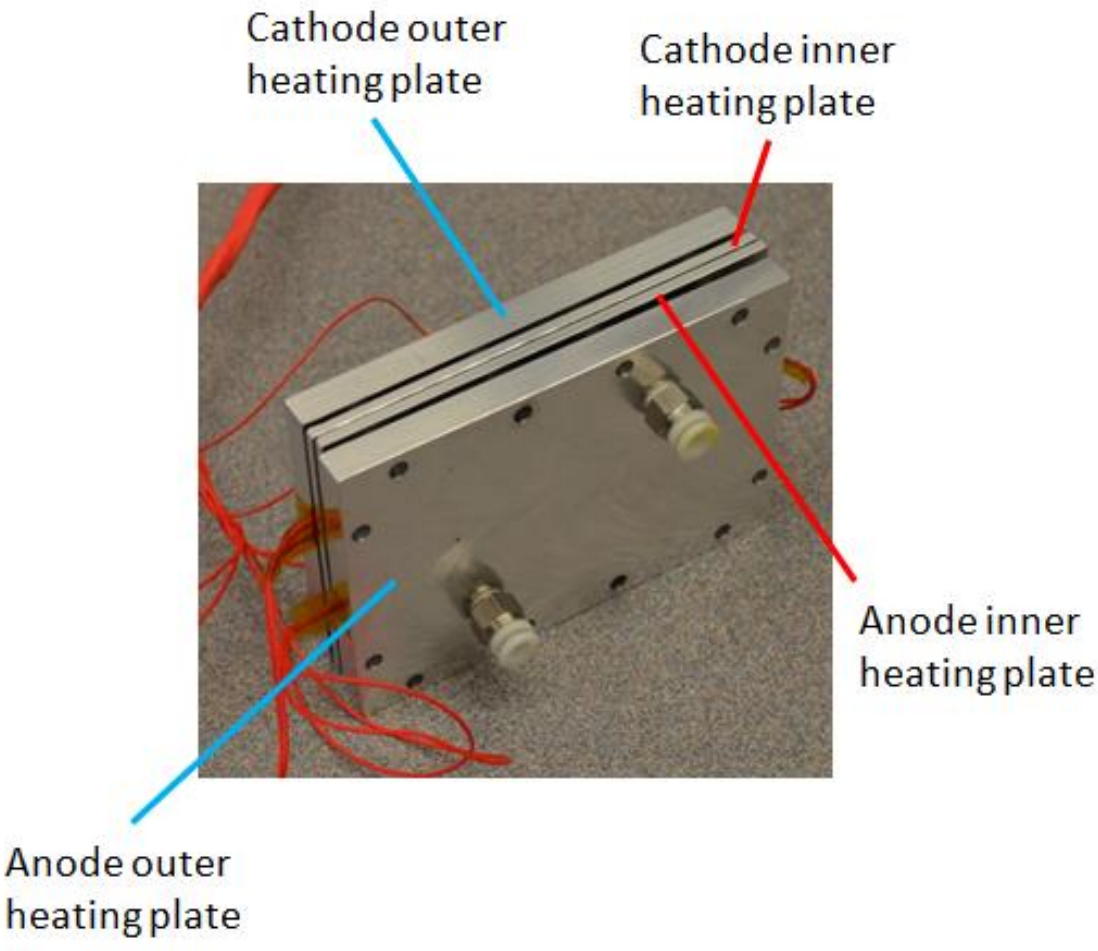

Figure 3-12. The heating plate assembly

The anode and cathode side of the heating assembly are almost identical. They only differ in that the cathode side features a small slot to allow for the OCT laser beam to reach the membrane. Figure 3-13 below shows an exploded view of a Solid Works model of the in situ test cell with all of its components.

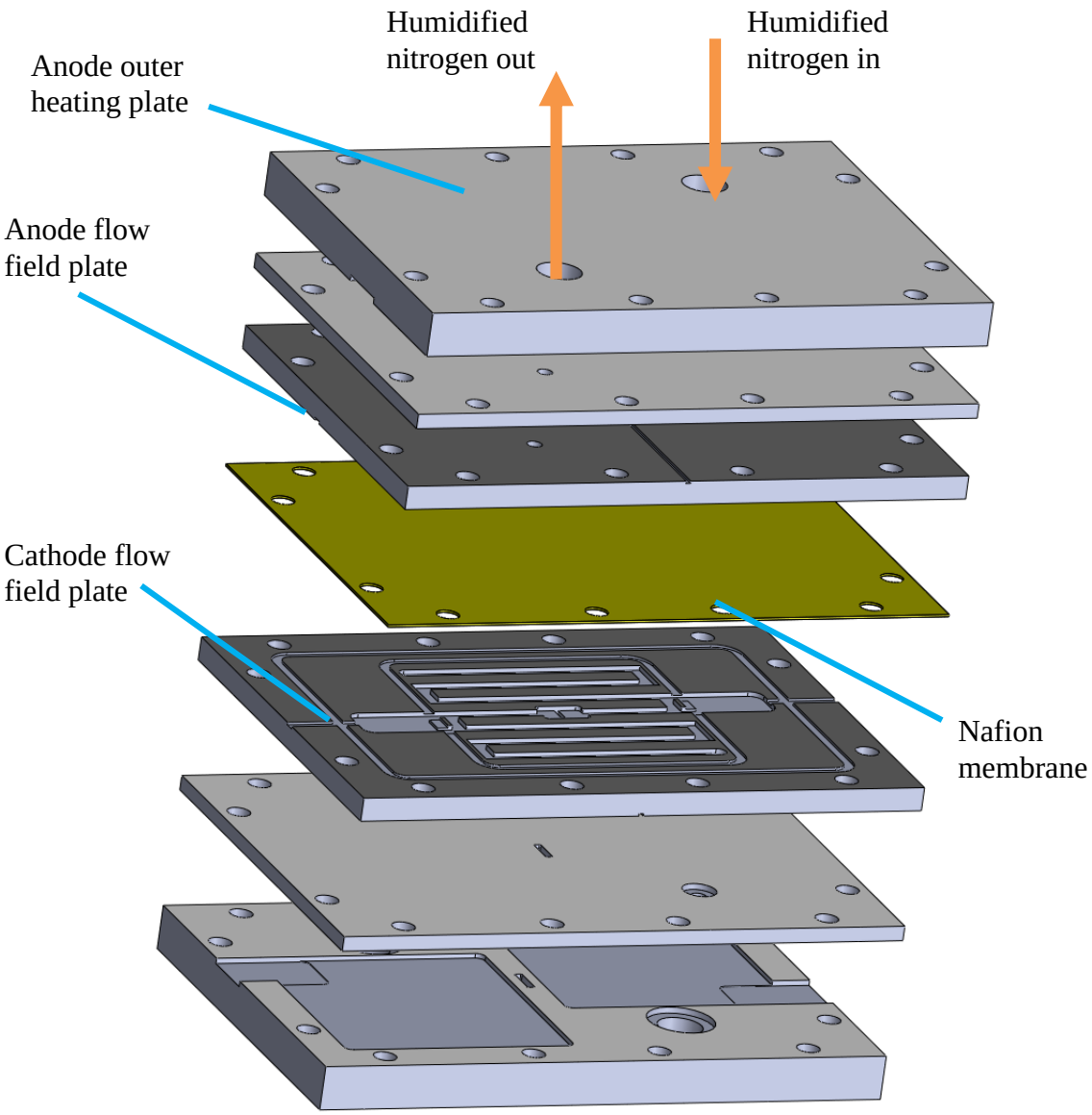

Figure 3-13. Exploded view of quasi in-situ test cell

It is important to point out that the Nafion membrane displayed on Figure 3-13is a bare membrane with no GDL or GDE attached to it. All tests carried out with the situ test cell were conducted with GDE material.

3.2.3 Channel Chip

As it was mentioned on the previous section, the channel chip was constructed out of two parts of graphite and one part of polycarbonate in the middle. As polycarbonate is electrically inactive, it was necessary to keep its thickness to a minimum in order to keep the test apparatus representative of an actual fuel cell system.

The OCT system used in this project was built using a laser that follows a Gaussian profile. The radius of a Gaussian beam increases with stand of distance as described by Equation 4.2 below [53].

$$w(z) = w_0\sqrt{1 + (\frac{z}{z_R})^2} \tag{3.1}$$

Where w (z) is the radius of the beam spot, w_0 is the radius at the focal point, Z is the stand of distance from the focal point and Z_r is the Rayleigh range defined by: $z_R = \frac{\pi w_0^2}{\lambda}$ [53]. Figure 3-14 below shows beam radius as a function of the stand off distance. For the system used in the experiments carried out in this project, the beam spot size is 11.7 μm at the focal point which is located at a distance of 50 mm from the objective lens. The focal point should be adjusted to be located at the Nafion membrane, in order to optimize the system. As the stand of distance from the focal point increases, the beam spot size increases as well. It is therefore important to design the channel chip accordingly to ensure the polycarbonate section is wide enough to allow the whole of them beam through.

While calculating the minimum thickness for the polycarbonate section, all parameters were taken in the worst possible case scenario. This would lead to an overestimation of the minimum polycarbonate thickness. However, due to the difficulty of changing the thickness of the polycarbonate once it had already been manufactured it was decided that it was preferential to overestimate the minimum thickness other than underestimate it.

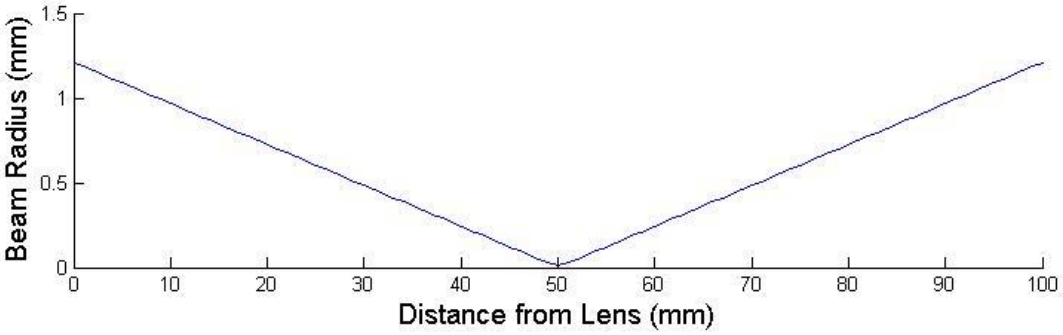

Figure 3-14. Profile of OCT laser beam

The focal point was considered to be located at the center of the Nafion/ PDMS membrane. The membrane thickness was taken at 200 µm for the calculations, the GDE used in the experiments had a thickness of approximately 200 µm and the chip had a height of approximately 2 mm. As seen in Figure 3-15 below, when the OCT laser is focused at the centre of the membrane, the focal point is located at a distance of approximately 2.3 mm from the top of the chip.

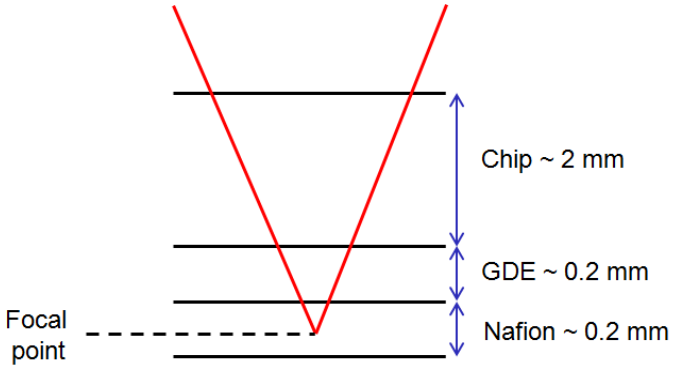

Figure 3-15. OCT Laser focused at centre of membrane

At the top of the chip, the beam diameter is approximately 0.4 mm (as seen in Figure 3-14 above). Therefore a chip with a polycarbonate section 0.4 mm wide should suffice. However due to recommendations of OCT system operators, the transparent media should be taken to be at least twice the width of the laser spot size in order to avoid reflectance with the graphite walls and to allow for ease of alignment. It was then specified that the polycarbonate section should have a thickness of at least 0.8 – 1 mm. A smaller thickness

could potentially be considered with the risk of reflections affecting the quality of the image.

3.3 Membrane Preparation

This section covers the procedure carried out for the preparation of the membranes used in this project. Two types of membrane were prepared: Nafion-TiO_2 membrane with different contrast agent concentration and PDMS (Polydimethylsiloxane)-TiO_2 phantoms. Phantoms can be considered to be samples manufactured to closely mimic the optical and motion properties of the material to be studied. The PDMS-TiO_2 membranes were first used in this experiment as a means of validation of the OCT elastography technique in the compression tests carried out in the ex-situ test cell. PDMS was selected as the material of choice as it is non-toxic, relatively cheap and for its ease of controlling membrane thickness. Once the validation experiments were carried out with the PDMS-TiO_2 phantoms, experiments with the more expensive and more complex to prepare Nafion-TiO_2 membranes were carried out. The following is a detailed description of how the two types of membrane were prepared. Even though both use the same contrast agent, the manufacturing procedure differs between PDMS and Nafion membranes as described below. The TiO_2 powder used for fabrication of membranes was TiO2 particles 99% by Spectrum Chemical Manufacturing Corp. For specifications on the TiO_2 powder, please refer to Spectrum Chemical Manufacturing web site [58].

3.3.1 PDMS-TiO_2 Phantoms

PDMS-TiO_2 membranes were fabricated using the spin coating technique. This technique allows for simple and easy control of membrane thickness and ensures uniformity. Spin coating works by pouring a coating liquid material at the center of a substrate disc. The substrate was spun at high speed forcing the material to spread over the area of the substrate due to centrifugal force, as seen in Figure 3-16 below [41]. The rotation continued until the desired thickness was achieved. The thickness of the membrane was controlled by controlling both spin time and spin velocity [41]. Both spin velocity and

spin time are inversely proportional to film thickness. Typically films formed on the surface of the substrate tends to have a uniform thickness.

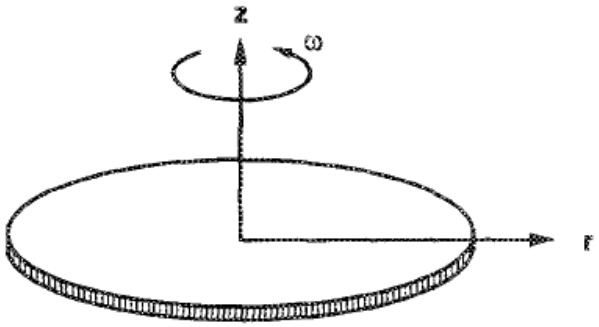

Figure 3-16. Example of substrate in spin coating process [41].

The material used in this project was Sylgard® 184 Silicones Elastomer Kit by Dow Corning. More information Sylgard 184 elastomer can be found online at the Dow Corning web page [59]. The procedure for preparing PDMS membranes is followed as recommended by Dow Corning. However some steps are added in order to add the contrast agent. The mix was subsequently spun coated in order to from a uniform film. Figure 3-17 below shows the preparation scheme of PDMS-TiO_2 membranes.

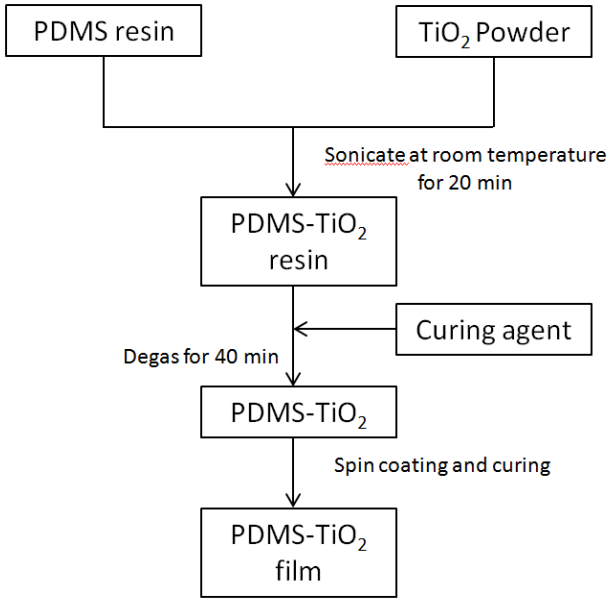

Figure 3-17. Preparation scheme of PDMS-TiO_2 membranes.

Firstly PDMS resin was mixed and stirred with TiO_2 powder until all material is dissolved. Different concentrations of TiO_2 powder were used in order to achieve different levels of membrane transparency. The mixture was further sonicated at room temperature for 40 minutes to ensure for a homogeinity and avoid the formation of lumps of TiO_2 powder. After sonication, the curing agent was mixed with the resin. The ratio of resin to curing agent used was 10:1, as recommended by Dow Corning. The mixture was then degassed in a vacuum chamber for 40 minutes to eliminate air bubbles. The degassed mixture was subsequently poured into a substrate for spin coating. The membranes in this project were spun coated for 30 secons at 500 and 700 RPM. After the spin coating process was finished the material was cured on a hot plate at 80 °C for 4 hours. Once the curing process was completed, the material was cut to size. The membranes had their thicknesses subsequently measured using a micrometer. Measurements were made using a Mitutoyo Digimatic Micrometer, with an accuracy of ± 2 μm, eight measurements were made for each membrane and the averaged results were used.

3.3.2 Nafion-TiO_2 Membranes

Nafion-TiO_2 composite membranes used in the experiments of this project were prepared at Simon Fraser University with the aid of Dr. Steven Holdcroft's group, in the Deparment of Chemistry. The procedure carried out was similar to what is readily available in the literature [11, 24]. Special care was taken while mixing the contrast agent with the Nafion solution to ensure for homogeneity.

The membranes were prepared from a 20% wt Nafion dispersion in propane/water. The solution used was D2020 by DuPont. Membrane were fabricated with different titanium dioxide concentrations: 0, 0.1, 0.2, 0.5 and 1 %wt. The titanium dioxide powder used for fabrication of Nafion-TiO_2 membranes was the same as used in the fabrication of PDMS-TiO_2 membranes (refer to section 3.3.1). Figure 3-18 below shows the preparation scheme of the Nafion-TiO_2 membranes.

Firstly the D2020 solution was mixed with the TiO_2 powder. The mix was stirred for 15 minutes, following further 15 minutes of sonication. This process was carried out twice to ensure good dispersion of TiO_2 particles. The solution was further poured to a glass plate.

A 1 mm thin layer was formed with using a K202 Control Coater casting table and a doctor blade from RK PrintCoat Instruments Ltd as seen in Figure 3-19.

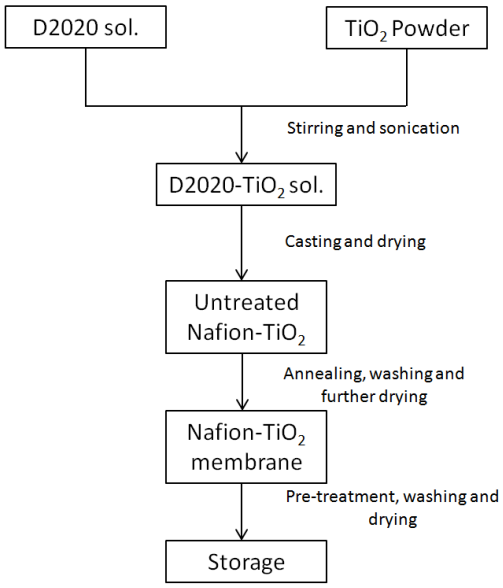

Figure 3-18. Preparation scheme of Nafion-TiO_2 membranes

The membrane was left to dry overnight at room temperature, further annealed at 120 °C for eight hours and dried at 100 °C in vacuum for 24 hours in order to remove solvents.

Figure 3-19. D2020-TiO_2 solution on glass plate (left) and 1 mm film after casting (right)

Once the drying process was complete, the membranes were be peeled off the glass plate. The membrane was moistened with deionized water prior to peeling in order to soften the material and avoid tearing or cracking. Prior to storage, the membranes went through a pre-treatment process in order to remove contaminants, similarly to the procedure carried out on references [11, 24].

The membranes were pre-treated at a solution of hydrogen peroxide (3% wt) at 80 °C for 1 hour in order to oxidize any organic impurities and a further hour in a 1 M solution of H_2SO_4 in order to remove ionic impurities. All membranes were then washed multiple times in deionized water in order to remove any excess acid. The membranes were then dried in vacuum for 12 hours at 80 °C and stored. The Membranes had their thickness measure with a micrometer (refer to section 3.3.1) at the centre and edges, four measurements were made for each and the results averaged.

3.3.3 Nafion-TiO_2 MEAs

Nafion-TiO_2 membranes were hot pressed with GDE material to create MEAs (membrane electrode assemblies). The GDE material was provided by Ballard Power systems, in order to closely represent the MEA of a fully operational fuel cell. The GDE specifications were not provided.

The GDE material was firstly cut to dimension. A rectangular slit was then laser cut in the centre of the GDE to allow for the passage of the OCT laser beam. The slit was 5 mm in length and heights of 50, 100, 150 and 200 μm were used. The Nafion TiO_2 membrane was then sandwiched by the two GDE layers, one with a slit and one without it. The Membrane and GDE layers were then hot pressed together. Hot pressing was carried out at a pressure of 15 bar and a temperature of 150 °C for 150 seconds, as recommended by Ballard Power systems.

3.4 Method Validation

As mentioned in previous chapters, this project makes use of DIC (digital image correlation) in order to estimate thickness change, displacement maps and strain distribution on Nafion-TiO_2 membranes. This process is carried out by analyzing changes

in images of the membrane acquired by an optical coherence tomography (OCT) system and microscope acquired images. It was mentioned in section 2.5.2 how the subset size may impact the displacement calculations. Section 2.5.3 mentioned the need for a contrast agent in order for the DIC technique to be carried out. The need for image filtering and noise reduction was overviewed in section 2.7. To the knowledge of the author, DIC has not been carried out on Nafion membranes to date. Therefore it is important to first validate the technique and estimate its accuracy before more detailed experiments can be carried out. This section outlines the processes and steps carried out for interpretation, validation and the effect of different parameters in DIC. The results of the validation experiments along with a discussion of the findings can be found on Chapter 4:. The steps carried out for the validation of the experiment were conducted as follows:

A. Interpretation of OCT scans and optical path length (OPL) correction
B. Study opacity of membranes with contrast agent concentration.
C. Effect of spatial diversity filtering on OCT scans.
D. Evaluate the impact of subset size on relative displacement calculations
E. Smoothing of vector fields and contour plots
F. Quantitative analysis of effect of contrast agent on membrane swelling

3.4.1 Scan Interpretation and OPL Correction

OCT scans undergo optical shifting due to optical path length difference in parts of the scan. Section 4-1 shows example scans of Nafrion-TiO_2 membranes sandwiched by the polycarbonate flow field plates. The geometry of the flow field plates, as shown in figure 4-1, leads to a difference in optical path length between land and channel. This OPL difference leads in an apparent shift in the channel section of the membrane in comparison to the land section of the membrane. The interpretation of the scans is showed in section 4.1, along with example images of OPL corrected scans.

3.4.2 Membrane Opacity

It was mentioned in Chapter 2 how a contrast agent was necessary in order to create a speckled pattern in the membrane. However, lower concentrations of contrast agent might lead to speckles that are not visible, and too high a concentration might lead to membrane opacity. In case the membrane has a high degree of opacity, the laser signal may be absorb by the material as it travels through its thickness. This may lead to the membrane only being imaged partially, leading to loss of information. The membranes fabricated in this project can be found on section 4.2 along with images showing OCT scans for a variety of different contrast agent concentrations.

3.4.3 Spatial Diversity Filtering

The spatial diversity technique was used in this project in order to remove unusable speckled noise from the OCT scans. Section 4.3 shows example scans of OCT membranes prior to spatial diversity filtering. The intensities of the image were thresholded in order to show the variance of intensities from the background. Images post filtering underwent thresholding in order to evaluate any significant decrease in background randomness.

The stationary spatial diversity technique was used for filtering out unusable speckled noise in the OCT scans. Fifty scans of the same location were acquired for each OCT scan while scanning the membranes. The filtering was carried out simply by averaging the intensity of all fifty images. Image intensity threshold was carried out prior and post spatial diversity filtering to analyse its effects.

3.4.4 Subset Size Impact on Displacement

As mentioned earlier on section 2.5.2, the appropriate selection of subset size is of vital importance for accuracy of displacement calculations. The impact of subset size on the estimation of membrane thickness change is studied on section 5.4. Thickness change is calculated using DIC for a number of different subset sizes and the results are compared to a reference measurement. Once DIC results from the various subset sizes are compared to measured results, the appropriate subset size for subsequent experiments can be found.

3.4.5 Smoothing impact on Displacement

Smoothing is a commonly used technique in DIC for noise reduction [47, 51]. Smoothing is carried out by averaging displacements in the vicinity of control points in order to reduce some of the noise inherent from DIC. Even though results gone through smoothing look significantly more homogeneous and easier to interpret, this process could potentially lead to an alteration of the calculated results. In order to verify if smoothing impacts the calculated results, thickness change is calculated using DIC and the results for different levels of smoothing are compared. The results can be found on section 4.5.

3.4.6 Contrast Agent Concentration Impact on Displacement

Titanium dioxide powder was used as a contrast agent in Nafion membranes in order to generate a speckled pattern to be tracked by a computer algorithm in order for membrane swelling and thickness change to be calculated. Previous studies have shown how the use of said contrast agent may alter the membranes mechanical properties [11, 24] (refer to section 2-6) . Therefore an analysis is carried out in an attempt quantify the impact of the use of TiO_2 powder on Nafion membranes. The results for these experiments are displayed in section 4.6.

3.5 Experimental Procedure

Once the technique has been validated and the appropriate parameters to be used in DIC have been found, experiments quantifying thickness change in Nafion-TiO_2 membranes and displacement maps can be carried out. This section details the procedure followed for the tests carried out in this project. This section first details the setup and procedure of the compression tests carried out with the ex-situ cell. Section 3.5.2 details the procedure for the humidification tests carried out in the ex-situ cell. Section 3.5.3 explains the setup and steps followed for tests carried out with the in-situ cell.

Section 3.5.4 details the process carried out for measuring the membrane thickness change using the microscope images, while section 3.5.5 details the steps taken to measure thickness change and obtain strain maps using speckle tracking

3.5.1 Ex Situ test cell – Compression

The compression tests were carried out using PDMS-TiO_2 membranes only. No GDL was used in these tests as their goal was only to compare the results from microscope images and OCT scans. Ideally the OCT scans and microscope images would be acquired simultaneously however, do to time constraints and limited space in the facilities where the OCT scans were acquired, these tests were carried out separately. Care was taken to ensure repeatable results.

The ex situ cell was firstly bolted to a heavy steel plate to minimize vibration and movement. A PDMS-TiO_2 membrane was placed in the cell, being sandwiched by the carbon flow field plates. The cell was pressurized to 30 psi, which was taken as the starting point. Scans of the membrane were taken with the OCT system (refer to Figure 3-6) and images taken with the microscope. A light source was used to illuminate the membrane for clarity of the membrane images. The pressure was then slowly increased by turning the knob in the nitrogen tank regulator. The pressure was increased in steps of 1 psi. OCT scans and microscope images were taken for each pressure step. The membrane was pressurized up to a pressure of 85 psi.

3.5.2 Ex Situ test cell – Humidification

The humidification tests in the ex-situ cell were carried out in a similar fashion to the compression tests. The difference is in that for the humidification tests the cell was at a constant pressure of 100 psi. The ex situ cell was loaded with bare Nafion-TiO_2 membranes and Nafion-TiO_2 MEAs (refer to section 3.3.3). The cell was humidified with the aid of a Fuel-Cell test station system 850 e multirange by Screibner Associates Incorporated on loan from NRCC. The fuel cell test system pumped humidified air into the ex-situ test cell as seen in Figure 3-7above. The outlet humidity was be controlled by controlling the temperate of the water bubblers inside the fuel cell test system. Microscope images of the membrane and OCT scans were taken for incremental steps of 1% RH at a constant temperature of 60 °C and 80 °C. A humidity of 30% was taken as the baseline for the starting point of the tests. The maximum humidity was of 85 %.

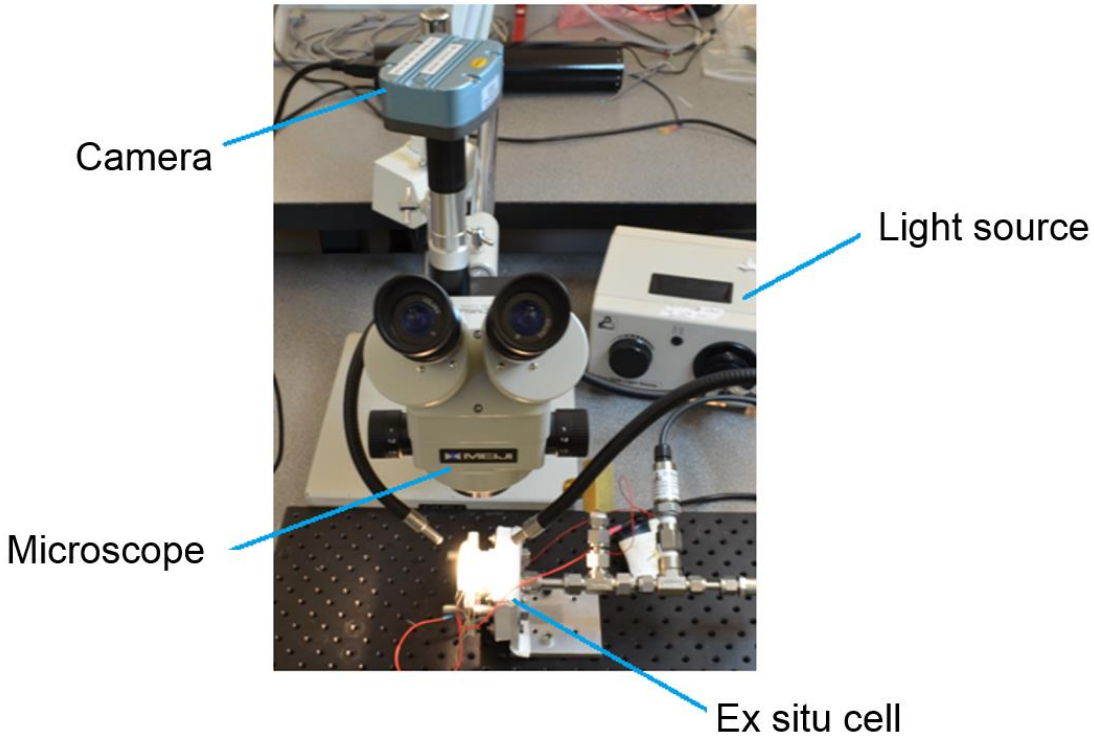

Figure 3-20. Ex-situ cell being imaged by microscope

3.5.3 In Situ Cell – Humidification

The tests carried out in the in-situ cell were conducted with a Nafion-TiO_2 MEA. The GDE material for fabrication of the MEAs was supplied by Ballard Power Systems. Figure 3-21 below shows the setup of the test. The test specimen used was a Nafion-TiO_2 MEA made of a membrane with a contrast agent concentration of 0.2 % wt. The MEA slit was aligned with the channel chip inside the cathode plate and the cell was assembled with the heating plates. The quasi in-situ test cell assembly was attached to a three axis stage for ease of alignment with the OCT system. The side of the test cell containing the imaging slot was taken as the cathode side. The cathode side is placed facing the OCT laser, while the anode is placed facing away from the OCT laser as seen in Figure 3-21.

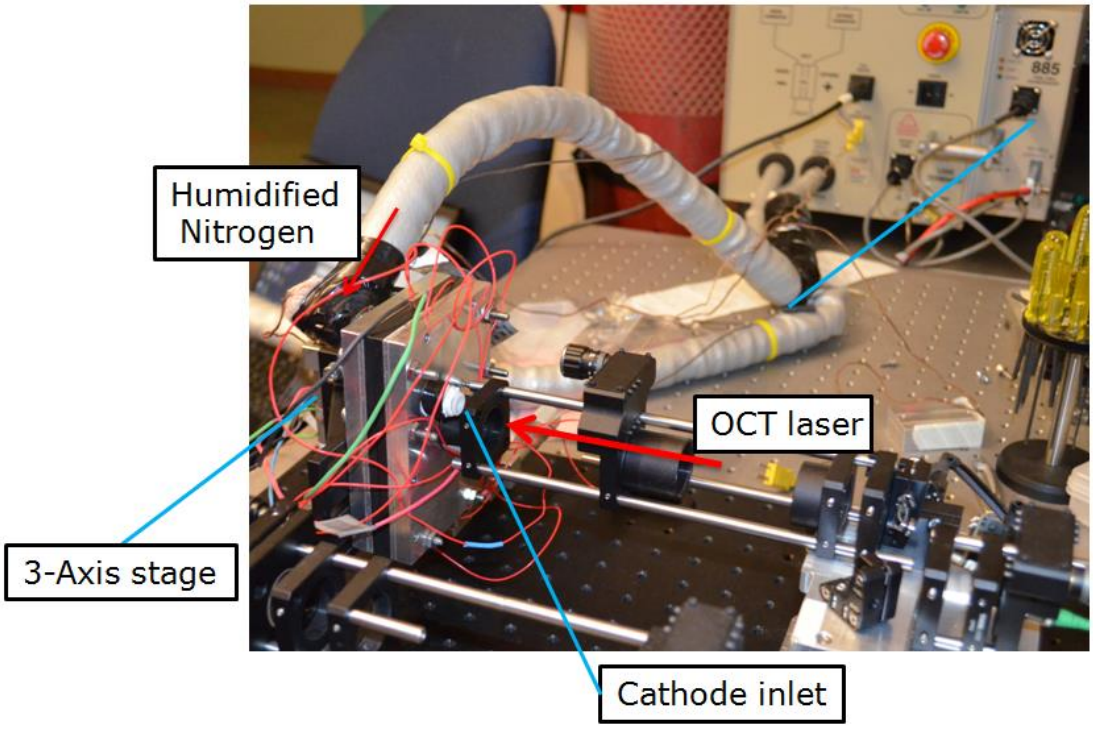

Figure 3-21. Test setup of quasi in-situ cell

Hoses coming from the test station supplying humidified nitrogen were attached to the cell through NPT push to connect tube fittings. Originally the cell was designed to receive humidified Nitrogen from both anode and cathode. However, at the time of the imaging session (March 11th – 12th 2014) the OCT system was setup in such a way that in order for the cathode hose to be connected to the test cell, it would have to block the optical path length of the OCT laser. Time constraints also played an important role in the experiments that were able to be carried out. The experiment with the in-situ test cell was carried out with only a hose connected to the anode side. The humidity was increased in steps of 1-2 % by moisturizing the incoming gas stream. The humidity range was 30 to 80 % while the temperature of the cell was kept constant throughout the experiment at 70 °C. Once the humidity reading of the combined temperature and humidity sensors stabilized, the system was left idle for approximately 1.5 min and only then an OCT scan was recorded. The process was repeated until the relative humidity value of 80% was achieved. The cell was clamped at a pressure of approximately 4 bar, which is similar to values found in the literature [60].

3.5.4 Microscope Thickness Change Measurements and DIC

Image processing and analysis software ImageJ was used to measure thickness change images acquired by the microscope mounted camera. Thickness change results from OCT and microscope images were further compared. The measurements done on the microscope images were carried out measuring the membrane thickness in each successive image. Figure 3-22 below shows one of the microscope images with a magnification factor of 5.

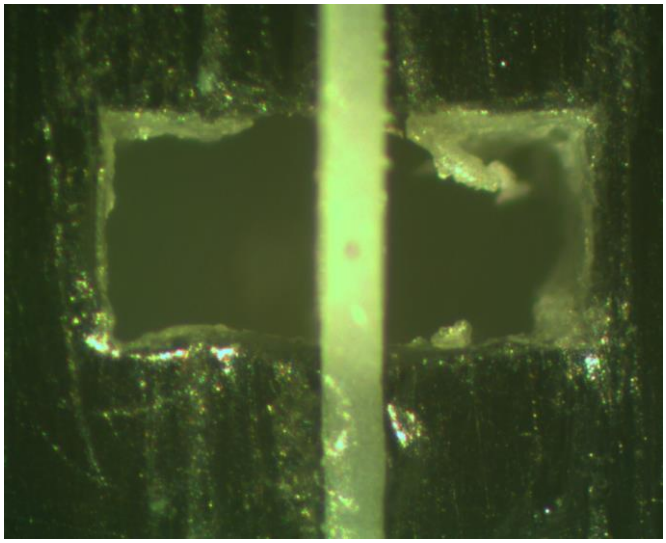

Figure 3-22. Example of image acquired through microscope

The membrane is displayed in white in the middle of Figure 3-22, while the two polycarbonate flow channel are on the sides. First the image was loaded to ImageJ. The option “binary” was selected, converting the colour of pixels in the image to either a white or black. This option highlights the borders of the membrane sitting in the middle of the polycarbonate plates, as shown in Figure 3-23 below. The option “find edges” was subsequently used to highlight the edge of the binary membrane image. The width of the membrane was then measured by drawing a horizontal line, perpendicular to the edges of the membrane. The two extremities of the horizontal line touch the edges of the membrane. ImageJ allows for counting the number of pixels that make the drawn line by selecting: Analyze, Measure. Strain was calculated as shown in Equation 3.2 below:

$$\varepsilon = \frac{L_1 - L_2}{L1} \quad (3.2)$$

Where L_1 is the length of the membrane in the reference image and L_2 is the length of the membrane in the deformed images. The length of the membrane was measured in 3 different locations for each image. The same location was used in all images for higher accuracy. The strain value in the results section was calculated as an average of the strain found for the three different line locations. These locations were taken as the middle of the land section in order to avoid any potential variation due the proximity with land section.

The uncertainty of the technique was measured to be approximately ± 5% as a number of measurements was carried out for the same location and its variation recorded. For more information on the estimation of uncertainty of the technique, please refer to Appendix A.

As the measurement technique is carried out manually, it is subject to human error. It is likely that variations in the measurements take place depending on the observer. However, to the knowledge of the author, there are currently no other validation techniques available for comparison with DIC.

As the reference measurement technique for comparing DIC of OCT images was also an imaging technique, DIC of microscope images was further carried out for comparison of results. By comparing the DIC results of OCT and microscope images it is possible to analyse how factors such as pixel per micron ratio affect the quality of the results. A comparison of displacement maps for OCT scans and microscope-acquired images can be found on section 5.2.

Figure 3-23. Binary conversion of microscope image

3.5.5 Speckle tracking Thickness Change and Displacement Maps

Speckle tracking was used in the experiments of this project for two purposes: Measuring thickness change for comparison with microscope images and for showing relative displacement maps. Both processes were carried out in the same fashion, but thickness change requires some interpretation of the results.

For thickness change measurements, two or more OCT scans were necessary, one for the reference image and one or more for the deformed images. Figure 3-24 below shows an example with one reference image and one deformed image. All images had same dimensions (in pixels). The centre of the membrane was aligned in the reference and deformed images, as shown in an example on Figure 3-24.

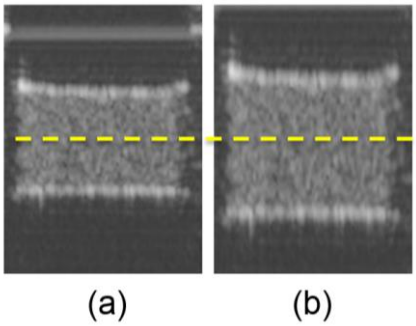

Figure 3-24. Reference (a) and deformed (b) images with membrane centre alignment.

The two images were loaded into the MATLAB algorithm and the correlation parameters were selected. Figure 3-25 shows the contour plot of displacement in the vertical direction of the scans on Figure 3-24.

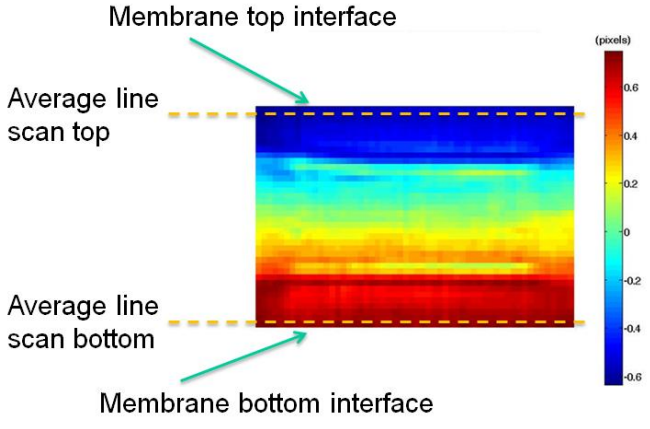

Figure 3-25. Contour map of example deformed membrane

The contour plot shown in Figure 3-25 shows the vertical displacements in a colour map. Each colour represents a magnitude in the vertical direction. By analysing the contour plot, it is possible to observe how much displacement each part of the membrane undergoes.

The center of the membrane was taken as the reference point for displacement and thickness change was interpreted as the difference in the displacement between top and bottom interfaces of the membrane as seen in Figure 3-24. The thickness change is calculated as shown in Equation 3.3 below:

$$\Delta t = -d_t + d_b \tag{3.3}$$

In this equation d_t is the displacement of the averaged line scan at the top end of the membrane and $d_b$is the displacement of the averaged line scan at the bottom end of the membrane in pixels. These lines scans were selected to be at a normalized distance of 0.05 from both interfaces. The absolute values of the displacement of the top and line average scans were added and this value was taken as the membrane thickness change.

As the images from the microscope had different dimensions in pixels, thickness change cannot directly be compared. However, the strain in both images should theoretically be the same. In order to compare strain from elastrography to the values found from the microscope images, thickness change was converted to strain.

$$\varepsilon = \frac{\Delta t}{t_0} \tag{3.4}$$

The symbol ε in Equation 3.4 represents strain, while t_0 is the reference thickness of the membrane at a reference pressure of 30 psi.

When more than two images were correlated, the option of using preceding images as reference image was selected, opposed to always using the first image e.g. if three images were being correlated, image 1 is the reference image for the deformation of image 2 and image 2 is taken as the reference image for the deformation of image 3. This option was used as changes in useful speckled pattern are too great between the full range of images being studied, leading to the code not being able to find correlation results. However, contour plots or vector fields display the cumulative displacement.

By default the code sets a threshold correlation factor of 0.5. As a result when the code finds a correlation factor lower than 0.5 for a specific control point, no result is plotted for that control point on the contour map. The threshold value was raised to 0.7 for this

experiment in order to improve accuracy. The threshold factor was raised in order to avoid noise in the calculated images. This factor was established on a trial and error basis. When threshold values of 0.8 and 0.9 were attempted, poor correlation between reference and deformed imges was observed.

The subset size was selected from a range between 20 and 60 pixels depending on the membrane being studied. The control point spacing was normally 2 pixels, although this value was altered at times for faster calculations. The search zone was set to twice the subset size by default. It was changed to 1.2 times the subset size to prevent erroneous results. This also leads to a much smaller computational effort however, the maximum displacement is limited.

Digital image correlation was further carried out for microscope images. The results DIC results of microscope images and OCT scans was further compared in order to observe potential differences related to subset size accuracy and clarity of results.

Chapter 4: Method Validation Results and Discussion

In this chapter the results from the validation experiments are presented along with a discussion and interpretation. As it was mentioned on section 3.4, these validation experiments are of importance in order to select the correct parameters to be used in DIC, to verify the accuracy of the technique and to evaluate the impact of changing parameters such as smoothing and contrast agent concentration. Firstly the interpretation of the results is shown along with optical path length (OPL) correction for the optical coherence tomography (OCT) scans. The opacity of PDMS-TiO_2 and Nafion-TiO_2 membranes is analysed in section 4.2. Section 4.3 shows the results of OCT scans post spatial diversity filtering. The effect of subset size on the accuracy of the calculated results is analysed on section 4.4. Once the appropriate subset size is found, the effect of smoothing is studied. The results are presented in section 4.5. One the impact of the mentioned parameters is known, the effect of contrast agent concentration is quantified and discussed in section 4.6.

4.1 Interpretation of OCT Scans and Optical Path Length Correction

All OCT scans in this project were acquired while the membranes were sandwiched between two transparent polycarbonate plates or sandwiched between chips with polycarbonate strips. Due to their transparency, polycarbonate plates allow the OCT laser to reach the membrane with minimal signal disruption, while still physically clamping the membrane. However due to the difference in index of refraction between polycarbonate and air, the backscattered laser signal experiences an optical delay in the channel when compared to the land. Figure 4-1 below shows a side view of the polycarbonate flow field plate and its dimensions.

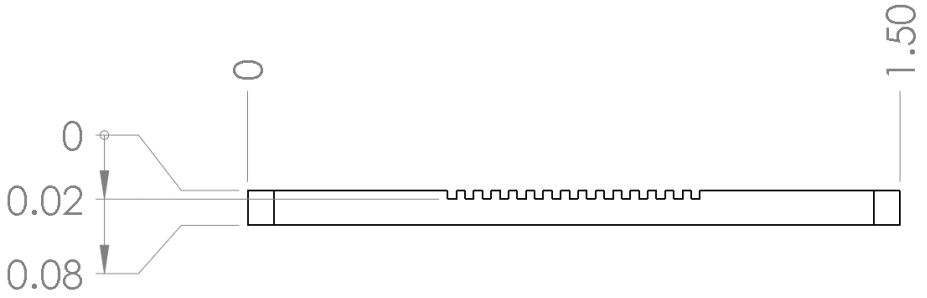

Figure 4-1. Side view of polycarbonate flow field plate

When light travels through the land, it travels through 0.08 inches of polycarbonate which has an index of refraction of approximately 1.58. The optical path length (OPL) is defined as the geometrical distance times the index of refraction of the material. For the polycarbonate lands, this results in an optical path length as described in Equation 5.1.

$$OPL_L = n_P\, d_L = 0.08 * 1.58 = 0.1264 \text{ in} \tag{5.1}$$

OPL_L is the optical path length of the land, n_P is the index of refraction of polycarbonate and d_L is the physical length of the land. When light travels through the channel portion of the polycarbonate flow field plate, it partially travels through air before reaching the membrane. The optical path length of the channel section is described by Equation 5.2.

$$OPL_C = n_P\, d_P + n_a\, d_a = 0.06 * 1.58 + 0.02 * 1 = 0.1148 \text{ in} \tag{5.2}$$

OPL_C is the optical path length of the channel, d_P is the geometrical length of the solid section of the channel made out of polycarbonate, n_a is the refractive index of air and d_a is the geometrical length of the channel. This difference in optical path length between channel and land translates to a time delay between the two signals to reach the photo detector. This time delay is ultimately translated into an apparent shift between land and channel sections of the membrane, as seen in Figure 4-2 below. The green lines in Figure 4-2 were drawn to represent the physical dimensions of the polycarbonate plate, with the blue arrow representing its length in the axial position. The yellow arrow represents the length of the channel. The horizontal white lines seen above and below the membrane in the channel sections represent the interface of the polycarbonate plate. A number of randomly placed horizontal white lines can also be seen in Figure 4-2. These are believed to be reflections backscattered from the polycarbonate plate due to its glossy appearance. These reflections do not affect the speckle tracking algorithm as they fall outside its search zone. For ease of image interpretation, the land section of the membrane can be shifted upwards to correct for the optical path length difference between land and channel. One example of an “OPL corrected” image is shown below on the left side of Figure 4-2.

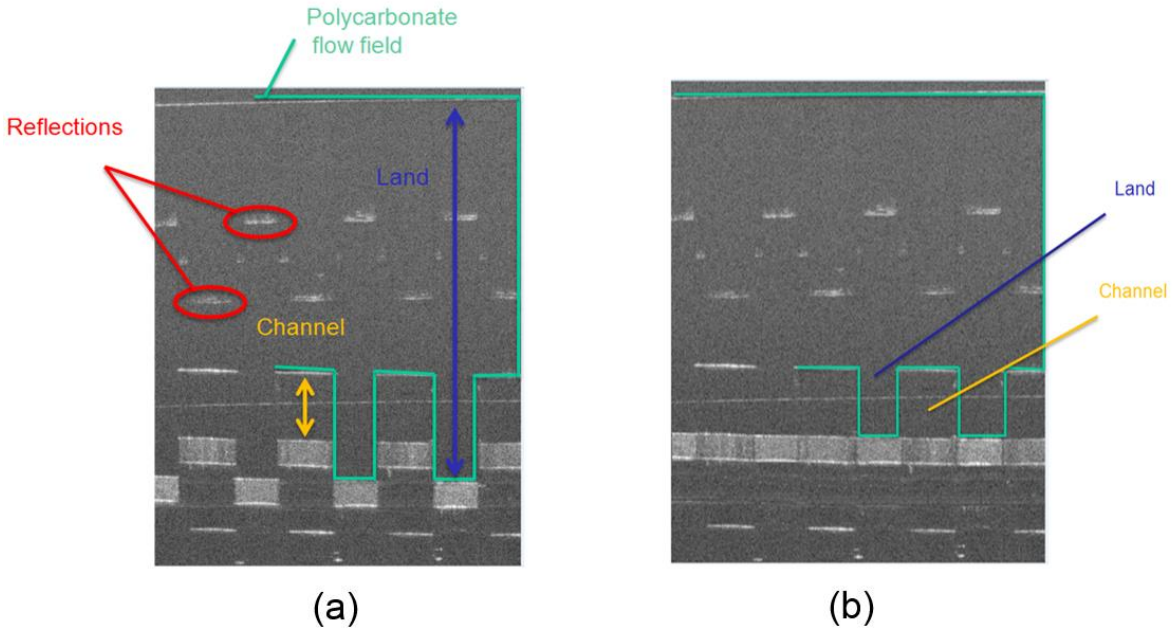

Figure 4-2. OCT Scans through a polycarbonate flow channel plate prior to (a) and post (b) OPL correction

4.2 Membrane Opacity

This section studies the opacity of the PDMS-TiO_2 and Nafion-TiO_2 membranes prepared for this project. As mentioned earlier, different contrast agents were used for both membranes in order to generate a speckled pattern. However, inappropriate concentrations could lead to the membranes not being appropriate for OCT scanning due the high degree of opacity. As the degree of opacity of the membrane depends on both thickness and contrast agent concentration, membranes with different values for both parameters are compared in order to study how suitable they are for OCT imaging. The results of this section show which combinations of thickness and contrast agent can successfully be used for DIC and provide complete through thickness information.

PDMS-TiO_2 membranes were fabricated using 3 different concentrations of TiO_2: 0.1, 0.63 and 1 % wt. Two different spin speeds were used in the fabrication process: 500 and 700 RPM. All membranes were spin coated for 30 seconds. Table 4-1 below shows the membrane thickness found for different concentrations of TiO_2 and spin speed.

Table 4-1. Thickness of PDMS-TiO_2 membranes with spin speed and concentration

Specimen #	Concentration [% wt]	RPM	Thickness [µm]
P1	0.1	700	138
P2	0.63	700	125
P3	1	500	220
P4	1	700	110

Figure 4-3. Difference in transparency of specimens P1, P2 and P4. below shows three membranes side by side each with a different concentration of contrast agent. From left to right these membranes are specimens: P1, P2 and P4 (refer to Table 4-1).

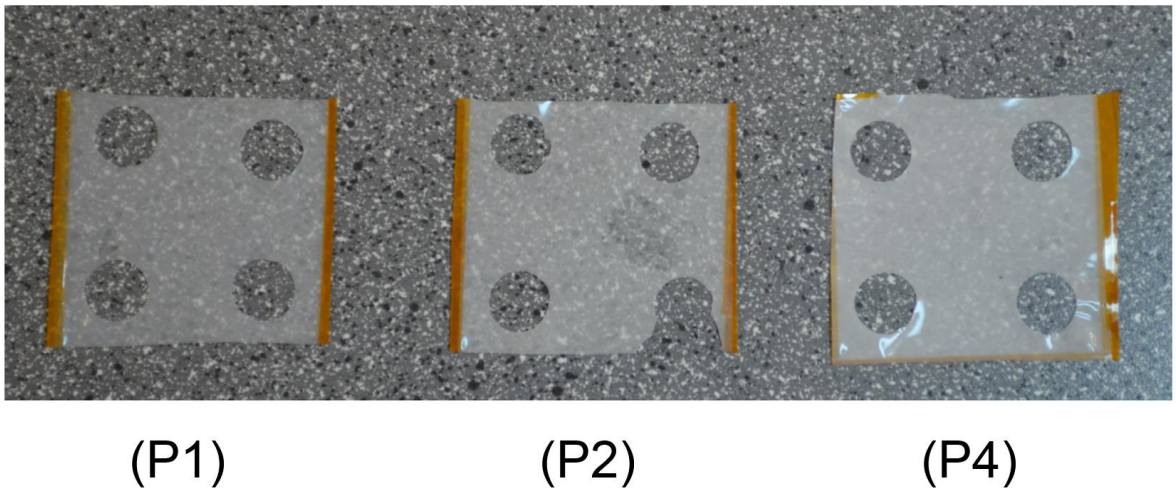

Figure 4-3. Difference in transparency of specimens P1, P2 and P4.

It can be seen that as contrast agent concentration increases so does the opacity of membranes. Specimen P4 looks almost opaque whereas specimen P1 presents a higher degree of transparency. The membranes had OCT scans taken while in the ex-situ test cell to check for transparency. Figure 4-4 below compares OCT scans of specimens P1 and P3.

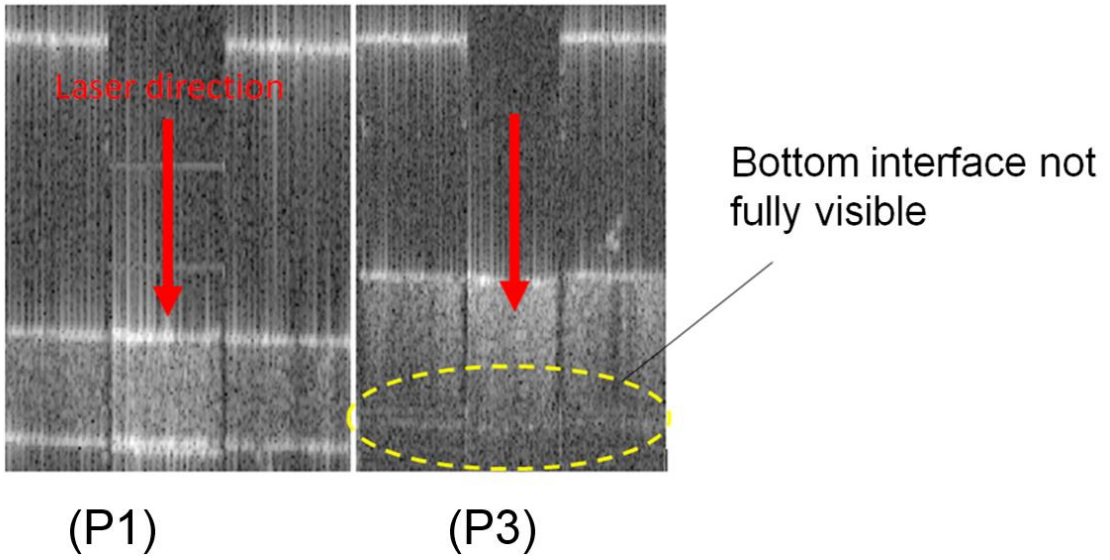

Figure 4-4. Comparison of OCT scans of specimens P1 and P3.

It is possible to see from Figure 4-4 that on specimen P1 both top and bottom interfaces are fully visible. However, in the OCT scan of specimen P3 the bottom interface of the membrane is not fully seen. This is probably due to the increased thickness and opacity of specimen P3 in comparison to specimen P1. Light gets absorbed or scattered as it travels though the membrane. Due to the increased thickness and contrast agent concentration of specimen P3, the signal was not able to penetrate and image the entire depth of the membrane. Furthermore, specimen P1 appeared to have a very well defined speckled pattern, which should suffice for the purposes of speckle tracking. Therefore membranes with lower concentrations of contrast agent were deemed as more appropriate for the purposes of this experiment.

All Nafion-TiO2 membranes were prepared following the procedure detailed on section 3.3.2. Small variations of thickness were measured as contrast agent concentration changed. During the control coating process, the blade was adjusted for a film thickness of approximately 1 mm (prior to drying by evaporation) for all membranes. The difference in concentration of contrast agent could have been responsible for the variation in thicknesses between the membranes. By previous experience, 1 mm thick Nafion dispersion layers were expected to lead to a membrane thickness of around 75 µm for membranes with no contrast agent. Table 4-2. Thickness of Nafion TiO_2 Membranes below summarizes the measured thicknesses.

Table 4-2. Thickness of Nafion TiO_2 Membranes

TiO_2 concentration [%wt]	Thickness edge [µm]	Thickness centre [µm]	Comments
0	70-86	74-75	Wrinkles on edges
0.1	80-102	73-76	Wrinkles on edges
0.2	97-103	76-80	Small wrinkles
0.5	96-120	81-85	Wrinkles on edges
1	86-102	88-90	Small wrinkles

The reason for this apparent difference in thickness between membranes of different concentration levels could be because the contrast agent does not evaporate at the temperatures undergone by the membrane. In other words, when the 1 mm film of Nafion is applied to the casting table, about 80% of the material was constituted of water and alcohols. After evaporation what a much thinner membrane was found. However, as TiO_2 does not evaporate at room temperature, the membrane thickness was expected to increase as the contrast agent concentration increased, as seen in Table 4-2. Furthermore, a variation in thickness can be observed within each membrane. The membranes were measured to be slightly thicker on the edges, while they had an almost homogeneous thickness towards the middle. This was probably due induced by the wrinkles that were found on the edges of the membranes, while the centre was mostly flat.

Similarly to what was seen with PDMS-TiO_2 membranes, higher concentrations lead to less transparency in the Nafion-TiO_2 membranes. Figure 4-5 shows OCT scans acquired for membranes of TiO2 concentrations of 0.2 and 0.5%.It is possible to observe that for the membrane contrast agent concentration and thickness used, both top and bottom membrane interfaces can be fully resolved by the OCT system . No images were acquired of the membrane with concentration of 1% wt due to time constraints.

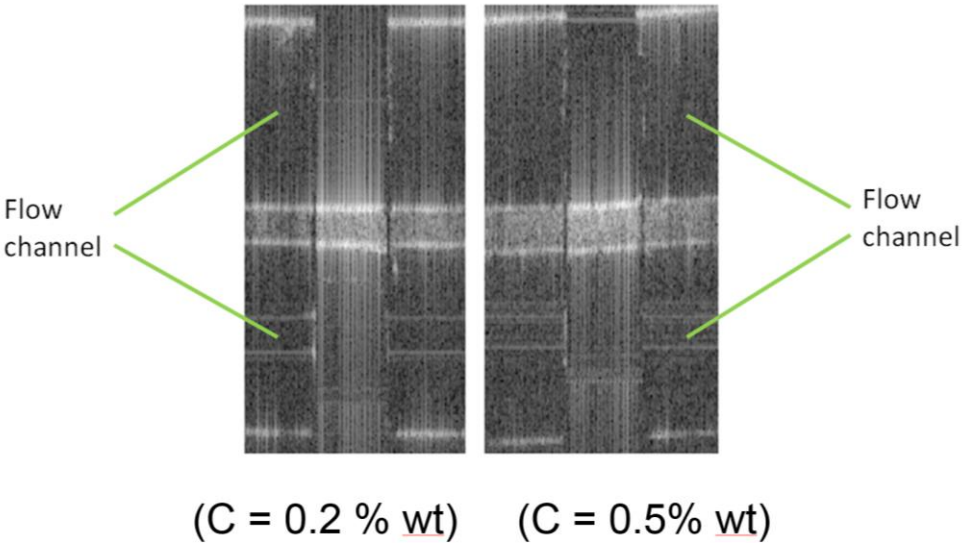

Figure 4-5. Scans of Nafion-TiO_2 membranes. Concentrations 0.2 (left) and 0.5% wt (right)

4.3 Image Filtering

As previously described in section 2.7, the OCT scans required noise filtering prior to image correlation in order to remove background noise and potential membrane superimposed noise. Firstly the intensities of the OCT scans were analysed with an intensity threshold to assess the possibility of superimposed noise on the membranes as seen in Figure 4-6 below.

It is important to point out that the OCT scans were saved as 8 bit image files. All images are composed of 2^8 (256) different intensities. An intensity value of zero is displayed as bright (white) and an intensity value of 255 is as the darkest pixel. All other points in between are a grey scale value.

The red dots on Figure 4-6 bellow show any intensities inside a specific range. The three scans seen in Figure 4-6 are for intensity values of 40-60 (a), 50-70 (b) and 40-90 (c). It is possible to see that there is a wide range of different intensities in the background in the vicinity of the membrane, probably due to unusable speckled noise. Furthermore, some of these intensities seem to be repeated on the membrane section of the scan. This is more apparent on the scan found on the right on Figure 4-6. This repeated intensities in background and membrane sections are probably due to speckled noise superimposed onto the membrane. This superimposed unusable noise is likely to negatively affect the speckle tracking results, as it adds randomness between successive scans.

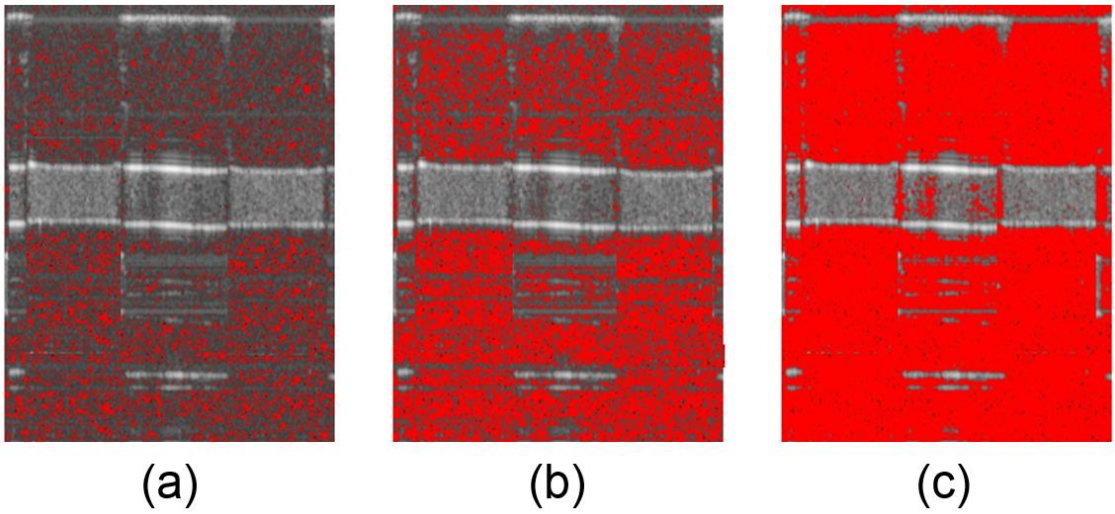

Figure 4-6. Intensity threshold of PDMS-TiO_2 membrane OCT scans prior to filtering. Intensities highlighted in red 40-60 (a), 50-70 (b) and 40-90 (c).

Spatial diversity was carried out using the open source software ImageJ. 50 stationary scans were taken and their pixel intensities were averaged. This operation can be carried out on ImageJ by following the commands: Image, Stacks, Z Project, Average Intensity. Figure 4-7 shows a comparison between the original unfiltered image (left) and the result of spatial diversity filtering (right).

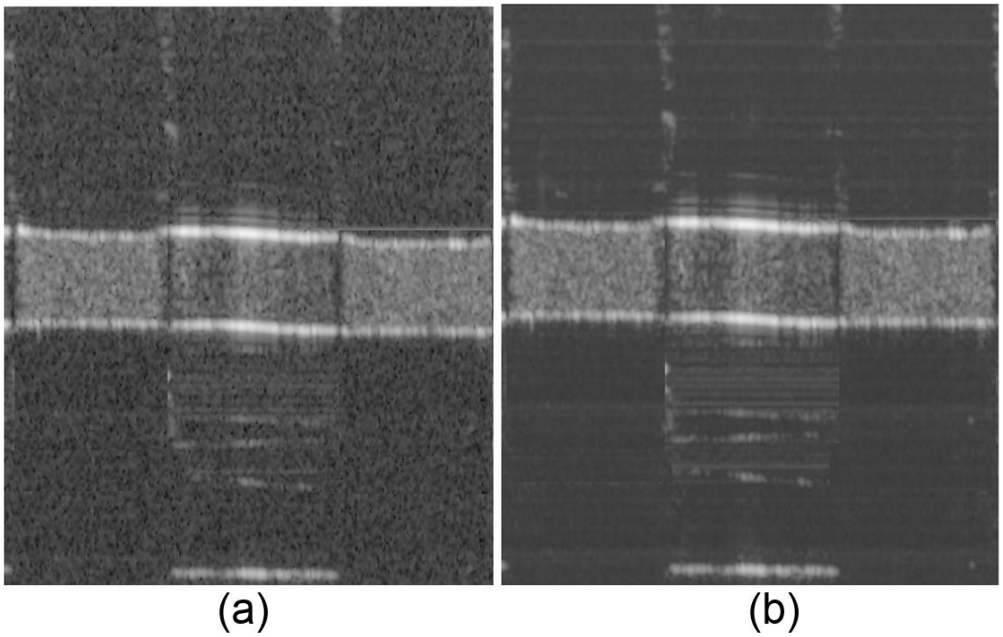

Figure 4-7. Comparison between OCT scans prior (a) and post (b) spatial diversity filtering making use of 50 scans, showing decrease in background noise.

An apparent reduction in the random background unusable speckled pattern is seen in Figure 4-7 after spatial diversity filtering is carried out. However, the usable speckled pattern in the membrane portion of the scan created by the titanium dioxide undergoes minor changes. It is believed that these minor changes in the usable speckled pattern of the membrane portion are related to the removal of superimposed random speckled noise. The removal of the superimposed noise is important it decreases the "randomness" between subsequent frames, allowing for smoother and more precise elastography results. Furthermore, the vicinity of the membrane may also be used for speckle tracking depending on the subset size and search area size. Randomness in the background may lead to erroneous displacement results, which is eliminated when noise is removed. Figure 4-8 below shows an image of the spatial diversity filtered scan found on Figure 4-7 with intensities values of 60-70 highlighted in red.

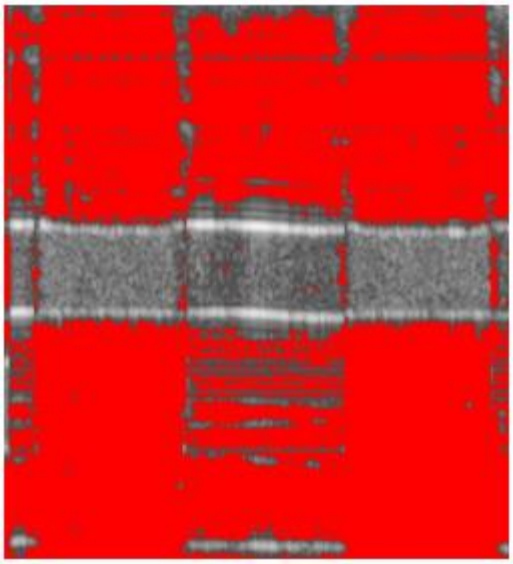

Figure 4-8. Post filtering threshold of OCT scan between intensities of 60-70 showing higher homogeneity in background and noise reduction.

After analysing Figure 4-8, it is possible to see that the variance of intensities in the background greatly diminishes after spatial diversity filtering is carried out. This is probably due to the averaging of the random intensities from noise with the intensity of the background. Furthermore, the membrane portion of the scan appears to be composed of different intensity values from the background. This is probably due to the elimination of

superimposed noise. It is believed that the speckled pattern present at the membrane post filtering is due to the presence of the contrast agent only, and not due to speckled noise.

4.4 Effect of Subset Size on Displacement Calculations

As mentioned in section 2.5.1 of this report, subset or interrogation window size selection is an important factor in the normalized cross correlation technique. It has been discussed previously in section 2.5 how inappropriate selection of subset size may affect the displacement results [47]. This section analyzes the effect of subset size on the thickness change estimations. Firstly data acquired from OCT scans and from microscope images were compared for pressure increment steps. As described in section 3.4.4, three measurements were taken from the microscope images and their results were averaged in order to improve the accuracy of the measuring technique, which is believed to be accurate to approximately ± 5%.

Squared subset sizes of 20, 30, 40 and 50 pixels were used in the MATLAB algorithm while conducting speckle tracking. Figure 4-9 below summarizes the strain as a function of clamping pressure for the various subset sizes compared to the averaged measured result from microscope.

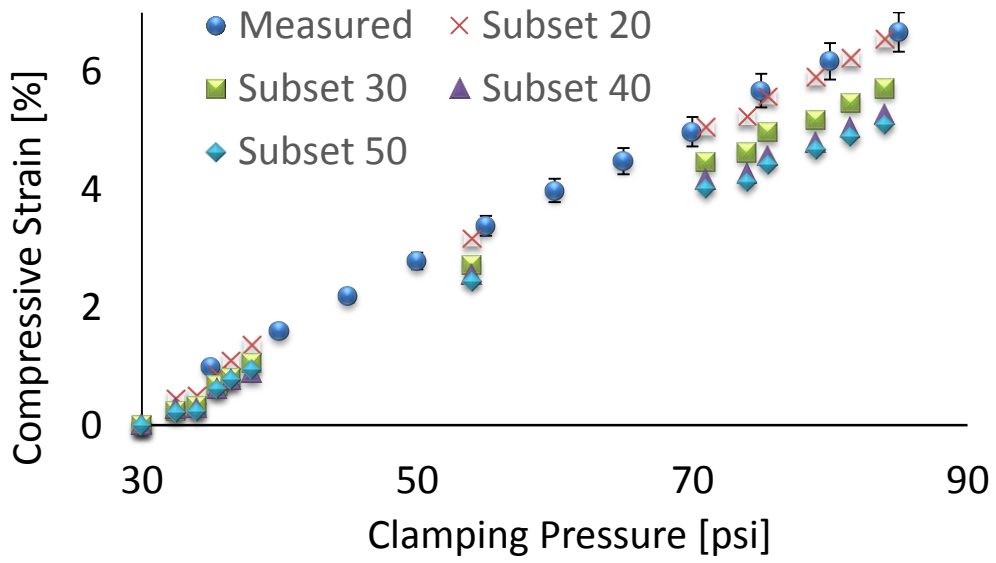

Figure 4-9. Comparison between measured and calculated PDMS-TiO_2 compressive strain at various subset sizes.

From Figure 4-9 it is possible to see that the scattered points follow an almost linear profile, in accordance with previous studies indicating that PDMS membranes have a linear stress-strain relationship up to compressive strain values of about 0.15 [61]. It is seen on Figure 4-9 how the subset size affects the strain calculations. As the subset size increases, the results acquire a tendency to be underestimated. A subset size of 20 pixels showed good agreement between calculated and measured results. The calculated results for this subset size fall inside the uncertainty of the measured results (± 5%) as seen in Figure 4-19. This strongly suggests that a subset size of 20 pixels is the most appropriate for DIC of the OCT scans used in this project.

Percentage difference between calculated and measured results for a pressure of 80 psi was calculated for the data displayed on Figure 4-9. The value of 80 psi was selected arbitrarily. Although the results of Table 4.3 could have been reproduced for the entire pressure range, it is believed that the variation between different pressure values would be insignificant. The variation for different pressure values can be found on Appendix A.

The results can be seen in table 4-3. The data displayed on table 4.3 show that the percentage difference between measured and calculated results is only of 2.19% when a subset size of 20 pixels is used. This falls inside the relative error of the measuring technique. As the subset size increased, this relative difference increased as well, up to a value of almost 23% when a subset size of 50 was used. The data on table 4-3 strongly suggests that a subset size of 20 pixels is the most appropriate for carrying out DIC with the OCT scans used in this project.

Table 4-3. Strain Percentage Error for Different Subset Sizes at 80 psi

Subset Size	Calculated Strain at 80 psi	Measured strain at 80 psi	percentage difference [%]
SS 20	0.060	0.062	2.19
SS 30	0.053	0.062	14.29
SS 40	0.049	0.062	20.67
SS 50	0.048	0.062	22.89

The images acquired from the microscope were also use for digital image correlation, as they possess a clear speckle pattern. In order to investigate its accuracy and appropriate subset size, the speckle tracking results were compared to measured results, as described

in section 3.4.4. A membrane with contrast agent concentration of 0.2 % wt was used, with its humidity increasing from 30% to 84% in steps of approximately 5% at a constant temperature of 50 °C. Figure 4-10 below shows the measured and calculated results found for different subset sizes.

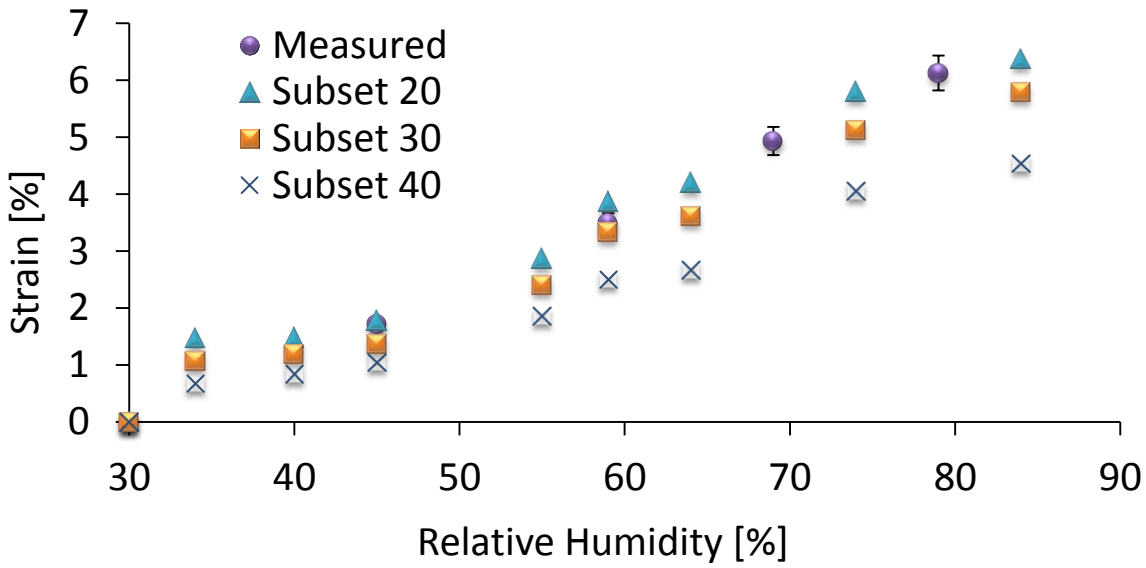

Figure 4-10. Compassion between measured and calculated Nafion-TiO_2 hygro-strain at various subset sizes

As seen from Figure 4-9 above, the results displayed in Figure 4-10 there is good agreement between the measured data and the data found from DIC using a dubset size of 20 pixels. Figure 4-10 above strongly suggests that the most appropriate subset size for speckle tracking on microscope images is also of 20 pixels.

As mentioned in the literature, the use of inappropriate subset sizes may lead to erroneous strain calculations [47]. This would ultimately lead to a loss in the capacity to carry out microstructural assessment. As the image correlation was carried out in small pressure step or humidity increments, the speckled pattern from frame “n” to frame “n+1” is expected to be very small. It is thought that larger subset sizes may not be able to detect these small changes, leading to the underestimation of displacement. A subset size of 20 pixels was therefore taken as the most appropriate for both OCT scans and images collected in this project.

Although the exact accuracy of the DIC technique is unknown, it is estimated to be approximately 6 % when a subset size of 20 pixels is used based on the results of Figures 4-9 and 4-10. For the accuracy calculation of the technique, please refer to Appendix B. The accuracy of the technique may be affected by small temperature variations, the accuracy of relative humidity sensors or noise inherent from speckle tracking. The data in the following sections take the "worst case scenario" taking error bars of ± 6% for calculated strain results. The relative humidity sensors used in this project have a reported accuracy of ± 2%. The subsequent error bars for humidity are therefore taken as ± 2%.

4.5 Smoothing and edge effects

Even though a subset size of 20 pixels suggested to be the most accurate, smaller subset sizes also tend to provide higher degree of noise in results due to the smaller amount of information within the subset [51]. Vector displacement maps tend to me more well defined and have a clearer appearance for larger subset sizes. Figure 4-11 below compares a vector map between the subset sizes of 20 and 40 pixels for a pressure increment from 30 to 80 psi.

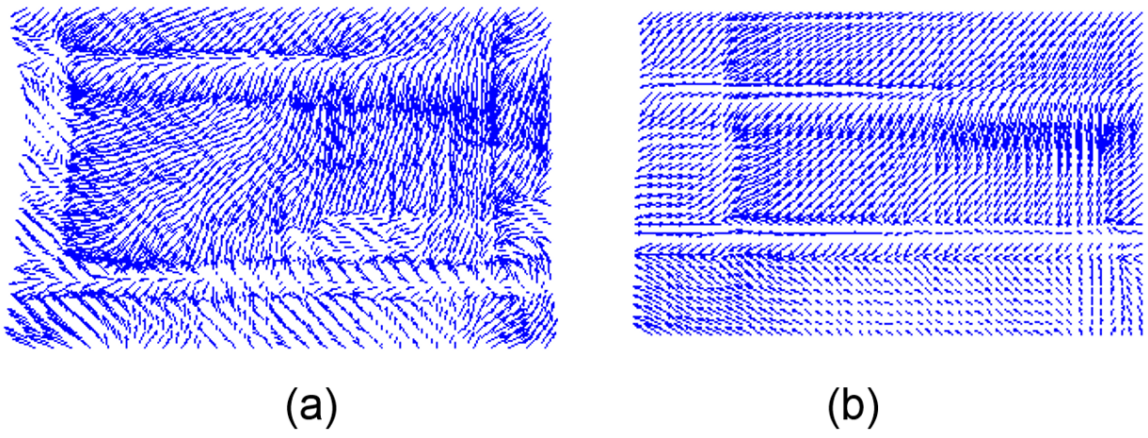

Figure 4-11. Displacement vector field for pressure of 80 psi at subset size of 20 pixels (a) and 40 Pixels (b).

The vector field obtained when a subset size of 40 pixels was used shows a good agreement with expected results for compression. The two outer edges show an inward

displacement, while the center of the membrane shows a small vertical displacement value. Most vectors showed displacements almost entirely in the vertical direction with a small component in the horizontal direction. A small difference in vector magnitude may also be seen between top and bottom of the membrane. This magnitude difference is due to slight misalignments of successive scans. However, as thickness change is calculated as the difference in displacement between top and bottom, misalignments have no impact on thickness change calculations.

An obvious erroneous displacement can be seen near the centre of the membrane after careful analysis of the vector field of subset size of 40 pixels. This artifact is highlighted on Figure 4-12 with a green ellipse.

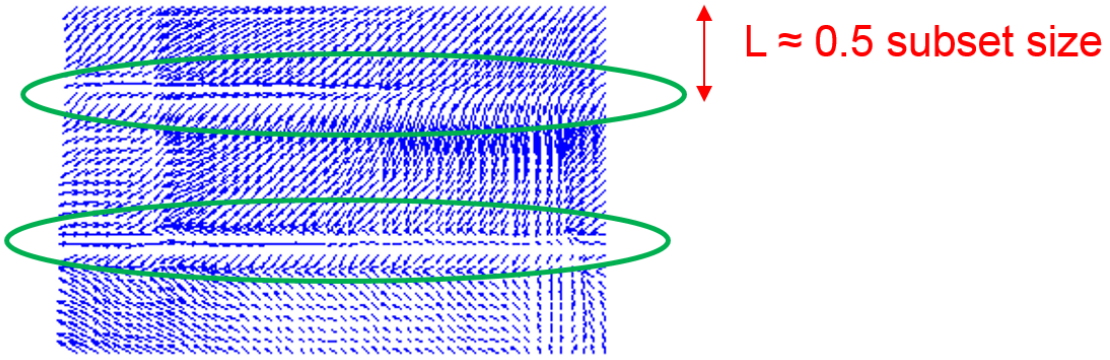

Figure 4-12. Highlighted artifacts due edge effects.

The two artifacts show erroneous displacements near the center of the membrane. An erroneous upward displacement may be seen slightly below the center of the membrane, while an erroneous downward displacement is seen slightly above the center of the membrane. The distance "L" of these artifacts from the edges of the membrane was found to be approximately the same as half the size of the subset. When different subset sizes were used, it was found that this distance "L" was always half the subset size, regardless of the subset size used. It is believed that this happens is due to edge effects. Figure 4-13 below shows a schematic of the subset around one of the control points in the membrane.

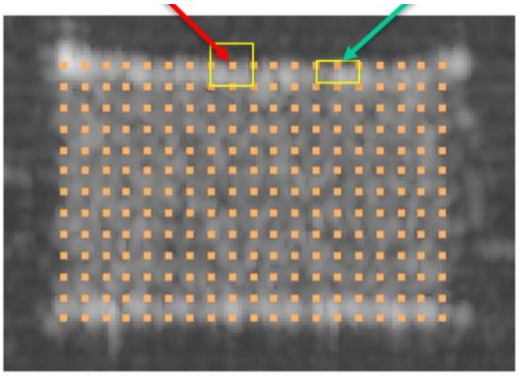

Figure 4-13. Subsets near the edge of membrane

Subsets for control points near the edge of the membrane use partially membrane information and partially background information for calculating relative displacements. This can be seen in the control point pointed out with a red arrow in Figure 4-13. It is believed that this proximity to the edge may lead to erroneous displacements. One possible technique for correction of these edge effects would be to use variable subset sizes near the edge of the membrane. These variable subset sizes could be controlled not to take in account any of the background, possibly fixing this issue. However, writing and or modifying the speckle tracking algorithm falls outside the scope of this project. Another commonly used technique for fixing erroneous displacements carried out a technique called "smoothing" or "spatial filter" [47, 51].

This technique averages calculated results in the vicinity of control points. This can be done either through mean averaging or by applying a Gaussian distribution of weights. While using smoothing it is important to carefully select the smoothing parameters in order not to negatively affect thickness change calculations. Figure 4-14 below shows the vector field of a pressure step change from 30 to 80 psi using a subset size of 20 pixels. The vector field on the left (a) of Figure 4-14 is the original vector field prior to the smoothing treatment. The vector field on the right (b) underwent a Gaussian smoothing using 11 control points and 3 passes.

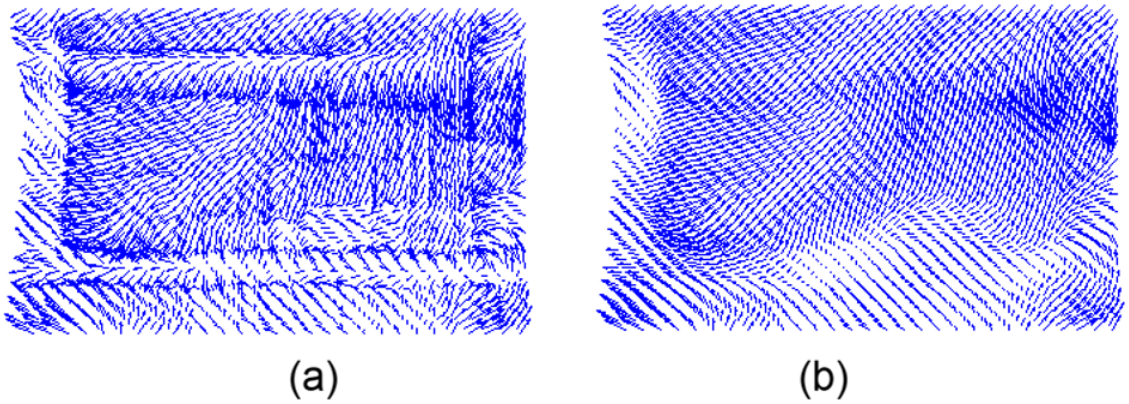

Figure 4-14. Comparison of displacement vector field for a pressure of 32.5 psi at subset size of 20 pixels prior (a) and post (b) 3 smoothing passes

The smoothed vector field (b) found of Figure 4-14 possess a higher degree of homogeneity than the original (a) vector field. Even though a significant improvement in appearance is noted, this procedure could lead to potential erroneous displacement calculations. In order to study the effect of smoothing on displacement calculations, the thickness change was plotted for a pressure range from 30 to 80 psi. Subset sizes of 20 with no smoothing, 1 smoothing pass and 3 smoothing passes were used. The results are found on Figure 4-15 below.

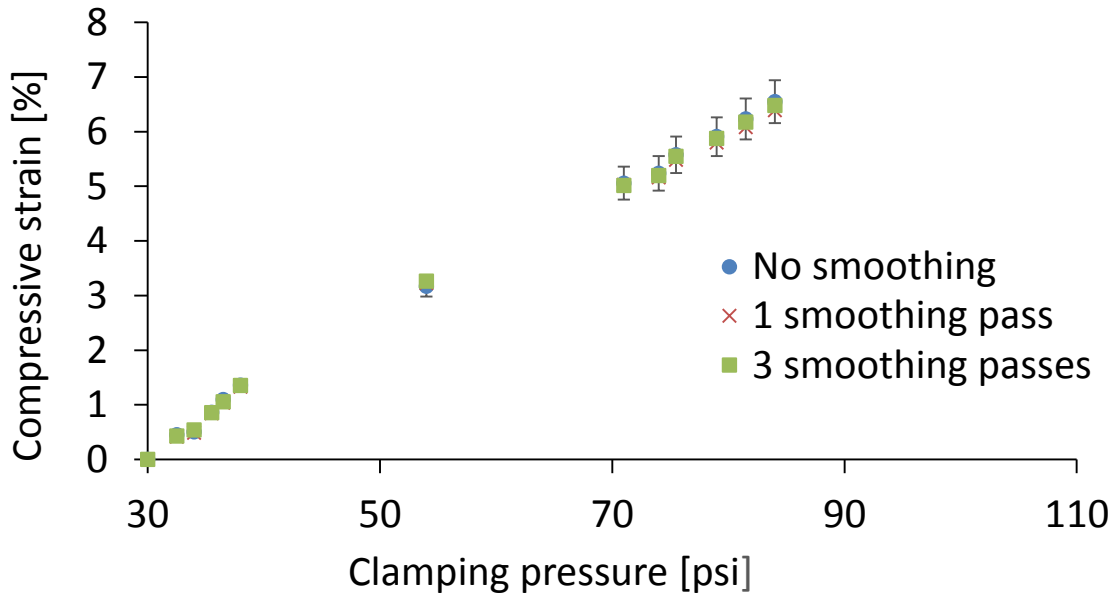

Figure 4-15. Comparison between calculated PDMS-TiO_2 compressive strain at subset sizes of 20 pixels for different smoothing parameters.

Even though a significant visual improvement is seen after smoothing the results, the impact on thickness change calculations is almost negligible as seen in Figure 4-15 above. The calculated points for 1 and 3 smoothing passes fall inside the error bars for the data with no smoothing, as displayed on Figure 4-16. Similarly to section 4-4, the results at a pressure of 80 psi were compared for a percentage difference analysis. The results are found on Table 4-4 below.

Table 4-4. Strain Percentage Error for Different Smoothing Parameters

# of passes	Calculated Strain at 80 psi	Calculated strain at 80 psi no smoothing	percentage difference [%]
1 pass	5.913	6.038	2.07
3 passes	5.995	6.038	0.71

The results shown in Table 4-4 above and Figure 4-14 and Figure 4-15 suggest that while smoothing is a powerful technique for achieving higher homogeneity of vector fields, the technique has little impact on the calculated strain values for the membrane, as the results from 1 and 3 smoothing passes fall inside the error bars of the original data. It is therefore accepted that a Gaussian smoothing with 3 passes is most appropriate for the purposes of this project. The results presented in the following sections, i.e. sections 4.6 and chapter 5, all underwent 3 smoothing passes.

4.6 Effect of Contrast Agent Concentration on Nafion-TiO_2 Membranes Swelling

After finding the appropriate subset size for displacement measurements and studying the effect of smoothing on relative motion calculations, the swelling behaviour of Nafion membranes can be studied making use of the speckle tracking technique. However, as mentioned earlier in, Nafion membrane used in this report were mixed with a contrast agent in order to provide speckles. In order to assure the presence of such filler has no impact on swelling measurements, this section studies the swelling behaviour of Nafion membranes with different contrast agent concentrations.

The swelling of membranes with concentrations of 0.2 and 0.5 % wt was obtained from OCT scans at a temperature of 80 °C and a clamping pressure of 100 psi. The swelling behaviour with contrast agent was also studied in microscope images through speckle tracking. Concentrations of 0.2, 0.5 and 1% wt were studied through microscope images for membranes without GDE layers. Membranes of Concentrations of 0, 0.2 and 0.5% wt were studied for membranes sandwiched by GDE layers. All microscope acquired images in this section were carried out at a temperature of 50 °C. The clamping pressure of all experiments was set to 100 psi.

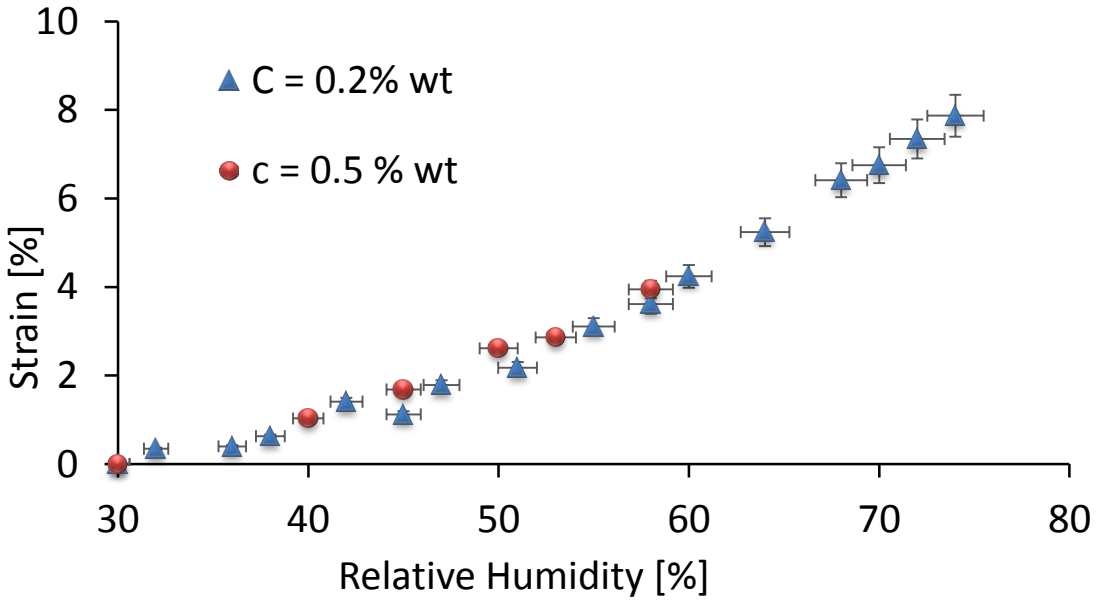

Figure 4-16. Swelling strain for Nafion-TiO_2 membranes acquired from OCT scans at contrast agent concentrations of 0.2 and 0.5% wt.

As seen in Figure 4-16, the increase in concentration from 0.2 % wt to 0.5% wt has an apparent small effect on the swelling behaviour of Nafion. On average the data for a contrast agent concentration of 0.5% was slightly higher than that found for a contrast agent concentration of 0.2% wt. However, even though this small variation can be observed, the difference between the two data sets is comparable to the estimated accuracy of the technique (approximately 6%). Previous studied of the subject concluded that low concentrations of TiO_2 led to only minor changes on membrane mechanical properties [11, 24], while membrane preparation method has by far a stronger impact. The concentrations

used in the studies by Satterfield et al were up to 3%, 6% and 20% wt. The data presented by the authors suggested that lower concentrations of TiO_2 had very small impacts on mechanical properties. The most significant difference between bare Nafion membranes and composite membranes was on water retention upon dehydration. Furthermore these contrast agent concentrations were significantly higher that the values used in the current study. It is believed that for the low concentrations used in the current project, the difference between the values observed in Figure 4-16 are due to experimental errors and within the accuracy of the technique. The DIC technique with the current parameters used in this project is believed not to have the necessary accuracy necessary to detect changes in mechanical properties when low concentrations of TiO_2 are used.

Similar results were found from carrying out speckle tracking on microscope acquired images. Figure 4-18 below shows a scatter plot for DIC results carried out from microscope acquired images of membranes with concentrations of 0.2, 0.5 and 1% wt. Similarly to what was found on OCT scans, the results of all three concentrations was observed to be very similar. The variation between the three data sets was found to lie within the accuracy of the DIC technique for the majority of the data.

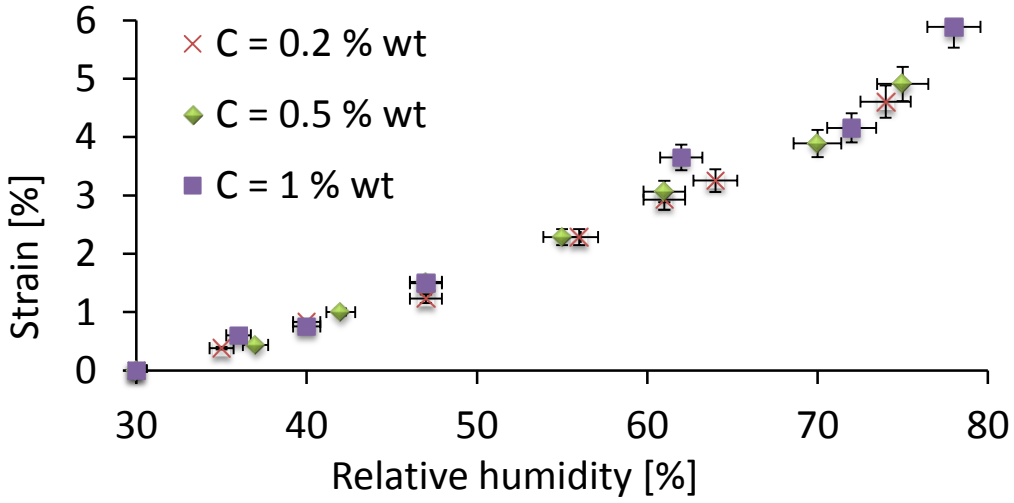

Figure 4-17. Swelling strain for Nafion-TiO_2 membranes acquired from microscope images at different contrast agent concentrations.

The results presented in this section suggest that the use of low concentrations of TiO_2 powder on Nafion membranes has little impact on its mechanical properties. Previous studies found higher concentrations (3, 6 and 20%) to have a negative impact on the plastic modulus of the membrane. However, little difference was observed in the elastic modulus of the material as TiO_2 concentration changed. Furthermore, the concentrations used in the current project were substantially lower than those used by Satterfield et al. , the low concentrations used in this project (0.1, 0.2, 0.5 and 1 % wt). A small variation was observed between the collected results from different contrast agent concentrations, however these variations lie within the accuracy of the technique and are believed to be experimental error. It is therefore concluded that the concentrations tested in the project only lead to minor changes in mechanical behaviour of the material, not detectable using the current DIC technique. However, as the exact impact could not be quantified due to the accuracy of the technique, the concentration of contrast agent is still suggested to be kept to a minnium.

4.7 Summary

In this chapter the results of the validation testes were presented and analysed. The results of this chapter indicate the most appropriate parameters to be used while carrying out DIC of OCT scans and microscope acquired images.

Section 4.1 presented example OCT scans of Nafion-TiO_2 membranes being imaged through a polycarbonate flow channel. The Apparent shift in membrane land and channel sections was associated with an optical path length difference.

The opacity of different combinations of contrast agent and membrane thickness was analysed in section 4.2. It was found that membranes with a contrast agent concentration of 1% could not be imaged fully when their thickness was higher than 200 µm. However, as all Nafion membranes cast for this project were thinner than 100 µm, it was found that any concentration lower than 1 % wt were appropriate for the use of DIC through OCT scans.

Section 4.3 presented the results of spatial diversity filtering of OCT scans. It was shown how OCT scans underwent a significant decrease in background noise post spatial diversity

filtering. Intensity threshold showed how the variation in random background intensity decreased as filtering was applied.

Section 4.4 studied the effect of subset size on the calculated DIC results. The results from subset sizes of 20, 30, 40 and 50 pixels were compared to a reference measured value. It was found that when a subset size of 20 pixels was used, the calculated results fell within the experimental error of the measured results. As the subset size increased, the strain values became increasingly underestimated. All subsequent DIC calculations were carried out using a subset size of 20 pixels.

In section 4.5 the impact of smoothing of results was analysed. It was found that vector fields that underwent smoothing presented a significantly higher degree of homogeneity and decreased noise. However, when thickness change calculations were carried out for non-smoothed a smoothed results, it was found that the variation was within the accuracy of the technique and taken to be negligible. All subsequent DIC calculations were carried out making use of 3 smoothing passes.

The effect of contrast agent on the mechanical properties of composite Nafion membranes was assessed in section 4.6. A small variation was found between different concentrations of contrast agent. However these variations were comparable to the accuracy of the technique and taken to be experimental error. It was found that the low concentrations of contrast agent used in this project have no detectable impact on swelling strain based on the current technique.

Chapter 5: Results and Discussion

The results of the validation experiments were presented on chapter 4. The previous chapter demonstrated the steps necessary for filtering of OCT scans in order to remove background noise and improve image quality. A subset size of 20 pixels was found to output the most accurate results when compared to a reference measurement. The impact of smoothing was assessed and found to have no significant impact on DIC results. Lastly the impact of contrast agent concentration was found to be within the accuracy of the present technique used. Once all these parameters have been tested and assessed, more representative tests can be carried out in order to measure membrane swelling strain. This chapter presents the results from humidification studies carried out in OCT scans and microscope acquired images.

The effect of GDE layers is assessed on section 5.1. Swelling strain was calculated using DIC with and without GDE layers. A compression between land and channel sections of the membrane was carried out and theirs results are compared when GDE layers are present and absent.

Section 5.2 presents through thickness displacement maps of OCT scans and microscope acquired images. Vector fields and contour plots are presented showing the displacement distribution as imaging depth changes. Strain distribution plots are presented in this section.

Section 5.3 shows membrane scans acquired from an in situ test set up that show the potential of OCT DIC to be carried out in situ.

Section 5.4 analyses the current issues experienced and lays recommendations for future work.

5.1 Effect of GDE layers and Location on Swelling

This section studies the effects of changing parameters in swelling strain in Nafion-TiO_2 membranes. Firstly the difference between swelling in land and channels sections was studied. These results were further compared for cases were GDE layers were present and absent.

A comparison between land and channel can be seen for an OCT scan of a membrane containing a TiO_2 concentration of 0.2% wt and no GDE on Figure 5-1 below. The two scans show the membrane at humidity values of 30 % (a) and 82 % (b). It is seen that while the sections of the membrane under the land increased in thickness with humidity, the section under the land also underwent buckling.

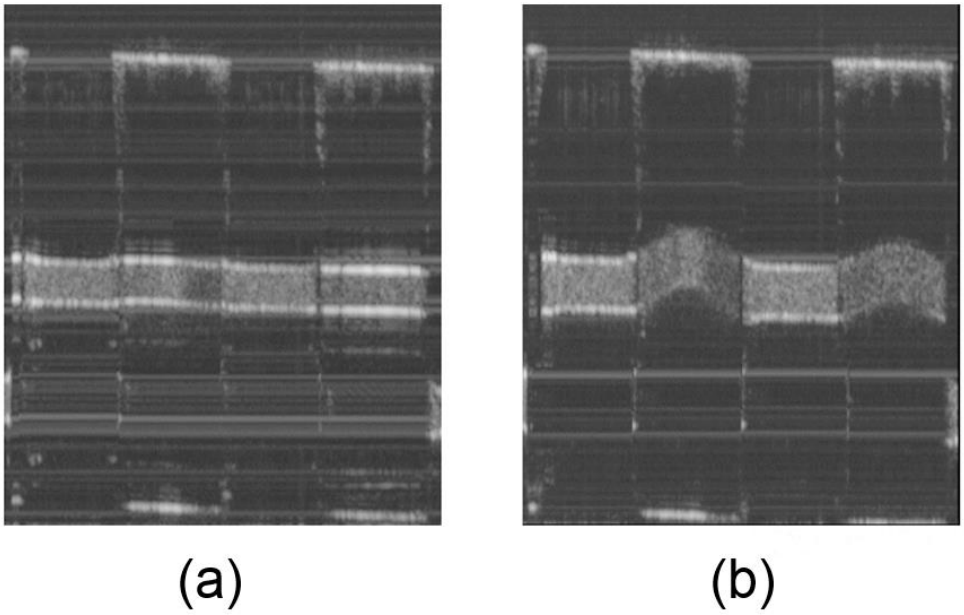

Figure 5-1. Comparison between nafion-TiO2 membrane at 30% (a) and 82 % (b) relative humidity.

The section of the membrane under the land is constrained by the clamping pressure of the polycarbonate plates. This keeps the membrane from buckling and limits the amount of swelling strain experienced. However, at the land section the membrane is unconstrained in the thickness direction, allowing it to undergo higher swelling strain than the land section. Figure 5-2 shows the evolution of contour plots for displacements in the thickness direction. The humidity values displayed on Figure 5-1 are 51 (a), 55 (b), 60 (c) and 64 % (d).

From the contour plots displayed on Figure 5-2, it can observed how displacement is highly dependent on location for the channel section of the membrane. The highest strains take place near the center of the channel section while the sides experience lower strain. It can also be seen how displacements are lower near the bottom of the membrane, but higher near the direction of buckling. Figure 5-3 shows the difference in swelling strain between

land and channel sections of a Nafion-TiO_2 membrane with a concentration of 0.2% wt at 80 °C.

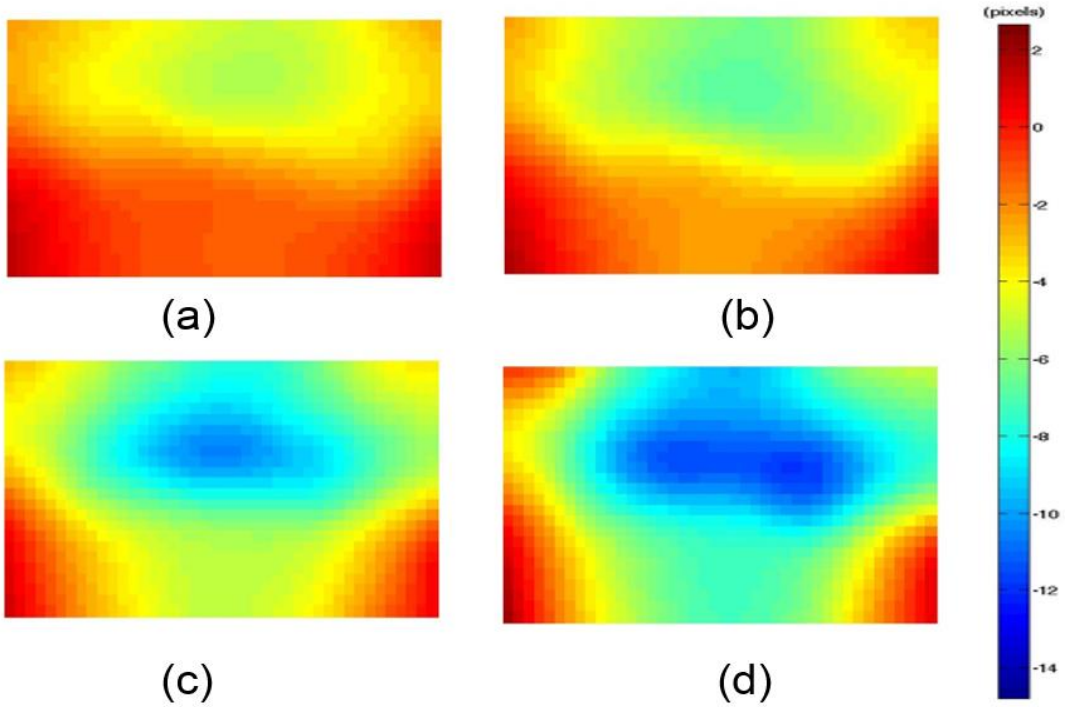

Figure 5-2. Evolution of displacement in thickness direction for membrane channel section of membrane for humidity values of 51 % (a), 55% (b), 60% (c) and 64 % (d)

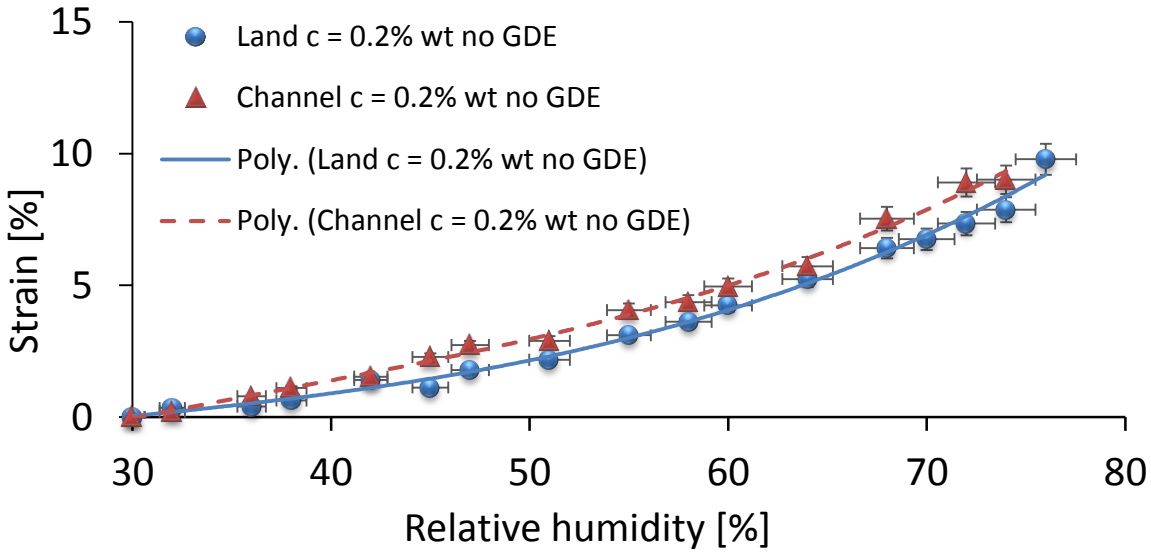

Figure 5-3. OCT comparison of swelling strain between land and channel sections of a membrane with no GDE for a TiO_2 loading of 0.2% wt.

Polynomials of order 3 were fitted to the curves of swelling strain, in accordance with previously published studies [2]. It can be observed that the land section of the membrane undergoes higher swellings strain than the channel section of the membrane. Error bars were fitted into the points shown in Figure 5-3, similarly to what is observed on Figures 4-15 to 4-17 in chapter 4. On average the channel section of the membrane underwent 25 - 30% more strain than the land section. This difference is significantly greater than the uncertainty of the technique, displayed as errors bars in Figure 5-3. As mentioned previously, this is most likely due to the constraints applied to the membrane. The land section of the membrane is constrained by the polycarbonate flow channel plates, which applies a clamping compressive force on the material. However, the channel section of the membrane in unconstrained in the through thickness direction, hence it has more freedom to expand. As swelling occurs due to membrane water content [29], as described in chapter two, it is believed that the channel section of the membrane is able to absorb a higher quantity of water than the land section.

Similar results can be seen in Figure 5-4. Land and channel sections of the membrane are compared for a TiO_2 loading of 0.5% wt, opposed to 0.2 % wt as shown in Figure 5-3. The results of Figure 5-4 show that the channel section of the membrane also undergoes 25-30 % more strain than the land section, values considerably higher than the uncertainty of the technique.

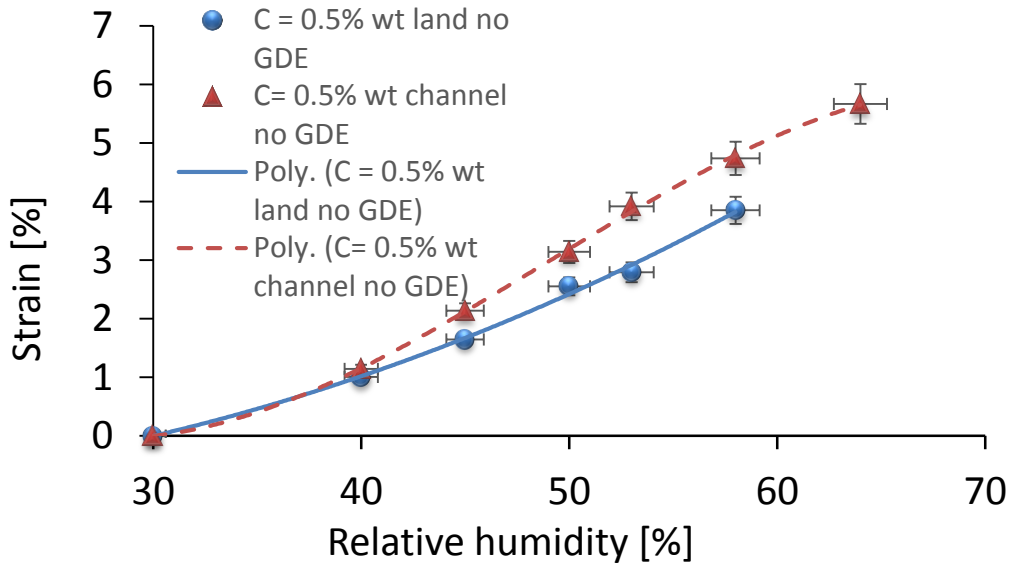

Figure 5-4. OCT Comparison of swelling strain between land and channel sections of a membrane with no GDE for a TiO_2 loading of 0.5% wt.

Figure 5-5 shows similar results than those of Figure 5-3 and Figure 5-4, however the results on Figure 5-5 are for a GDE sandwiched membrane. It can be seen that even in the presence of GDE, the membrane still undergoes approximately 30 % more swelling on channel than on the land section. It is seen that for the upper part of the humidity range (values above 60%), the difference between these two lines is seemingly lower. At lower values, the difference between the two is more easily noticeable. This difference between upper and lower values is believed to be due to experimental errors and the accuracy of the technique. Similarly to what occurred when GDE layers were not present, the membrane is constrained in the thickness direction by the flow field plates in the land section, but only constrained by the fibrous GDE in the channel section. As GDE layers are relatively soft on the bending direction, the membrane is able to undergo higher swelling in the channel section.

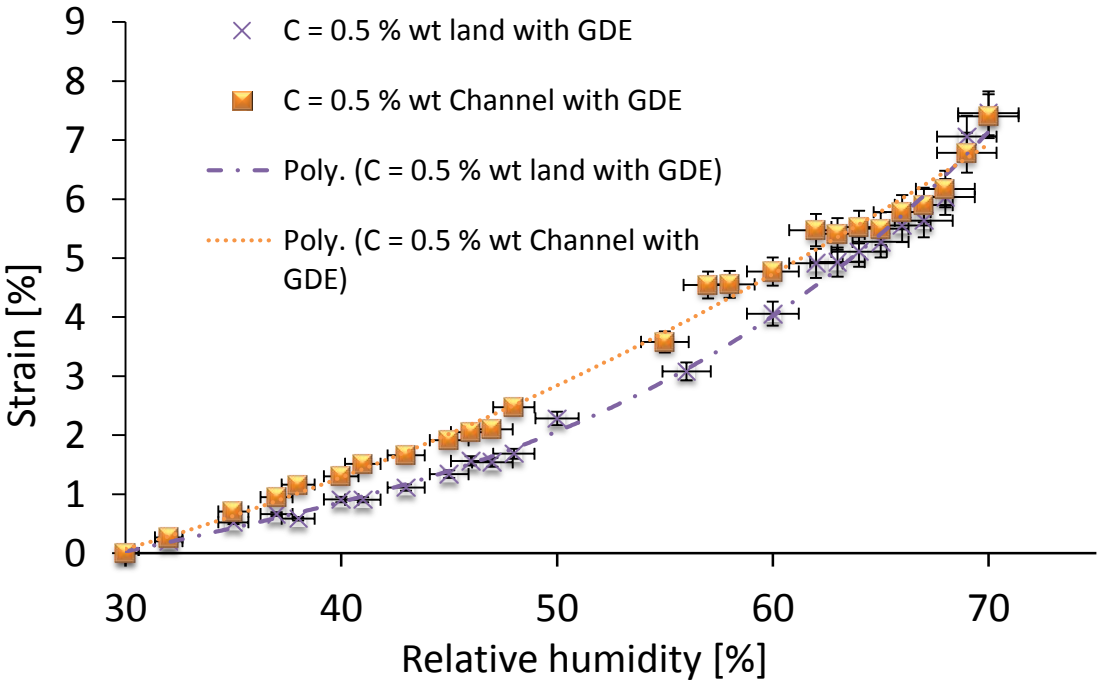

Figure 5-5. OCT comparison of swelling strain between land and channel in GDE sandwiched membrane with TiO_2 loading of 0.5% wt.

Figure 5-6 compares the swelling on land sections with and without the presence of GDE layers. Similarly, Figure 5-7 compares swelling on channel only for membranes with and

without GDE layers. It is seen that in both cases when the membrane is sandwiched by GDE layers the swelling is slightly lower.

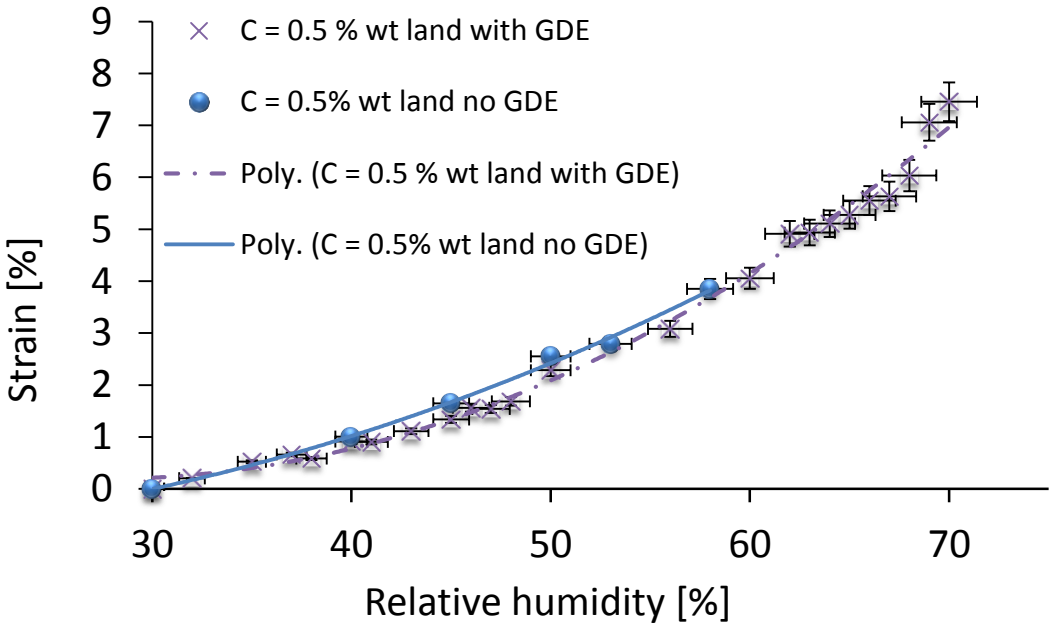

Figure 5-6. OCT swelling strain at land section of membrane for membranes with and without GDE layers.

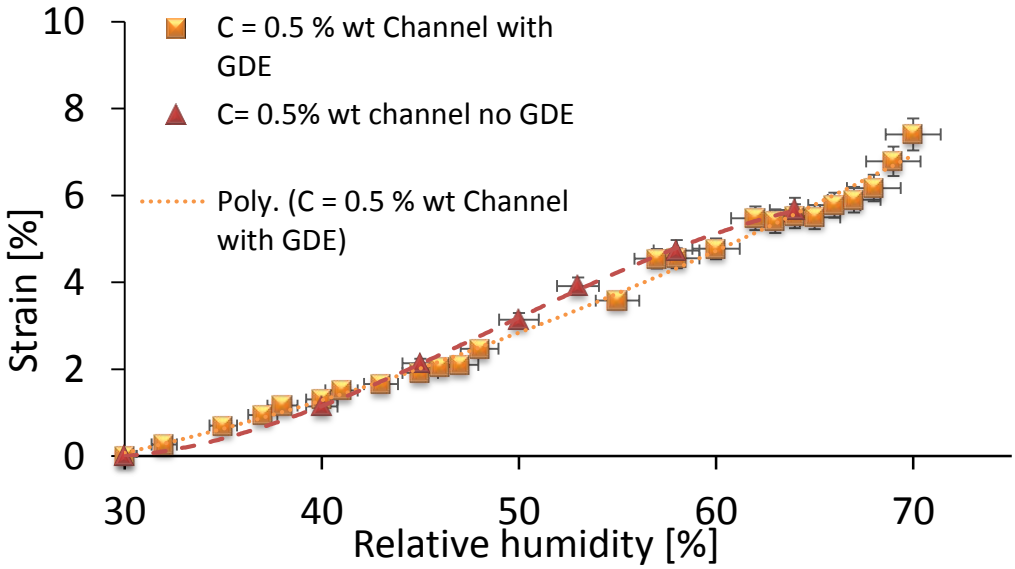

Figure 5-7. OCT swelling strain at channel section of membrane for membranes with and without GDE layers.

At the land section of the membrane the swelling reduces in approximately 12 - 14 % when GDE are present. However, when the error bars are analysed, it can be seen that this difference is on the limits of the experimental accuracy. This difference was slightly lower for the channel section of the membrane, where only a 10 - 12% decrease in swelling was noticed when GDE layers were present. Similarly, this difference between the two curves of Figure 5-7 is within the accuracy of the technique. Based on the current results, it is difficult to quantify the exact impact that GDE layers have on swelling strain. However, it is possible to see that the majority of points found on Figures 5-6 and 5-7 are lower when GDE is present. Furthermore, the polynomial best fit curves are for the great majority lower in both Figures 5-6 and 5-7 are GDE is present. The two curves intersect at some points, especially at lower humidity values. It is believed that there is in fact a decrease in strain with the introduction of GDE layers as shown in Figure 5-8 . However, its impact is very small, and approximately in the order of 6 – 8%, but the exact quantification of this value is hard to estimate given accuracy of the current technique. In order for a more statistical relevant analysis to be carried forward, it is recommended for the experiment to be repeated at least 10 times and its values averaged.

To the knowledge of the author, there is currently a lack of studies comparing the through thickness strain in Nafion membrane with and without the presence of GDE layers or GDL. The decrease in swelling strain with the addition of GDE is believed to be an interplay between water absorption and stress redistribution through the fibrous structure of the GDE.

The presence of GDE is believed to introduce better stress distribution on the membrane. When no GDE was used, the clamping pressure of the polycarbonate flow field plates was concentrated on land only, as there was no contact between flow channel plates with the channel section of the membrane. However, when the GDE layers are introduced to the system some of the clamping pressure that was applied to land only is believed to lead to an increase in restrain the channel section, ultimately leading to lower strains at the channel. The added constraint at the channel section leads to lower strain and therefore lower water content. As the channel section experiences slightly lower water content when GDE is introduced, it is believed that less water is available to diffuse back to the land section. This decrease in water diffusion from channel section to land section leads to a

lower water content at the land as well. Hence the swelling experienced by the land section of the membrane with the addition of GDE is also reduced. Furthermore as the GDE material is relatively soft, it is believed that the GDE layers absorb some of the swelling pressure. Although clear trends can be seen from Figure 5-5 through Figure 5-7, it can be seen from Figure 5-8 that some variations were present on the percentage difference between all polynomial curves. For a humidity value of 40% the channel seemingly presented lower swelling strain with the absence of GDE, while the opposite was found for the rest of the humidity range, as shown below in Figure 5-8. This difference is believed to be due to experimental errors. The percentage difference between these two data points also varied between humidity values. The difference was about 10- 12 % for most of the humidity range, however lower values were seen at the extremities of the curves. Variations were also seen when the results of land with and without the presence of GDE were compared throughout the humidity range. These variations are attributed to experimental errors and the accuracy of the technique. Only one point was collected for each data set. For a more precise analysis, it is recommended that more data points be taken in the future.

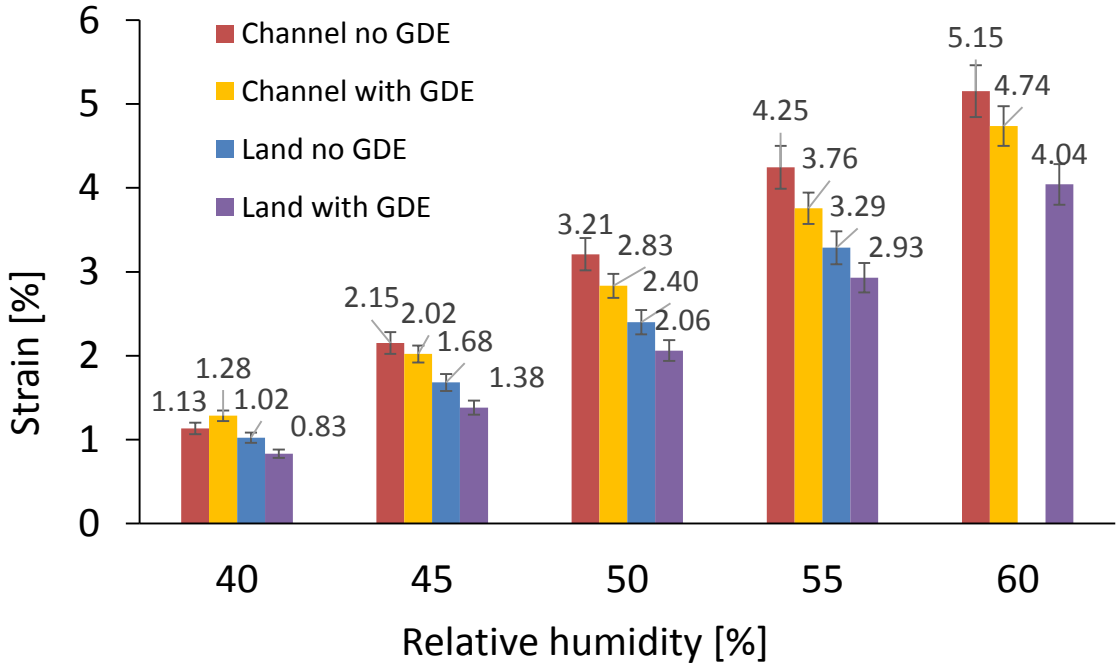

Figure 5-8. Swelling strain with and without GDE at land and channel locations for various humidity values.

5.2 Through Thickness Displacement Maps

As mentioned in the in the first three chapters, DIC was used in this project as it is able to not only measure thickness change, but it is also able to measure through thickness strain distributions based on the input images. This sections shows the results for through thickness strain distributions through vector fields or contour plots. The results shown in this section are for both microscope images and OCT scans.

A Nafion-TiO_2 membrane of concentration = 0.2% wt sandwiched by GDE layers was used for the demonstration of the technique. Microscope images were firstly used do to the high number of pixels in the images, leading to ease in calculating strain maps. Figure 5-9 below shows vector fields representing the evolution of strain in the land section of the membrane as humidity increases. The tail of the vectors represent the position of the control point in the reference image, while the tip of the vectors represent their position in the deformed images. For ease of visualization and interpretation, the spacing between each vector is of 8 pixels. The vectors displayed on Figure 5-9 were scaled by a factor of 10.

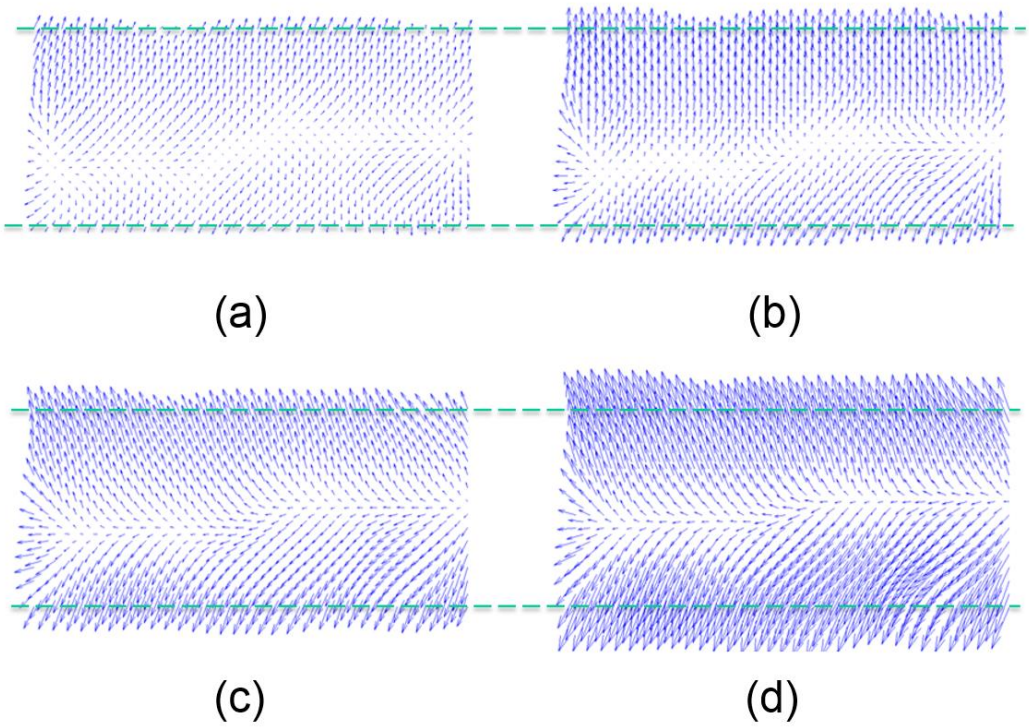

Figure 5-9. Vector field for displacement of a Nafion-TiO_2 membrane c = 0.2% wt sandwiched by GDE layers. Humidity values of 40 % (a), 50 % (b), 55% (c) and 76 % (d). Green lines approximately represent reference boundaries of membrane

It can be seen from the vector fields displayed on Figure 5-9 that the displacement is nearly zero at the center of the membrane, as all images were aligned in that position. The displacement gradually increases towards the top and bottom edges of the membrane. The displacement at top and bottom interfaces are seemingly comparable, which is to be expected as the humidity was uniform throughout the membrane. It can also be seen that the magnitude of displacement greatly increases with humidity value. Figure 5-10 shows similar results to those of Figure 5-9 but in the format of contour plots.

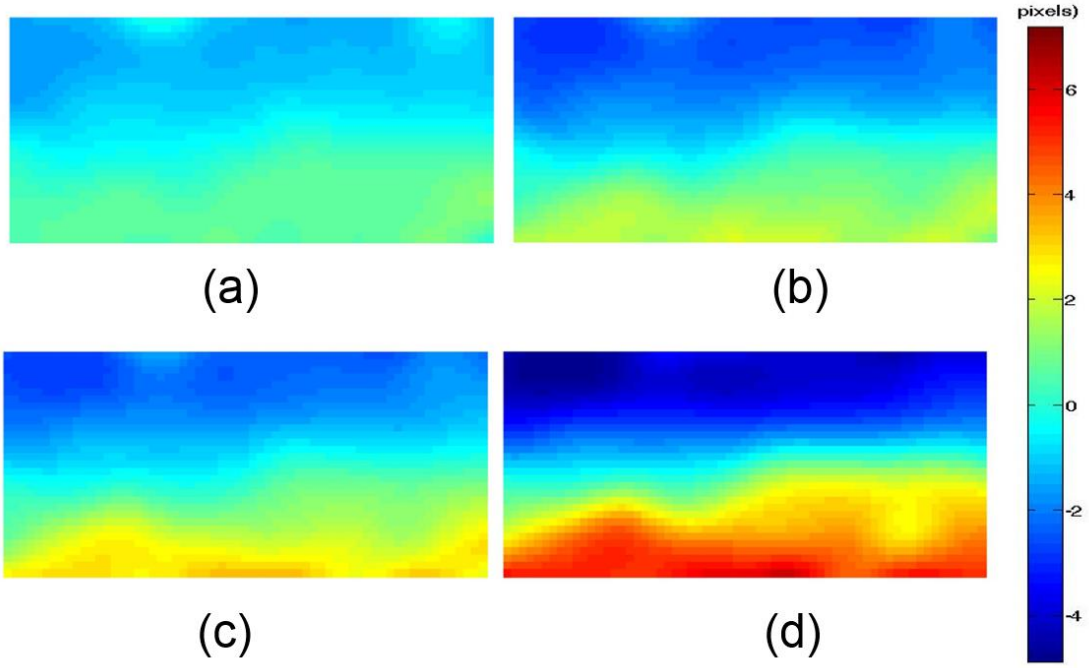

Figure 5-10. Contour plots for displacement in thickness direction for a Nafion-TiO_2 membrane c = 0.2% wt sandwiched by GDE layers. Humidity values of 40 % (a), 50 % (b), 55% (c) and 76 % (d)

The contour plots displayed on Figure 5-10 above, show displacement in the thickness direction for a Nafion-TiO_2 membrane of c = 0.2% wt. The colour scale on the right of the image show the number of pixels each control point was displaced in the thickness direction. As shown in the vector field in page 97, the thickness change towards the centre of the membrane was approximately zero, as the membranes were all aligned reference to that point. The displacements gradually increased towards upper and lower edges of the memrbane. Furthermore, the membrane shows a relatively homogeneous displacement

throughout the x direction of the contour plots. The small variations are believed to be experimental errors.

Figure 5-11 shows the pixel displacement as a function of normalized membrane thickness. Negative values represent the top of the membrane while positive values represent the bottom of the membrane. A value of zero represents the center of the membrane. The plot is for a membrane humidified to a relative humidity value of 76% and a temperature of 50 °C. The data displayed on Figure 5-11 was acquired on microscope.

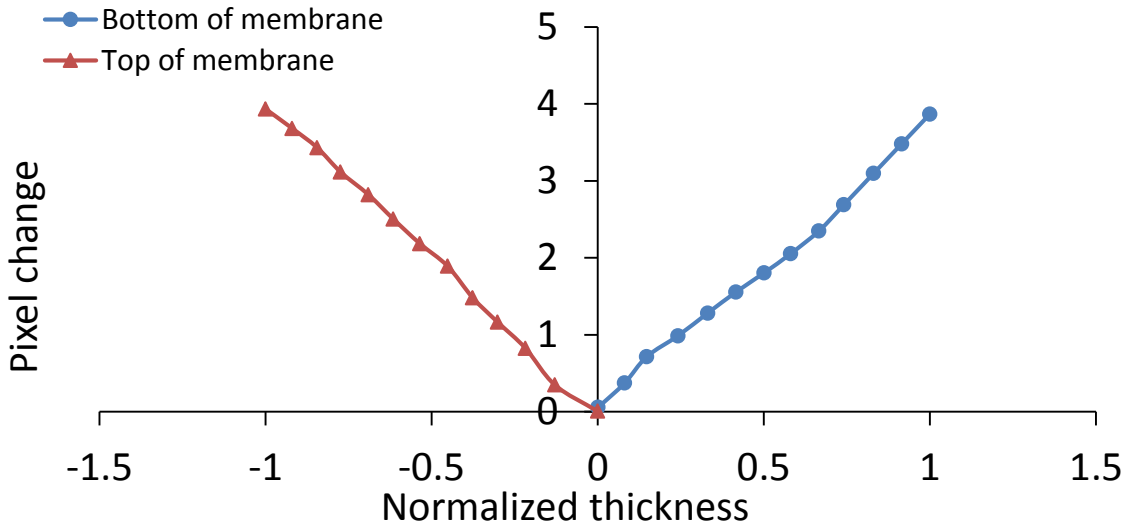

Figure 5-11. Relative displacement in thickness direction for normalized thickness at membrane top and bottom for a humidity value of 76%

As seen in Figure 5-11, the thickness change gradually increases with distance from the center of the membrane. Furthermore, the difference between top and bottom is within the errors of the measuring technique. This information shows the homogeneity of the swelling in the membrane. Figure 5-12 shows the swelling strain calculated by dividing the thickness change in Figure 5-11 by the membrane thickness. Except for 1 point at a thickness of roughly 0.15, the strain was found to show relatively low fluctuations throughout the normalized thickness of the membrane. As the membrane images were taken at steady state and the entire domain was humidified to the same humidity value, it would be expected for the swelling strain to be uniform across its thickness. The data presented in Figure 5-12 shows relatively low fluctuations in swelling strain with

normalized thickness, as expected. The strain was found to vary between the values of 3.4 and 3.8 %.

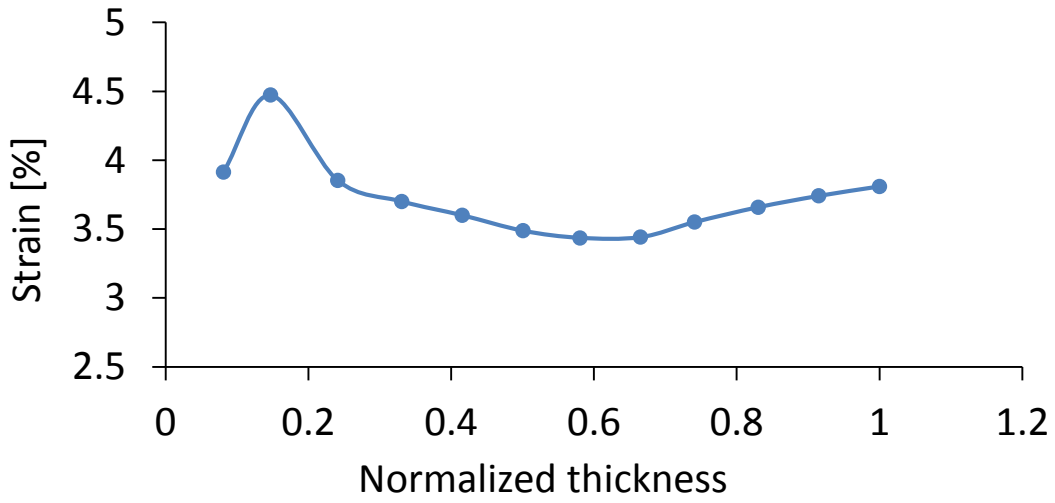

Figure 5-12. Variation of strain with normalized thickness for GDE sandwiched nafiton-TiO_2 membrane with C = 0.2% wt in microscope acquired images.

Displacement distributions were also calculated for OCT scans. Similar results were found from OCT scans and microscope acquired images. Vector fields for a GDE sandwiched Nafion-TiO_2 membrane with a concentration of 0.5% wt are displayed on Figure 5-13. The membrane was imaged through a GDE layer containing a slit of 100 μm wide. The vector plots found on Figure 5-13 below are for humidity values of 38, 41, 47 and 50 % respectively. It can be seen that the results from the OCT scans are similar to those found from microscope acquired images. However, the vector plots from OCT scans are seemingly noisier, containing a fair amount of randomness, even after smoothing. It is still possible to see that there is an evident section in the middle where the displacement is nearly zero, similar to the results presented on Figure 5-9. The magnitude of the vectors gradually increase as they get closer to the upper and lower boundaries of the membrane.

Contour plots for the displacement in the through thickness direction can be found on Figure 5-14. A clear evolution of swelling can be noticed as the humidity value increases.

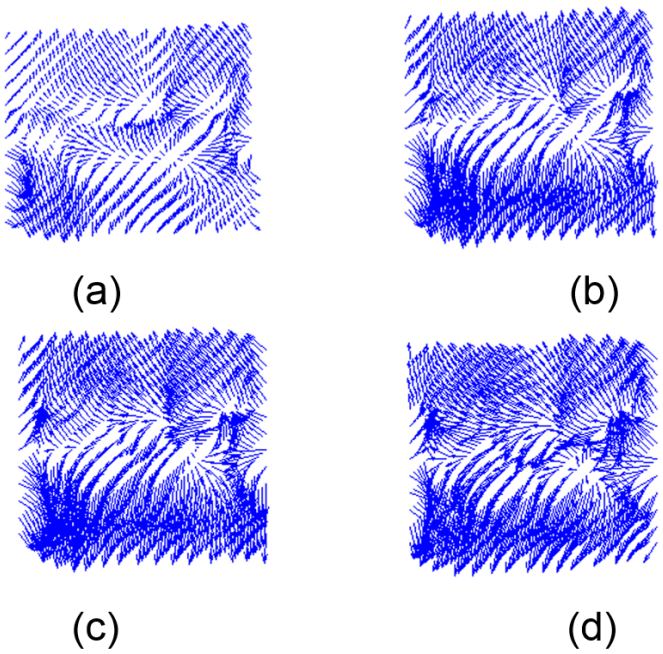

Figure 5-13. Vector field for displacement of a Nafion-TiO_2 membrane c = 0.5% wt sandwiched by GDE layers. The humidity values of 38 % (a), 41 % (b), 47% (c) and 50 % (d)

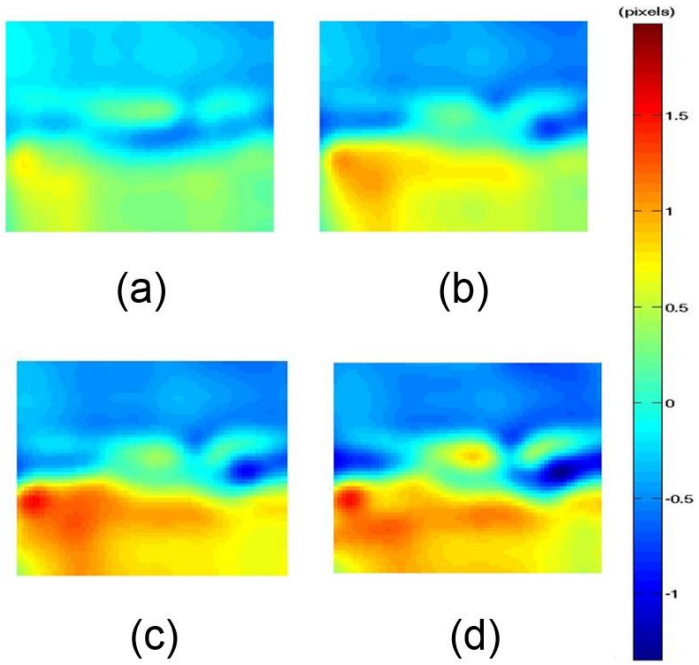

Figure 5-14. Contour plots for displacement in thickness direction for a Nafion-TiO_2 membrane C = 0.5% wt sandwiched by GDE layers. The humidity values are 38 % (a), 41 % (b), 47% (c) and 50 % (d)

The contour plots calculated from OCT scans show some clear differences compared to those calculated from microscope acquired images from Figure 5-10. Similar to what was found on the vector fields in Figure 5-13, the contour plots of Figure 5-14 show some variations in displacement and are less homogeneous than those of Figure 5-10. In other words, after carefully analysing the results from Figures 5-10 – 5-14 it can be concluded that the DIC results from microscope acquired images seem to be significantly more homogeneous than those from OCT scans. The results from OCT scans tend to contain a higher degree of noise and randomness. This is believed to be due the relatively low number of pixels composing the membrane in the OCT scans. This issue is further discussed on section 5.4

However, a clear trend of increasing thickness can be seen in the displacement map found from DIC of OCT scans. Even though the results from OCT elastography present a considerable higher amount of noise, the results show the potential of OCT elastography for imaging Nafion membranes through GDE material.

5.3 In-Situ Cell Imaging – Qualitative Analysis

The previous sections showed how though thickness swelling strain can be experimentally found for Nafion-TiO_2 membranes by DIC making use of either microscope acquired images or OCT scans. Though thickness strain maps were also demonstrated in the last section for an ex situ experimental setup. As mentioned in the first two chapters of this work, one of the goals of this project was to demonstrate that the results found from the ex situ experimental setup could be replicated in an in situ setup. Due to time constraints and limited access to the OCT system a full in situ experiment could not be carried out. However, a number of scans were taken at different humidity values for qualitative analysis, as shown in Figure 5-15.

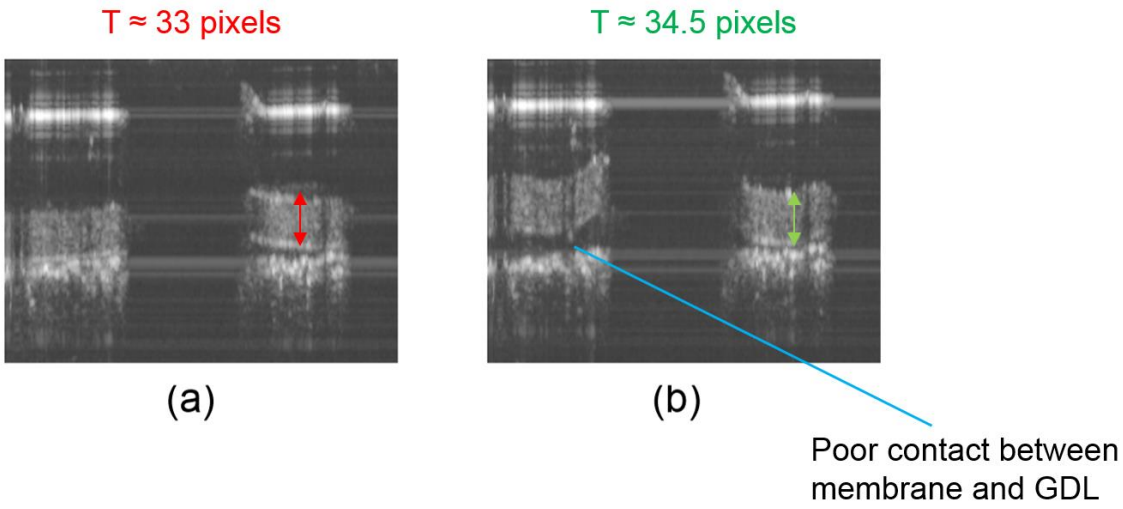

Figure 5-15. OCT Scans of Nafion membrane inside in situ test cell under relative humidity values of 30 % (a) and 68 % (b)

The two pictures displayed on Figure 5-15 show OCT scans acquired from the in situ test cell. The cells clamping pressure was set to 50 psi and it was heated up to 80 °C. The humidity was set to 30 % and left at steady state for roughly 2 minutes before scans were taken. The humidity was then increased to 68% and the same procedure repeated. The scans on Figure 5-15 show the land section of the membrane being imaged through a narrow slit with a width of 100 µm through GDE layer. As it can be seen the polycarbonate chip allows for the passage of the OCT laser beam without significant signal interference. The vertical lines above the membrane sections of the land represent the interface between the polycarbonate strip of the chip and the slit of the GDE. It is possible to observe some degree of membrane swelling between the two images. When the thickness was manually measured, it was found that the thickness was higher once the material had been humidified, as shown in Figure 5-15. Furthermore, it is possible to see that the membrane on the left hand side of the scan with a humidity of 68 % does not touch the lower GDE layer. This indicated poor contact within the components of the cell. However, the scans presented in this section still show OCT elastography as a viable technique for measuring in situ swelling strain of Nafion membranes.

5.4 Current Issues and Recommendations for Future Work

There are currently a number of known deficiencies with the test apparatus and procedure carried out for this project. This section mentions the issues experienced in this project as well as laying down recommendations for the future reproduction of the experiments.

The reference measurements of membrane thickness carried out in this experiment made use of manually drawing lines and determining the thickness of the membrane by a pixel count technique. However, as this process was carried out manually, it is subject to human error. Even though its uncertainty was estimated to only be approximately 6%, it is possible that the results could be impacted by observer. However, to the knowledge of the author, there is currently no other technique that is bale to measure membrane strain or displacement maps in situ in fuel cells. Therefore at the present date, the measurement technique used in this work is accepted as a good validation tool for the DIC of Nafion membrane scans.

It is possible that small discrepancies exist between results obtained from OCT scans and microscope acquired images due to the location where the data is taken. OCT scans were taken from a location close to the centre of the polycarbonate plates, while the microscope images were taken at the top of the polycarbonate plates, where the membrane was in contact with dry air. A small variation in humidity values could have occurred between data from OCT and microscope acquired images. The relative humidity sensor was placed next to the section where the OCT scans were taken from. As the section of the membrane were the microscope images were taken from was in contact with air, these edge effects may have caused the membrane to be slightly drier than what the relative humidity sensor was reading. In order to minimize these edge effects, the fuel cell test station was set to output a high volumetric flow rate of humidified air. The volume flow rate used for all experiments was of 2 L/min of humidified air. A direct comparison with experiments carried out at the same conditions would be necessary to estimate any discrepancies between the two procedures. However, OCT and microscope experiments were carried out at 80°C and 50°C respectively.

While conducting digital image correlation of OCT scans it was noticed that the speckle pattern between humidity steps behaved differently between the lower and upper ends of

the humidity range. When the humidity value was between values of 20 – 45 %, very small changes in the speckled pattern were seen between humidity step changes. As mentioned before, OCT scans were taken for every step change of 2 % in relative humidity. However, in the lower range, the algorithm was able to correlate images with a humidity step change from 5 – 6% with a high success ratio. However when the humidity value was between the 50 – 70% these step changes had to be reduced to 2 % for the algorithm to keep a similar success rates in correlating successive scans. This value had to be further lowered to 1 % for humidity values above 70%. This phenomenon seems to correlate with the information provided in Figure 4-16 through Figure 5-3, which show how strain evolves with humidity. In the lower humidity range the curve is shallower, while in the upper part of the humidity range, the curve becomes steeper. This would explain why at lower humidity values a step change in 5 – 6 % is acceptable. There is little variation of dimensional size with humidity, for this range and the algorithm is able to successfully track the displacements for step changes of 5 – 6%. However, in the upper section of the humidity range the curve becomes much steeper. This translates to greater dimensional changes with small humidity step changes.

No mechanical testing of the Nafion-TiO_2 membranes used in this project was carried out prior to carrying out DIC. Therefore the exact mechanical properties of the material are unknown. However, if these facts were known, it would be possible to analyze shifts from the elastic range to the plastic range of the material when analysing contour plots. Another potential technique for analysing presence of plastic strain would be to study the membrane under dehumidification and search for hysteresis on the strain curve. However, due to limited testing time, it was not possible to acquire any data from dehumidification tests.

A sudden change in speckled pattern of the composite membranes was noticed when the humidity values reached approximately 56 %. It has been observed that the morphological structure of Nafion undergoes a radical change for water volume fraction values above 0.5 [18]. As mentioned in chapter two, a phenomenon named inversion takes place at that water volume fraction level. Furthermore, it was notices that this sudden change in speckled pattern was roughly at the same location of the inflection point in the third order polynomial curves found in Figures Figure 4-16 through Figure 5-37. It is believed that this sudden

change in speckled pattern is the result of inversion between backbone and side chains of the membrane leading to sudden change in the mechanical properties of the material.

The vector fields presented in Figure 5-13 and the contour plots in Figure 5-14 presented a considerably higher amount of noise or randomness when compared to those of Figure 5-9 Figure 5-10. This is believed to take place as the combined effect of two different factors. The first factor is the small amount of pixels making up the membrane. In OCT scans the pixel to micron ratio was approximately 0.55. As the Nafion membranes studied in this work were approximately 80 μm thick, their thickness in pixels was approximately 44- 45 microns and lowered to approximately 40 micros after compression. As the subset size used was of 20 pixels, their size in pixels represented roughly half the thickness of the membrane. This lack of information in the OCT scans is believed to lead to the higher noise in the results. In comparison, the same membranes were approximately 150 pixels thick in the microscope acquired images due to a higher pixel/micron ratio, explaining the smoother results. In order to achieve a more homogeneous results with less noise in them, a system with a higher pixel/ μ ratio could be used. Normally time domain systems are able to deliver a higher ratio due to the increased sampling rate. This can be maximized by adjusting the scanning speed of the reference arm and the scanning frequency.

The second factor affecting the experienced noise in the vector fields and contour plots of Figure 5-13 Figure 5-14 was the formation of the vertical displacement artifacts shown in figures Figure 4-12. As mentioned earlier, these artifacts are believed to take place due to the white horizontal lines that make up upper and lower interface of the membrane. Scans were taken in a system with higher axial resolution and it was found that the thickness of these lines greatly decreased, as shown in Figure 5-16 below. By making use of a higher resolution system, it is believed these lines would significantly decrease in thickness, leading to a decrease in noise in the contour plots and vector fields.

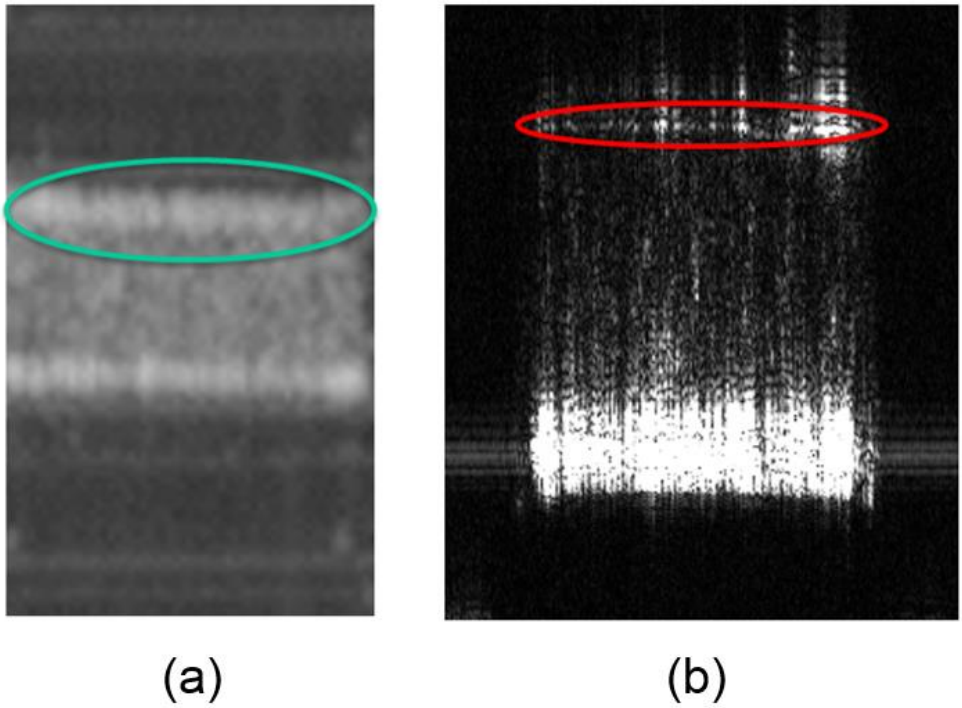

Figure 5-16. Difference between scans of membrane in systems of axial resolution of 7 µm (a) and 1 µm (b).

Chapter 6: Conclusions

The present work demonstrates for the first time that OCE is a viable technique for measuring deformation and generating strain/ displacement maps of Nafion membranes for fuel cells. To the knowledge of the author, there are currently no known techniques with the capacity to carry out Nafion strain measurements in fuel cells in situ. This work demonstrated that it is possible to generate strain or displacement maps of Nafion membranes when images are acquired using an OCT system. Furthermore, the technique was demonstrated to have the potential to be carried out in situ, as OCT images were acquired from an in situ test setup. As the technique has the potential to measure localized strain, it could become a useful diagnostics tool for identifying under which operating conditions the membrane may undergo localized plastic strain and observe crack formation growth.

OCT membranes scans were analysed when the membrane was sandwiched by transparent polycarbonate flow field plates. The difference between optical path lengths between land and channel sections of the flow field plate led to an optical shift of the membrane between these two sections. Optical path length correction was applied for interpretation of the OCT scans.

Spatial diversity was used for filtering out unwanted speckled noise from the OCT scans and reducing background randomness. Fifty stationary scans were taken while conducting this technique. It was shown through intensity threshold that after the scans underwent spatial diversity filtering, that the random speckled noise in the background was removed. The superimposed noise on to the membrane section of the scans was also removed through this technique. As the technique was carried out making use of 50 stationary scans the speckled pattern of the membrane section of the scans was unaffected by the filtering technique.

The effect of subset size on displacement calculations was compared for four different subset sizes. It was found that by increasing the subset size the calculated strain decreased, leading to an underestimation of results. The compressive elastography results from PDMS-TiO_2 membranes for different subset sizes were compared to measured results for determining the optimal subset size. It was found that when a subset size of 20 pixels was

used, the agreement between measured and calculated results was within the estimated accuracy of the measuring technique. This subset size was used also found to be ideal when using it in microscope acquired images. This subset size was subsequently used for all remaining scans analysed in this work.

Smoothing was carried out in the output vector fields and contour plots to decrease noise inherent from speckle tracking. It smoothed vector fields and contour plots showed a significant visual enhancement, by canceling obvious erroneous results. The effect of smoothing on calculated strains was found to be within the errors of the technique and therefore negligible.

Membranes of different TiO_2 concentrations had their swelling strain compared for an analysis of its impact on the mechanical properties of the material. It was found that for the small concentrations used in this project there was small variation between the collected data for difference contrast agent concentrations. These variations are mainly attributed to experimental error and the accuracy of the present technique. Previous studies show how the use of high TiO_2 concentrations (3, 6 or 20 % wt) has an impact on the plastic modulus of the composite membranes [11, 24]. However, minor differences were seen in the elastic modulus. The low concentrations used in this project are believed to have a minor effect, not measurable with the current technique employed.

The effect of sandwiching GDE layers to Nafion membranes as well as a comparison between land and channel section of the membrane was quantitatively analysed through OCT speckle tracking. It was found that for bare membranes in comparison to the land section of the membrane the channel section underwent 25 – 30% more strain, regardless of the TiO_2 concentration. The same comparison between land and channel was carried out for GDE sandwiched membranes. It was found that even with the presence of GDE, the membranes still underwent approximately 25% more strain on the channel then in the land sections. However the use of GDE sandwiched membranes led to a decrease in swelling in both land and channel sections. The land underwent 12 – 14 % less strain when GDE layers were present. The channel experienced similar results with a reduction of 10 – 12 % for GDE sandwiched membranes. These values were, however, on the limit of the accuracy of the employed technique. However, it is believed that the use of GDE layers does in fact lead to a small decrease in swelling strain.

Displacement maps were calculated for both microscope acquired images and OCT scans. Vector fields and contour plots showed how the displacement gradually increased from the centre of the membranes towards the upper and lower edges. The results also showed how the displacement was relatively homogeneous throughout the land. The top and bottom of the membrane underwent same amounts of swelling as the membrane experienced homogeneous humidity. The swelling strain was also shown to be relatively constant through the thickness of the membrane when homogeneous humidity was applied to the domain. The vector fields and contour plots from OCT scans showed relatively good agreement to those from microscope acquired images, however due to limitations from the imaging system, the OCT elastography results presented a considerably higher amount of noise.

A sudden change in the membrane speckled pattern was observed for relative humidity values of approximately 56%. Similarly, at approximately the same point inflection occurs on the third order polynomials curves describing the swelling strain of the material through humidity changes. It is believed that inversion is responsible for this sudden shift in the speckled pattern also leading to changes in the mechanical properties of the material.

OCT scans for a functional cell setup were presented. Even though no quantitative results were shown from this data set, the results still show the potential of OCT elastography as an imaging technique for calculating in situ through thickness strain distribution in Nafion membranes.

Bibliography

[1] A. Kusoglu, M. Santare, A. Karlsson, S. Clrghorn and W. Johnson, "Numerical Investigation of Mechanical Durability in Polymer Electrolyte Membrane Fuel Cells," *Journal of The Electrochemical Society*, vol. 157, pp. B705-B713, 2010.

[2] A. Kusoglu, M. Santare, A. Karlsson, S. Cleghorn and W. Johnson, "Mechanical Behavior of Fuel Cell Membranes Dnder Humidity Cycles and Effect of Swelling Anisotropy on the Fatigue Stresses," *Journal of Power Sources,* vol. 170, pp. 345-358, 2007.

[3] N. David, P. Wild, J. jensen, T. Navessin and N. Djilali, "Simultaneous In Situ Measurement of Temperature and Relative Humidity in a PEMFC Using Optical Fiber Sensors," *Journal of the Electrochemical Society,* vol. 157, pp. B1173-B1179, 2010.

[4] M. Goulet, R. Khorasany, C. De Torres, M. Lauritzen, E. Kjeang, G. Wang and N. Rajapaske, "Mechanical Properties of Catalyst Coated Membranes for Fuel Cells," *Journal of Power Sources,* vol. 234, pp. 38-47, 2013.

[5] Y. Tang, A. Kusoglu, A. Karlsson, M. Santare, S. Cleghorn and W. Johnson, "Mechanical Properties of a Reinforced Composite Polymer Electrolyte Membrane and its Simulated Performance in PEM Fuel Cells," *ScienceDirect,* vol. 175, pp. 817-825, 2008.

[6] A. Kusoglu, M. Santare and A. Karlsson, "Aspects of Fatigue Failure Mechanisms in Polymer Fuel Cell Membranes," *Polymer Physics,* vol. 49, pp. 1506-1517, 2011.

[7] R. Solasi, "On Mechanical Behavior and in-Plane Modeling of Constrained PEM Fuel Cell Membranes Subjected to Hydration and Temperature Cycles," *Science Direct,* vol. 167, pp. 366-377, 2007.

[8] Y. Tang, M. Santare and A. Karlsson, "Stresses in Proton Exchange emmbranes Due to Hydration-Dehydration Cycles," in *Third International Conference of Fuel Cell Science, Engineering and Technology*, Michigan, 2005.

[9] T. Thampan, S. Malhotra, J. Zhang and R. Datta, "PEM fuel cell as membrane reactor," *Catalysis Today,* vol. 67, pp. 15-32, 2001.

[10] M. Mench, Fuel Cell Engines, New Jersey: John Wiley & Sons, 2008.

[11] M. Satterfield, P. Majsztrik, H. Ota, J. Benziger and A. Bocarsly, "Mechanical Properties of Nafion and Titania/Fafion Composite Membranes for Polymer Electrolyte Memvrabe Fuel CElls," *Journal of Polymer Science,* vol. 44, pp. 2327-2345, 2006.

[12] P. Majsztrik, "Mechanical and Trasport Properties of Nafion for PEM Fuel Cells; Temperature and Hydration Effects," 2008.

[13] S. Holdcroft, "Fuel Cell Catalyst Layers: A Polymer Science Perspective," *Chem. Mat.*, 2013.

[14] U. Buescher, S. Cleghorn and C. Johnson, "Challenges for PEM Fuel Cell Membranes," *Journal of Energy Research,* vol. 29, pp. 1103-1112, 2005.

[15] H. Tang, S. Peokang, S. P. Jiang, F. Wang and M. Pan, "A Degradation Study of Nafion Proton Exchange Membrane of PEM Fuel Cells," *Journal of Power SOurces,* vol. 170, pp. 85-92, 2007.

[16] S. Peighambardoust, S. Rowshanzamir and M. Amjadi, "Review of the Proton Exchange Membranes for Fuel Cell Applications," *International Journal of Hydrogen Energy,* vol. 35, pp. 9349-9384, 2010.

[17] Y. Wang, K. Chen, J. Mishler, S. Cho and X. Adroher, "A Review of Polymer Electrolyte Membrane Fuel CElls: Technology, Applications, and Needs on Fundametal Research," *Applied Energy,* vol. 88, pp. 981-1007, 2011.

[18] G. Gebel, "Structural Evolution of Water Swollen Perfluorosulfonated Ionomers From Dry Membrane to Solution," *polymer,* vol. 41, pp. 5829-5838, 2000.

[19] N. Deluca and Y. Elabd, "Polymer Electrolyte Membranes for the Direct Methanol Fuel Cell: A review," *Journal of Polymer Scicence,* vol. 44, pp. 2201-2225, 2006.

[20] M. Crum and W. Liu, "Effective Testing Matrix for Studying Membrane Durability in PEM Fuel Cells: Part 2. Mechanical Durability and Combined Mechanical and Chemical Durability," *ECS Transactions,* vol. 3, pp. 541-550, 2006.

[21] M. Silberstein and M. Boyce, "Hygro-Thermal Mechanical Behavior of Nafion During Constrained Swelling," *Journal of Power Sources,* vol. 196, pp. 3452-3460, 2011.

[22] Y. Tang, A. Karlsson, M. Santare, M. Gilbert, S. Cleghorn and W. Johnson, "An experimental investigation of humidity and temperature effects on the mechanical properties of perfluorosulfonic acid membranes," *Materials Science and Engineering,* vol. A 425, pp. 297-304, 2006.

[23] H. L. Tang, "A Mechanical Durability Comparison of VArious Perfluocarbon Proton Exchange Membranes," *Journal of Applied Polymer Scicence,* vol. 109, pp. 2671-2678, 2008.

[24] M. Satterfield, "Mechanical and Water Sorption Properties of Nafion and Composite Nafion/Titanium DIoxide Membranes for Polymer Electrolyte Membrane Fuel Cells," 2007.

[25] Z. Lu, M. Lugo, S. Michael, A. Karlsson, C. Busby and P. Walsh, "An experimental investigation of strain rate, temperature...," *Journal of Power Sources,* vol. 214, pp. 130-136, 2012.

[26] Y. Li, D. Dilalrd, Y. Lai, S. Case, M. Ellis, M. Budinski and C. Gittleman, "Experimental Measurement of Stress and Strain in NAfion Membrane during Hydration Cycles," *Journal of The Electrochemical Society,* vol. 159, pp. B173-B184, 2012.

[27] J. Catalano, T. Myezwa, M. De Angelis, M. Baschetti and G. Sarti, "The effect of relative humidity on the gas permeability and swelling in PFSI membranes," *International Journal of Hydrogen Energy,* vol. 37, pp. 6308-6316, 2011.

[28] F. Martinez, C. Imrie and G. Ribes, "Spectroscopic and Thermal Characterization of the Swelling Behaviour of Nafion Membranes in Mixtures of Water and Methanol," *Journal of Applied Polymer Science,* pp. 246-256, 2012.

[29] S. Eastman, "Effect of Confinement on Structure, Water Solubility, and WAter Transport," 2012.

[30] K. Butz, "Stress distribution and material properties demermined in articular cartilage from MRI-based finite strains," *Journal of Biomechanics,* vol. 44, pp. 2667-2672, 2011.

[31] I. Manke, C. Hartnig, N. Kardjilov, H. Reisemeier, J. Goebbels and J. Banhart, "In situ synchtrotron x-ray radiography investigations of water transport in PEM fue cells".

[32] P. Hajireza, W. Shi and R. Zemp, "Label-free in vivo fiber-based optical resolution photoacustic microscopy," *Optics Letters,* vol. 36, pp. 4107-4109, 2011.

[33] A. Bazylak, "Liquid WAter visualization in PEM fuel cells: A review," *International Journal of Hydrogen Energy,* vol. 34, pp. 3845-3857, 2009.

[34] R. McLaughling and D. Sampson, "Clinical applications of fiber-optic probes in optical coherence tomography," *Optical Fiber Technology,* vol. 16, pp. 467-475, 2010.

[35] J. Roth, J. Eller and F. Buchi, "Effects of Synchrotron Radiation on Fuel Cell Materials," *Journal of The Electrochemical Society,* vol. 2012, pp. F449-F455, 2012.

[36] D. Huang, E. Swanson, C. Lin, J. Schuman, W. Stinson, W. Chang, M. Hee, T. Flotte, G. Kenton, C. Piliafito and J. Fujimoto, "Optical Coherence Tomography," *Science, New Series,* vol. 254, pp. 1178-1181, 1991.

[37] P. Torok and F.-J. Kao, "Optical Coherence Tomography," in *Optical imaging and Microscopy,* Springer, 2007, pp. 401-436.

[38] J. Fujimoto, "Optical Coherence Tomography," *Applied Physics,* p. 10991111, 2001.

[39] D. Nolte, "Optical Coherence Tomography," in *Optical interferometry for Biology and Medicine,* West Lafayette, Springer, 2012, p. 297306.

[40] J. Schmitt, "Optical Coherence Tomography (OCT): A Review," *Journal of Selected Topics in Quantum Electronics,* vol. 5, no. 4, pp. 1205-1215, 1999.

[41] P. Hariharan, Basics of interferometry, Sydney: Academix Press , 1992.

[42] E. Alarousu, "Low Coherence Interferometry and Optical Coherence TOmography in Paper Measurements," University of Oulu, 2006.

[43] S. Lipson, Optical Physics, Cambridge: Cambridge University Press, 1995.

[44] I. R. Kenyon, The light Fantastic, New York: Oxford University Press, 2011.

[45] Drexler, "Optical coherence tomography-principles and applications," *Reports on Progress in Physics,* vol. 66, pp. 239-303, 2003.

[46] D. Hood, A. Raza, K. Kay, S. Sandler, D. Xin, R. Richt and J. Liebmann, "A Comparison of retinal nerve fiber layer thickness obtained with frequency and time domain optical coherence tomography (OCT)," *Optical Society of America,* vol. 17, pp. 3997-4003, 2009.

[47] J. Rogowka, "Optical Coherence Tomographic elastography Technique for measuring deformation and strain of atherosclerotic tissues," *Heart,* vol. 90, pp. 556-562, 2004.

[48] G. Pinton, J. Dahl and G. Trahey, "Rapid Tracking of Small Displacements With Ultrasounds," *Transactions on Ultrasonics, Ferroelectrics, and Frequency Control,* vol. 53, no. 6, pp. 1103-1116, 2006.

[49] J. Schmitt, "OCT Elastography: Imaging Microscopic Deformation And Strain of Tissue," *Optics Express,* vol. 3, no. 6, pp. 199-211, 1998.

[50] B. Friemel, L. Bohs and G. Trahey, "Relative Performance of Two-Dimensional Speckle-Tracking Techniques: Normalized Correlation, Non-Normalized Correlation and Sum-Absolute-Difference," *Ultrasonics Symposium,* p. 14811484, 1995.

[51] E. Jones, "Documentation for Matlab-based DIC code," University or Illinois, 2013.

[52] M. Kirillin, "Contrasting properties of gold nanoshells and titanium dioxide nanoparticles for optical coherence tomography imaging of skin: Monte Carlo simulations and in vivo study," *Jounal of Biomedical Optics,* vol. 14, no. 2, 2009.

[53] N. Nassif, W. Armostrong, J. Boer and B. Wong, "Measurement of Morphological Changes Induced by trauma with the Use of Coherence Tomography in Porcine Vocal Cords," *Otolaryngology-Head and Neck Surgery,* vol. 133, pp. 845-850, 2005.

[54] T. Lee, A. Oldenburg, S. Sitafalwalla, D. Marks and W. Luo, "Engineered microsphere contrast agents for optical coherence tomography," *Optics Letters,* vol. 28, pp. 1546-1548, 2003.

[55] R. Abbaraju, N. Dasgupta and A. Virkar, "Composite Nafion Membranes Containing Nanosize TiO2/SnO2 for Proton Exchange Membrane Fuel Cells," *Journal of the Electrochemical Society,* vol. 155, no. 2, pp. 1307-1310, 2008.

[56] J. Schmitt, S. Xiang and K. Yung, "Speckle in Optical Coherence Tomography: An Overview".

[57] Hinds, "Novel In Situ Measurement of Relative Humidity in a Polymer Electrolyte Membrane Fuel Cell," *Journal of Power Sources,* vol. 186, pp. 52-57, 2009.

[58] "Spectrum Chemicals & Laboratory Products," Spectrum Chemicals & Laboratory Products, [Online]. Available: https://www.spectrumchemical.com. [Accessed march 2014].

[59] "Dow Corning," Dow Corning, March 2014. [Online]. Available: http://www.dowcorning.com/. [Accessed 2014].

[60] W. Chang, J. Hwang, F. Weng and S. Chan, "Effect of clamping pressure on the performance of PEM fuel cell," *Journal of Power Sources,* vol. 166, pp. 149-154, 2007.

[61] F. Glaudiere, I. Masson, S. Morin-Grognet, O. Thoumire, J. Vannier, H. Atnabi, G. Ladam and B. Labat, "Mechano-chemical control of cell behaviour by elastomer templates coated with biomimetic Layer-byLayer nanofilms," *Soft Matter,* vol. 8, pp. 8327-8337, 2012.

Appendix A – Strain Percentage Error

Section 4.4 of this report studied the effect of subset size on the accuracy of DIC when compared to the reference measurement technique. Table 4-3 presented the calculated strain results for a number of subset sizes. Those results were compared to the measured results and a percentage difference was calculated. Only the results for a pressure of 80 psi were shown in table 4-3. In this section, the results for other pressure values making use of a subset size of 20 X 20 pixels are compared to the reference measurement technique. However, as seen in figure 4-9, the data for measured and calculated results was not obtained at the exact same pressure points. Hence, for the purposes of the results displayed in this section, some of the calculated and measured results had to undergo interpolation in order for a direct comparison to be carried out. The results are displayed in Table 7-1. Interpolated results are highlighted in red.

Table 7-1 Strain percentage difference for different pressure values

Pressure (psi)	Measured Strain	Calculated Strain Subset Size 20 X 20	Percentage difference %
38	1.35	1.36	0.477669108
55	3.38	2.64	21.90685077
70	4.98	4.22	15.32743607
75	5.67	5.46	3.739168619
80	6.17	6.04	2.194550344
84	6.57	6.55	0.344355124

As seen in Table 7-1, for most of the pressure range, there is a relatively low difference between measured and calculated results. Except for the pressure values of 55 and 70 psi, the percentage difference is always lower than 4%. This value is still lower than the estimated uncertainty of the measurement technique (± 5%), showing good agreement between measured and calculated results.

The pressure values of 55 and 70 psi however, presented a variations close to 20%, which is significantly higher than the estimated accuracy of the technique. However, the interpolation of results for pressures of 38, 75, 80 and 84 were carried out with data acquired near the vicinity of these points. In other words, the interpolation was carried out

with data from only 1 or 2 psi away from the interpolated results. For example: the interpolation of pressure point of 75 psi for calculated results was carried out with data from pressure points of 74 and 75.5 psi. On the other hand, there was a big gap in data acquired for calculated results from a pressure of roughly 40 psi up to about 75 psi. The interpolation for results with subset size of 20 X 20 at a pressure point of 55 psi was carried out with data from pressure points at 54 and 77 psi, which represents a much greater difference.

Therefore, it is believed that there is in fact good agreement between measured and calculated results when a subset size of 20 X 20 pixels is used. The variation between the two results is believed to be within the uncertainty of the measurement technique (± 5%), even though some results presented on Table 7-1 seemed to demonstrate otherwise. There results that indicated poor correlation between measured and calculated results were calculated with interpolation of values at a great distance from each other and are believed not to be representative.

Appendix B – Uncertainty Estimation

In chapter 4 the difference between measured and calculated results making use of DIC was compared. It was mentioned that the estimated uncertainty of the measurement technique was approximately ± 5%. This section shows how the estimation of the uncertainty of the technique was carried out.

The measurements were taken at the same section of the membrane by drawing a vertical line across it. A clear reference point was used due to the ease to replicate measurements at the same location, as seen in Figure 7-1. Image analysis software ImageJ allows for ease count of length of drawn lines in pixels. The measurement was carried out 6 times for a PDMS-TiO_2 membrane under a clamping pressure of 30 psi.

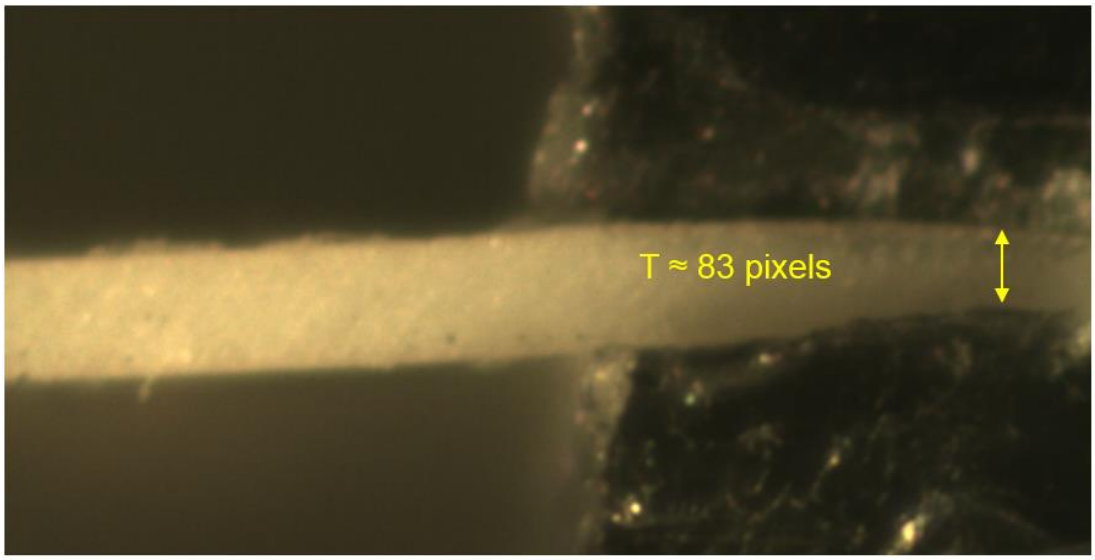

Figure 17-1. Pixel count thickness measurement

The results of all six measurements can found on Table 7-2

Table 7-2. Results of pixel count measurements

#1	#2	#3	#4	#5	#6	Average
83	85	78	80	79	78	80.5

The range was calculated as demonstrated in equation 7.1 below:

$$Range = Max - Min \tag{7.1}$$

Where Max is the maximum value found in Table 7-2 (85 pixels) and Min is the minimum value (78 pixels). The range was calculated to 7 pixels. The error or uncertainty was found by taking half of the range (3.5 pixels). The uncertainty value was calculated to about 4.34 % of the average results of the 6 readings. This value was further rounded up to 5%.